Investigation of the mesenchymal manifestations of tuberous sclerosis complex using tissue-engineered disease models

PhD Thesis

by

Adam Derrick Pietrobon

Doctoral Candidate

Program entry in June 2018

Supervised by

Professor William L. Stanford

Department of Cellular and Molecular Medicine

Faculty of Medicine

University of Ottawa

TABLE OF CONTENTS

ACKNOWLEDGEMENTS

To my supervisor, Dr. William Stanford: thank you for your guidance, support, and for helping me grow and explore as a young researcher.

To my Thesis Advisory Committee members, Dr. Harold Atkins, Dr. Rashmi Kothary, and Dr. Bernard Thébaud: thank you for your mentorship and for constantly steering me upwards and onwards.

To the members of the Stanford lab, past and present: thank you for the stimulating scientific discussions and for making this experience a memorable one.

And to my friends and family, near and dear: thank you for all your love and kindness. I have nothing but endless gratitude for your unwavering support throughout this journey.

ABSTRACT

Tuberous sclerosis complex (TSC) is a multisystem tumor-forming disorder caused by biallelic inactivation of *TSC1* or *TSC2*. The primary cause of mortality arises from mesenchymal manifestations in the lung and kidney: pulmonary lymphangioleiomyomatosis (LAM) and renal angiomyolipomas (RAMLs). Despite a well-described monogenic etiology, there remains an incomplete understanding of disease pathogenesis. Consequentially, tractable models which fully recapitulate disease characteristics are lacking. Here, I develop and study novel tissue-engineered models of TSC lung and kidney disease. In my first chapter, I demonstrate that lung-mimetic hydrogel culture of pluripotent stem cell-derived diseased cells more faithfully recapitulates human LAM biology compared to conventional culture on two-dimensional plastic. Leveraging this culture system, I conducted a three-dimensional drug screen using a custom 800-compound library, tracking cytotoxicity and invasion modulation phenotypes at the single cell level. I identified histone deacetylase (HDAC) inhibitors as a group of anti-invasive agents that are also selectively cytotoxic towards *TSC2*$^{-/-}$ cells. HDAC inhibitor therapeutic effects remained consistent *in vivo* upon xenotransplantation of LAM cellular models into zebrafish. In my second chapter, I develop a genetically-engineered human renal organoid model which recapitulates pleiotropic features of RAMLs *in vitro* and upon orthotopic xenotransplantation. I find that loss of *TSC1/2* affects multiple developmental processes in the renal epithelial, stromal, and glial compartments. First, loss of *TSC1/*2 leads to an expanded stroma by favouring stromal cell fate acquisition and alters terminal stromal cell identity. Second, epithelial cells in the *TSC1/2*$^{-/-}$ organoids exhibit a rapamycin-insensitive epithelial-to-mesenchymal transition. Third, a melanocytic population forms exclusively in *TSC1/2*$^{-/-}$ organoids, branching from MITF^{+} Schwann cell precursors of a *bona fide* neural crest-to-Schwann cell differentiation trajectory.

Through these two thesis chapters, I realize the power of tissue-engineered models for the study of TSC. This work offers novel insights into the pathogenesis of RAMLs and identifies a new class of therapeutics suitable for trialing in patients with pulmonary LAM.

THESIS OVERVIEW

This thesis includes two Data Chapters, each of which is comprised of a manuscript submitted for peer-reviewed publication. Implicitly, these manuscripts are self-contained articles which report all pertinent background information, description of methodology, and discussion of results. To complement these articles, the Introduction section of the thesis provides an expanded background to the subject at hand, while presenting critical rationale for the investigations described in the manuscripts. Finally, the Discussion section offers a global synthesis of the manuscripts, integrating key findings in a comprehensive analysis and proposing a bold new conceptual framework for understanding disease pathogenesis.

INTRODUCTION

Background on tuberous sclerosis complex

Disease overview

Tuberous sclerosis complex (TSC) is a monogenic multisystem disorder characterized by tumor formation in multiple organ systems, including the brain, skin, lungs, heart, and kidney.[1,2] The disease prevalence is approximately 1:6000 – 1:10,000 and exhibits an autosomal dominant inheritance pattern, although most cases arise sporadically.[1–4] The genetic etiology is a loss of function mutation in either *TSC1* or *TSC2*,[5–7] canonically leading to constitutive activation of the mechanistic target of rapamycin complex 1 (mTORC1).[8] The current standard of therapy includes treatment with the allosteric mTORC1 inhibitor rapamycin (clinically, sirolimus or the analogue everolimus), which exhibits efficacy in stabilizing several TSC-related manifestations.[9–13]

Mesenchymal manifestations of TSC

The leading cause of mortality in TSC patients is from mesenchymal manifestations in the lung and kidney: pulmonary lymphangioleiomyomatosis (LAM) and renal angiomyolipomas (RAMLs).[14,15] Pathologically, these lesions are characterized as neoplasms with perivascular epithelioid differentiation, termed PEComas.[16,17] PEComas are notably composed of histologically distinctive cells which have no anatomical counterpart in the normal human body.[18,19] In addition, these lesions possess a distinctive immunophenotypic profile, expressing smooth muscle or contractile proteins (ACTA2), melanocytic markers (PMEL, MLANA, MITF), and markers typically associated with mesenchymal cells (VIM, HMGA2, CSTK).[18,20–23,23–29]

RAMLs are solid tumors that exhibit a varying composition of dysplastic vasculature, fatty deposits, and smooth muscle-like components.[30] RAMLs affect approximately 60-80% of TSC patients, most often multifocal and bilaterally, and are generally asymptomatic.[31–34] The median age for TSC patients to exhibit radiographically detectable RAMLs is 7-11 years,[32,34,35] although the size and number generally increase over time.[36,37] Patients with TSC are also commonly affected by renal cysts; infrequently, cysts and RAMLs can co-occur in a phenomenon known as AML with epithelial cysts.[30,38] RAMLs can be found sporadically in the non-TSC patient population, yet in this case, they primarily occur as solitary unilateral lesions.[39]

LAM, in contrast, is an interstitial lung disease characterized by diffuse cystic destruction of the pulmonary parenchyma by invading "LAM" cells.[40–44] These invading cells digest the lung parenchyma, leading to progressive respiratory decline and fatality if untreated. Consequentially, LAM patients may experience a variety of pulmonary signs, including recurrent pneumothorax, chylothorax, abdominal hemorrhage, and lymphadenopathy.[45] Interestingly, clinically significant LAM almost exclusively occurs in female patients, and is generally first detected in adulthood.[46,47] Like RAMLs, LAM can occur sporadically in the non-TSC general population.[48,49]

Disease genetics

The genetic etiology of TSC lesions is classically described to follow the Knudson two-hit hypothesis, whereby a patient possesses a germline inactivating *TSC1/2* mutation followed by mosaic inactivating second-hit events.[50–53] Bi-allelic inactivation of *TSC1/2* is sufficient for human RAML formation.[54–56] Indeed, between-patient disease severity is likely attributable to variable mosaicism, [50–53] underscoring the role of second hit mutations in conferring disease.

Similarly, the genetic etiology of LAM lesions has been ascribed to loss of function mutations in either *TSC1* or *TSC2*,[5–7] although it has yet to be proven if this mutagenic event is sufficient for tumorigenesis. While TSC-associated LAM can arise from mutations in either *TSC1* or *TSC2*, sporadic LAM almost exclusively occurs as a loss of function of *TSC2*.[57] Importantly, TSC patients with mutations in *TSC2* generally exhibit a greater disease severity (in terms of both tumor burden and clinical phenotype), compared to patients with mutations in *TSC1*.[58–63]

Disease biochemistry

TSC1 and TSC2 are canonically described as negative regulators of mTORC1 signaling (**Figure 1**). These two proteins physically interact along their coiled-coiled domains, and with TBC1D7, form a functional trimeric complex.[64,65] TSC2 possesses a GTPase activating domain which can hydrolyze the GTP bound by Ras homolog enriched in brain (RHEB) and lead to inhibition.[66] In its GTP-bound form, RHEB allosterically activates mTORC1, a complex composed at minimum of mechanistic target of rapamycin (mTOR), Raptor, and mLST8.[67–71] mTORC1 is a serine/threonine kinase with a variety of direct effectors such as S6K1 and 4E-BP1.[72,73] Recent literature suggests RHEB is an essential activator of mTORC1[73,74] and acts by directly binding mTOR to induce a global conformational change to accelerate catalysis.[75] Importantly, the TSC complex is the only well-described GAP for RHEB, with no complementary GEF identified to date.[74]

More broadly, mTORC1 is often depicted as a master regulator of growth, sensing and integrating diverse nutritional and environmental cues such as growth factors, energy levels, cellular stress, and the presence of amino acids.[72,73] Upon favourable conditions, signals converge on mTORC1 to promote anabolic processes such as mRNA translation and lipid

synthesis, or by limiting catabolic processes such as autophagy. During adverse conditions, mTORC1 is inhibited to facilitate the converse biological processes. Many upstream inputs signal through TSC1/2 to regulate the nucleotide-loading state of RHEB.

Classically, TSC is described as a disease of mTORC1 hyperactivation. When TSC1 or TSC2 is absent, the functional heterotrimeric complex cannot form and RHEB is left unchecked to continuously activate mTORC1. This perpetual activation of mTORC1 uncouples the complex from environmental cues and leads to continued growth and proliferation, even in the presence of adverse extracellular cues.

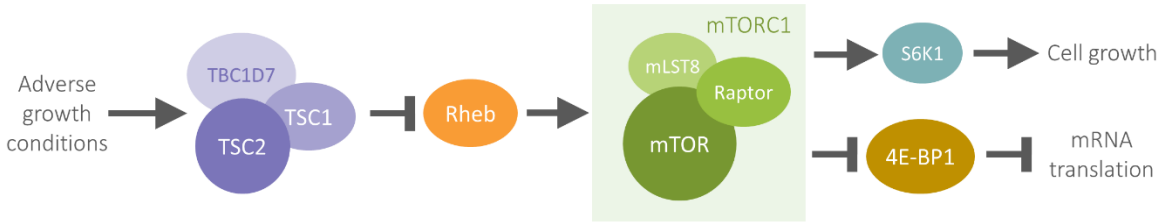

Figure 1. Schematic representation of mTORC1 regulation by the TSC complex.

Challenges facing the study of the mesenchymal manifestations of TSC

An incomplete understanding of disease pathogenesis

A major area of focus in the study of the mesenchymal manifestations of TSC has been lesion pathogenesis. RAMLs are classically described as hamartomas, and hence, considered lesions of disordered developmental.[23,50] All histological constituents of RAMLs are of clonal origin,[76,77] indicating a single mutational event can produce the remarkably phenotypic diversity. However, the exact cellular pathogenesis, including the cell of origin, remains unknown. Several candidates have been proposed, including pericytes,[78] lymphatic endothelium,[79] renal proximal tubular epithelium,[80] and neural crest cells.[81] The principal pieces of evidence for these

postulated cells of origin include any combination of the following: tissue marker expression; presumed progenitor potency due to lesion cellular diversity; and phenotypic characteristics of the pathological cells. However, loss of *TSC1/2* can significantly alter cell fate. For example, inactivation of *TSC1/2* alters neural progenitor differentiation trajectory to favour acquisition of a glial fate.[82,83] Thus, the physiological cell of origin cannot be easily inferred from terminal pathological cell characteristics.

The pathogenesis of LAM is even more enigmatic. In the early 2000s, an intriguing observation was made: identical mutations in *TSC2* were identified in LAM cells and RAMLs, suggesting the possibility of a clonal origin of disease.[57,84,85] This led to postulation of a "benign metastasizing" mechanism, whereby cells from RAMLs entered circulation and seeded the lungs to precipitate the LAM phenotype.[43,44,86] Additional pieces of data supported this hypothesis: circulating LAM cells have been detected in a variety of fluids,[87,88] and following transplantation, LAM cells of the same host genetic aberrations have been detected in the allografted lungs.[89,90] To date, this mechanism has still not be causally evidenced, and the cell of origin remains unknown. Other candidate source tissues proposed but not definitely proven include the uterus, lymphatics, and neural crest.[79,81,91,92]

While metastasis remains a plausible mechanism to explain mesenchymal disease pathogenesis, an alternative hypothesis is the mutagenesis of a common kidney-lung progenitor cell during development. In favour of a developmental second-hit, low level mosaicism was recently identified in a case of sporadic pulmonary LAM that did not meet TSC clinical diagnostic criteria.[93] A pulmonary-resident cell of origin for LAM is supported by a recent study which reported diffuse cystic lung disease upon biallelic inactivation of *Tsc2* in mouse lung mesenchyme.[94] Since the major cellular constituents of the kidney and lung segregate early in

development, mutagenesis of a common precursor must occur early in embryogenesis. Similar spatial segregation of identical genotypes have been observed in the TSC kidney lesions, as spatially-distinct RAMLs from the same patient can possess identical second-hit events.[54,55] Barring the possibility of RAML-cell migratory capacity, spatially distinct renal lesions of identical genetics likely arose from a common progenitor which segregated during development. Together, these data support both RAMLs and LAM as diseases of disordered development with a common etiology.

A lack of disease-relevant models

As a consequence of our limited understanding of lesion pathogenesis, tractable models of mesenchymal TSC lesions which fully recapitulate disease characteristics are lacking. *In vitro*, the most commonly employed cell line is a renal angiomyolipoma-derived *TSC2*$^{-/-}$ cell, named 621-101.[95,96] This cell line is not infinitely expandable and required immortalization for propagation. Cultures of cells derived from human pulmonary LAM lesions grow as a mixture of *TSC1/2*$^{-/-}$ and wild type cells, prohibiting the establishment of a homogenous population of cells.[97] As a result, the 621-101 line is often used as a surrogate model of LAM. The paucity of human-relevant *in vitro* models has resulted in the widespread use of rodent cell lines- particularly those derived from unaffected tissues (e.g. mouse embryonic fibroblasts)- which do not model many features of the human disease.

Several *in vivo* modelling strategies have also been attempted, yet largely are unable to recapitulate the mesenchymal manifestations of TSC. As a monogenic disease, one would expect a gene knockout approach would yield the greatest success. However, early on, it was discovered homozygous loss of *Tsc1/2* is embryonic lethal in mice.[98,99] Since then, several temporally and

spatially restricted knockout models have been attempted, yet none have fully reproduced the mesenchymal manifestations of TSC.

A number of mouse strains have been generated which target biallelic inactivation of *Tsc1/2* to various renal resident cells, in an attempt to model RAMLs.[80,100–108] Generally, polycystic lesions of ranging expressivity are described, with greater phenotypic severity upon inactivation earlier in development and/or in more tubular segments. However, none of these conditional models reported fulminant RAML lesions. Similarly, several inducible and conditional knockout models have been attempted to model LAM, but none have yielded comprehensive pulmonary features.[109–111] The exception is a recent study reporting a diffuse cystic lung disease upon biallelic inactivation of *Tsc2* in mouse lung mesenchyme,[94] providing reassurance for the possibility of genetic model of LAM. Xenografting strategies for modelling LAM have also been attempted, generally leading to greater success in recapitulating disease characteristics.[112–120] The majority of these models have relied on immortalized cells and/or non-human cell lines, limiting the ability to conclude human disease-specific mechanisms.

A paucity of therapeutic options available to patients

Ultimately, the *raison d'être* of the study of human disease is the development of new therapies which improve the lives of patients. Unfortunately, like many other rare diseases, identification of novel small molecule agents for treatment of TSC manifestations has been a slow process. While supportive therapies exist, the only disease-modifying therapy available is rapamycin (clinically known as sirolimus or the analogue everolimus). Rapamycin is effective in slowing lung decline in LAM, inducing partial RAML regression, and reducing the number of disease-associated adverse events.[9,12,121–126] However, the effects of rapamycin are cytostatic, and

TSC lesions rebound upon cessation of treatment. In response, the TSC field has shifted towards the laudable goal of identifying novel cytotoxic agents which can rid patients of their lesions, conferring a long-lasting, curative effect. A variety of therapeutic strategies have shown promise in the pre-clinical development phase, such as autophagy inhibition,[127,128] and, more recently, immunotherapies.[112,113] To date, none of these therapeutics have realized clinical success. While a myriad of factors contributes to the translational gap, one reason may be the use of models during pre-clinical development which do not fully recapitulate human disease characteristics.

The emergence of tissue-engineered disease models

A new frontier in the disease modelling landscape

Disease complexity is rarely recapitulated *in vitro* when using classic monolayer homotypic culturing approaches. Application of tissue engineering techniques for modelling human disease is an evolving landscape which holds substantial promise. In broad strokes, tissue engineering is a catch-all concept referring to the combination of cellular and acellular (i.e., physiochemical) materials to recapitulate human tissues in a physiological manner.[129] Examples include hydrogel synthesis for modelling the extracellular matrix,[130] co-culturing diverse cellular sources to model complex heterotypic interactions,[131] and the generation of stem cell-derived three-dimensional structures termed "organoids" which model physiological tissue structure and function.[132–134]

Tissue-engineered disease models offer an attractive compromise between *in vivo* complexity and *in vitro* tractability. Compared to monolayer homotypic cell culture, tissue-engineered disease models possess greater architectural complexity, an expanded repertoire of measurable phenotypic readouts, and generally increased physiological-relevance. In contrast,

compared to animal models, tissue-engineered disease models permit a greater range of experimental manipulation, capacity for scale-up, all the while with enhanced time and cost efficiency. Thus, tissue-engineered models expand the scope of phenotypes previously accessible only in model organisms, while maintaining the tractability of *in vitro* systems.

Tissue-engineered disease models of TSC

TSC is an ideal candidate for modeling with a tissue engineering approach. Histologically diverse lesions that form in numerous organ systems all arise from loss of *TSC1* or *TSC2*, suggesting tissue-specific mechanisms are at play in conferring lesion pleiotropy. Tissue-engineered disease models offer a new venue for exploring mechanisms of organ-specific manifestations. Studying disease in the relevant tissue context is also critical to the identification of novel therapeutics, as *TSC1* or *TSC2* ablation confers tissue-dependent therapeutic vulnerabilities. For example, *TSC2*$^{-/-}$ neural progenitor cells are selectively sensitive to the cytotoxic effects of proteasomal inhibition, yet the closely related but distinct neural crest lineage does not share this sensitivity.[83]

Tissue-engineered models of TSC manifestations have already been reported. For example, several models of the brain manifestations of TSC- including heterotypic co-cultures and stem cell-derived organoids- have unlocked novel insights into neuropsychiatric pathogenesis and therapeutic vulnerabilities.[82,135–140] Investigations of the mesenchymal manifestations of TSC have also implemented tissue engineering techniques to unravel disease biology. For example, in an *ex vivo* 3D alveolosphere assay, *Tsc2*$^{-/-}$ mouse lung fibroblasts compared to WT were found to increase growth and colony-forming efficiency of the alveolar type 2 (AT2) organoids, as well transdifferentiate AT2 cells to AT1.[94] Another study reported

LAM cell / fibroblast spheroids attracted mast cells and induced mast tryptase release, contributing to disease progression.[141] Most recently, a heterogenous pluripotent stem cell-derived neural crest culture was observed to model features of LAM, both with or without biallelic inactivation of *TSC2*, raising questions on the relative contribution of genotype versus cell of origin in conferring LAM properties.[83] Despite successes in unlocking mesenchymal TSC biology using tissue-engineered disease models, these tools are still in their infancy and necessitate further study to realize their full potential.

DISCUSSION

In this thesis, I develop and study novel tissue-engineered models of TSC lung and kidney disease. In my first manuscript, I analyze a lung-mimetic hydrogel culture system of pluripotent stem cell-derived diseased cells. I demonstrate that this model system more faithfully recapitulates human LAM biology compared to conventional culture on two-dimensional plastic. Using this system, I identified HDAC inhibitors as a group of anti-invasive agents that are also selectively cytotoxic towards *TSC2*$^{-/-}$ cells, *in vitro* and *in vivo*. In my second manuscript, I develop a novel genetically-engineered human renal organoid model which recapitulates pleiotropic features of TSC kidney disease *in vitro* and upon orthotopic xenotransplantation. I find that loss of *TSC1/2* affects multiple developmental processes in the renal epithelial, stromal, and glial compartments. This work offers novel insights into the pathogenesis of TSC mesenchymal manifestation and identifies a novel class of therapeutics suitable for trialing in patients.

Tissue-engineered disease models permit novel investigations of biology

A key theme of this work is the remarkable utility of tissue-engineered disease models, and their ability to mimic physiological features of the human condition. By direct comparison, I demonstrate hydrogel culture precipitates transcriptomic features of primary LAM not observed on plastic. Indeed, implementation of a hydrogel culture system enabled identification of novel drug candidates that would have been missed if making isogenic comparisons on plastic. Currently, the mechanism by which hydrogel culture facilitates a more physiological phenotype is unclear. Introduction of a hydrogel to a culture system changes a wide variety of variables, including matrix stiffness, architecture, degradability, and ligand exposure, among other

factors.[142] Untangling the specific contribution of each component to the physiological phenotype is a worthwhile endeavour, but technically challenging with the synthetic hydrogel system employed. My work suggests many transcriptomic changes are mTORC1-dependent; a hypothesis can be formed that these changes occur via mechanotransduction signals, as TSC2 phosphorylation and activity is sensitive to matrix stiffness via focal adhesion kinase.[143,144] Future work is required to explore this mechanism and identify the specific biology conferred by each hydrogel constituent.

Similarly, the development and implementation of a renal organoid model facilitated an investigation into RAML pathogenesis that would not have been otherwise possible via classic homotypic monolayer culture, nor by current *in vivo* approaches. Indeed, there is currently no animal model which fully recapitulates human renal disease.[110] Since *TSC1/2* null embryos die *in utero*,[98,99] knockout animal models attempted have been limited by the *a priori* selection of the temporal and spatial context of mutagenesis. This introduces a cyclical logical fallacy; to better understand disease pathogenesis, a disease model is required, yet development of a disease model requires a more refined understanding of pathogenesis. As it is well-established that RAMLs derive from a monogenic etiology, the implementation of organoid technology permits analysis of *TSC1/2* knockout in all renal lineages while circumventing the issue of embryonic lethality. Despite conducting this work *in vitro*, pluripotent stem cell-derived renal organoids resemble the $1^{st}/2^{nd}$ trimester human kidney,[145,146] offering a tractable system for making physiological and pathophysiological inferences. It is reasonable to conclude that organoid technology bridges the gap between *in vitro* and *in vivo* investigation, permitting the study of biology in a manner not accessible by classical approaches.[147]

Unravelling the HDAC inhibitor mechanism of action is the next step towards clinical translation

A critical outcome of this work is the identification of HDAC inhibitors as therapeutic agents against LAM cells *in vitro* and *in vivo*. As the cytotoxic effects were seen to be mTORC1-dependent, these drugs hold promise for treating the diverse manifestations of TSC and will benefit from testing in other models, including the RAML system described here. A limitation of this strategy is the antagonistic effects of rapamycin, as many LAM patients are on a chronic regime of rapamycin. In addition, I anticipate a full unravelling of the mechanism of cytotoxicity and anti-invasion will be required prior to trialling in LAM patients.

The intuitive next step to investigating the mechanism of action would be to consider the direct consequences of targeted HDAC inhibition. My preliminary analysis suggests this is unlikely to be a fruitful line of investigation for several reasons. First, HDAC inhibitors are plagued by a long history of phenotypic effects that cannot be directly connected to inhibition of specific HDACs.[148] This is particularly notable for pan-HDAC inhibitors which modulate multiple targets. Second, analysis of target affinity for the HDAC inhibitors I tested (11 in total), did not show predilection of any one specific HDAC, or even class of HDACs, as the most likely modulated target(s). Third, HDAC inhibitor expression in the bulk RNA-seq data did not yield any consistent differences between *TSC2*$^{-/-}$ cells and WT in plastic or hydrogel. Fourth and finally, the concentration of HDAC inhibitors employed greatly exceeded the IC_{50} of their annotated targets, suggesting combinatorial or off-target mechanisms as most likely to be inducing the measured phenotypes.

I postulate a more effective strategy for uncovering the mechanism of action must involve a systems-based approach. An important clue can be gathered from the correlation of

transcriptomic changes with selective cytotoxic effects. Indeed, HDAC inhibitor genotype and matrix (i.e. hydrogel vs. plastic) selectivity is mirrored by transcriptomic changes in a cluster of genes that are involved in cholesterol metabolism. Analysis of this cluster revealed *TSC2*$^{-/-}$ cells have increased expression of cholesterol uptake and synthesis genes compared to WT, selectively when in hydrogel culture. Remarkably, I also observed global upregulation of cholesterol uptake genes in the *TSC2*$^{-/-}$ renal organoids compared to WT cells. While *TSC2*$^{-/-}$ cells have been previously reported to increase cholesterol uptake and biosynthesis in response to chloroquine treatment,[149] such a phenotype has not been reported in maintenance conditions, highlighting the novel biology unlocked by tissue-engineered systems.

Several studies have reported a role for HDAC inhibitors in cholesterol metabolism in cellular models of Niemann-Pick disease type C (NPC) using *NPC1*$^{-/-}$ cells.[150–155] In general, HDAC inhibitors reduce intracellular cholesterol levels to confer cholesterol clearance by an unknown mechanism. Thus, I propose the following hypothesis: *TSC2*$^{-/-}$ cells have an anabolic dependency on cholesterol, and upon treatment with HDAC inhibitors – which leads to decreased intracellular cholesterol bioavailability – the cells experience anabolic mismatch and trigger apoptosis. Future work will be required to test this hypothesis and unravel the mechanism of HDAC inhibitors as therapeutic agents against the mesenchymal manifestations of TSC.

The pathogenesis of mesenchymal TSC manifestations requires a new conceptual framework which reflects the etiological complexity

The histological diversity and divergent pathogenesis of TSC lesions is enigmatic. Tumors can form in many distinct sites, including the brain, skin, lungs, heart, and kidney.[2] Despite a common genetic etiology, the composition and timing of lesion formation varies

widely across affected tissues. For example, cardiac rhabdomyomas are solitary masses that form and subsequently regress during fetal development, often with no persistent abnormalities in adulthood.[156] This is in complete contrast to LAM, which predominately affects women, grows clinically symptomatic primarily in adulthood, and exhibits a diffuse cystic destruction pattern in the lungs.[44] The observation of divergent phenotypes arising from a common genetic etiology underscores the value of investigating tissue-specific mechanisms of pathogenesis.

In the early years of studying the molecular basis of RAMLs, a pathogenic model was proposed whereby biallelic inactivation of *TSC1/2* in a single renal progenitor cell type (not yet determined) leads to aberrant differentiation and proliferation, forming the histologically diverse constituents of the RAML.[157] This conceptual framework for understanding RAML pathogenesis has persisted in the field, galvanizing many studies in the quest to identify the "cell of origin".[78–81,158] However, in this thesis, I demonstrate that ablation of *TSC1/2* alters multiple developmental trajectories to confer pleiotropic features of TSC kidney disease. Thus, these data suggest that TSC renal lesions may instead arise from *multiple* cells of origins, with disease heterogeneity a reflection of the diverse progenitor populations acquiring second hit mutations during development.

A new conceptual framework is required to capture this etiological complexity. Thus, I present a new model of pathogenesis that posits two key features (**Figure 2**). First, TSC kidney lesions are a continuum of phenotypes, including RAMLs of varying composition and cystic lesions of varying etiology. Second, TSC kidney lesions initiate during development from multiple distinct yet closely related cells of origin.

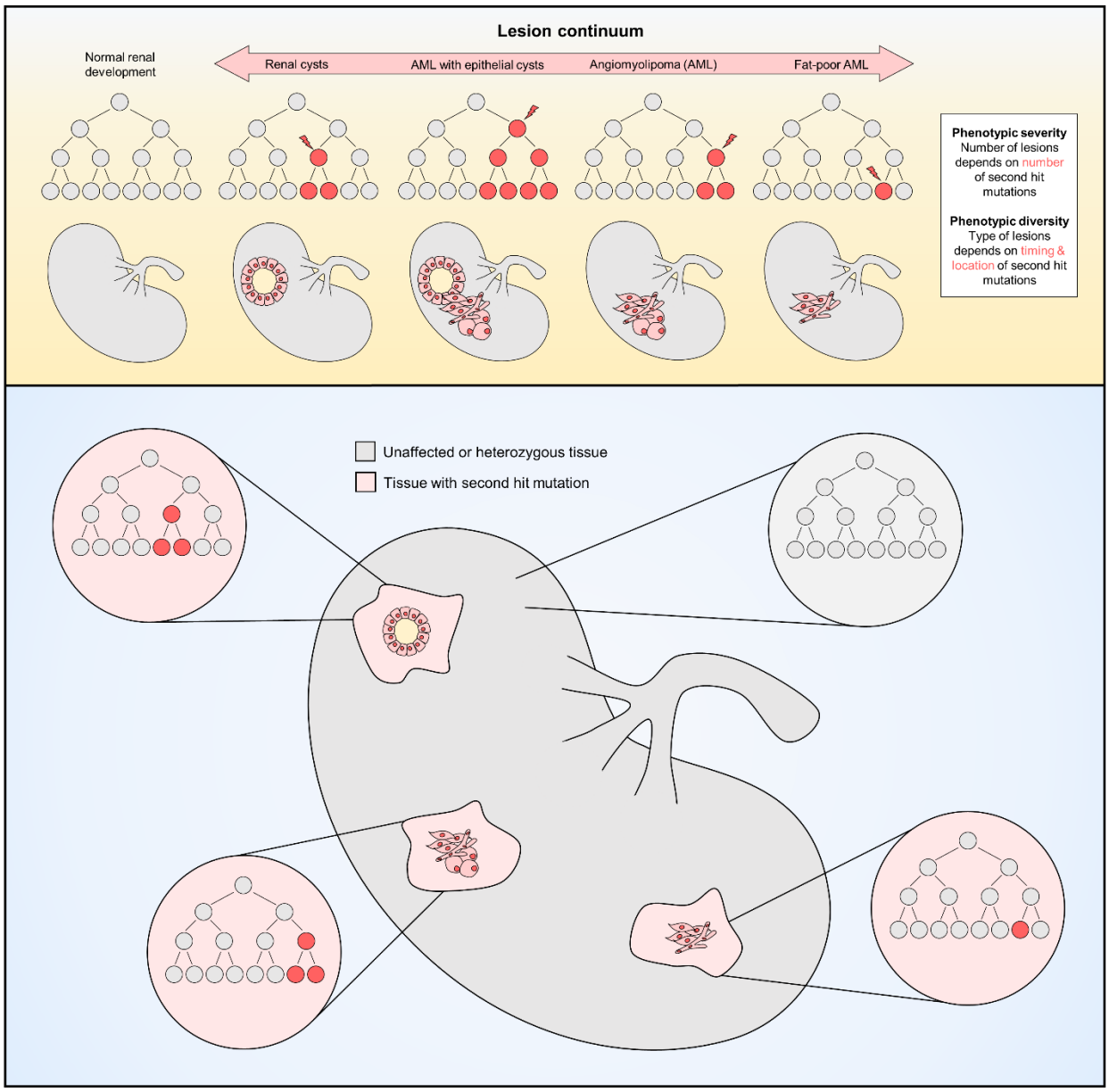

Figure 2: A new conceptual framework for TSC renal lesion pathogenesis.

A continuum of TSC renal phenotypes is likely intuitive, as nature does not exist as categorical phenomena but is rather discretized by the human psyche. Many pathological analyses of the TSC kidney have shown remarkable diversity in RAML and cyst morphology, size, cellular composition, and molecular expression.[23,24,26–29,159] The classic "triphasic" RAML is actually a minor phenotype, with most lesions skewing towards one or two lineages.[16,160]

Indeed, fat-poor RAML may even occur in up to one third of patients.[158] While lesion classification into angiomyolipoma and cysts is helpful- particularly in the clinical realm- conceptualization of a disease continuum is essential for interrogating pathobiology. The kidney lesion phenotypic continuum is well-illustrated by the rare variant of RAML termed RAML with epithelial cysts.[38] Although not definitely proven, there is evidence indicating the epithelial cysts are tumor-derived,[26,161,162] illustrating the phenotypically-diverse TSC kidney lesions may arise from overlapping processes. Acknowledgement of a continuum of disease phenotypes has precedence in TSC, where neuropsychiatric features can present as overlapping and with variable severity.[163] A continuum of phenotypes has also been described in closely-related mTORC1-driven cortical dysplasias.[164]

The postulation of multiple distinct yet closely related cells of origin is consistent with several disease characteristics. For example, while distinct TSC lesions may share similar second-hit events, many lesions possess distinct mutations.[54,55] The likelihood of these second hit events arising at the exact same time is low. In the context of development, where cell identity is transient and closely linked to developmental time, temporal stochasticity in second-hit events would confer distinct cells of origin. That is, the *when* and *where* of developmental mutagenesis is exquisitely intertwined. I postulate the phenotypic variability in kidney lesions seen within patients may be attributable to closely related but distinct cells of origin. For example, my renal organoid model demonstrates that *TSC1/2* ablation led to branching of a melanocytic population from a neural crest-derived $MITF^{+}$ Schwann cell precursor population. While this suggests Schwann cell precursors could be the progenitor population for the melanocytic features of RAML, other constituents may derive from distinct trajectories. A similar concept of multiple progenitors has been considered in the brain manifestations of TSC,

where variable developmental timing in somatic mutations leads to heterogeneity in cortical organoid phenotypes.[82] This concept has also been noted in a related renal cystic disorder, autosomal dominant polycystic kidney disease, in which the timing of *Pkd1* mutagenesis in a mouse model largely dictates phenotypic severity.[165]

I must note that other hypotheses could explain phenotypic variability, such as divergence in niche-specific factors during ontogenesis. I also cannot exclude the possibility of lesion formation from an adult tissue-resident cell type, particularly in the context of injury and regeneration.[166] However, such mechanisms are not mutually exclusive and may co-exist with aberrant differentiation of *bona fide* multipotent progenitor populations during development.

This model offers explanation for why an animal model recapitulating the entirety of human renal disease has yet to be established. Most genetically-engineered mice target *Tsc1/2* inactivation to all cells expressing a particular promoter. However, in this model, loss of *TSC1/2* is proposed to occur in a limited number of cells during development. Yet if *TSC1/2* inactivation is induced in an entire population of cells early in development, embryonic lethality or early mortality may ensue, preventing the formation of fulminant TSC lesions (e.g. as seen with *Tsc1/2* knockout under the *Wnt1* promoter).[110] Thus, animal models would benefit from employing stochastic knockout models early in development, recapitulating mosaicism seen in patients.

This model- proposed for TSC renal lesions based on my empirical data - also offers insights into pathogenesis of LAM. The suspected clonal origin of LAM cells and RAMLs[57,84,85] has for many years fueled the "benign metastasizing" mechanism of pathogenesis.[43,44,86] However, despite clinical LAM being precipitated in adulthood, recent work in human genetics and animal models[93,94] have supported the possibility of LAM as a disease of developmental

origin. The conceptual framework I propose offers a plausible mechanism, whereby low-level mosaicism affecting a common kidney-lung progenitor cell during development leads to the disease manifestations. Thus, TSC kidney and lung lesions should not be viewed as distinct entities, but rather overlapping processes which share a common ancestor.

Summary

The work presented in this thesis is a comprehensive investigation of the mesenchymal manifestations of TSC with tissue-engineered disease models. Using novel tools and techniques, I have sought to unravel disease biology in a manner informative to the research community, but ultimately of benefit to patients. As a hopefully positive prognostic, the work described here has generated just as many questions (if not, more) as it has answered. Novel insights into lesion pathogenesis and candidate therapeutic strategies have provided a foundation upon which to build, until the *raison d'être* of the study of human disease can be realized: the development of new therapeutic options which can improve the lives of patients.

REFERENCES

1. Salussolia, C. L., Klonowska, K., Kwiatkowski, D. J. & Sahin, M. Genetic Etiologies, Diagnosis, and Treatment of Tuberous Sclerosis Complex. *Annu. Rev. Genomics Hum. Genet.* (2019) doi:10.1146/annurev-genom-083118-015354.
2. Henske, E. P., Jóźwiak, S., Kingswood, J. C., Sampson, J. R. & Thiele, E. A. Tuberous sclerosis complex. *Nat. Rev. Dis. Primer* **2**, 1–18 (2016).
3. Jr, S., Sj, S., Jb, S., L, M. & Jm, C. Genetic aspects of tuberous sclerosis in the west of Scotland. *J. Med. Genet.* **26**, 28–31 (1989).
4. Osborne, J. P., Fryer, A. & Webb, D. Epidemiology of Tuberous Sclerosis. *Ann. N. Y. Acad. Sci.* **615**, 125–127 (1991).
5. Identification and characterization of the tuberous sclerosis gene on chromosome 16. *Cell* **75**, 1305–1315 (1993).
6. EVIDENCE THAT THE GENE FOR TUBEROUS SCLEROSIS IS ON CHROMOSOME 9. *The Lancet* **329**, 659–661 (1987).
7. Slegtenhorst, M. van *et al.* Identification of the Tuberous Sclerosis Gene TSC1 on Chromosome 9q34. *Science* **277**, 805–808 (1997).
8. HUANG, J. & MANNING, B. D. The TSC1–TSC2 complex: a molecular switchboard controlling cell growth. *Biochem. J.* **412**, 179–190 (2008).
9. Bissler, J. J. *et al.* Everolimus for angiomyolipoma associated with tuberous sclerosis complex or sporadic lymphangioleiomyomatosis (EXIST-2): a multicentre, randomised, double-blind, placebo-controlled trial. *The Lancet* **381**, 817–824 (2013).

10. French, J. A. *et al.* Adjunctive everolimus therapy for treatment-resistant focal-onset seizures associated with tuberous sclerosis (EXIST-3): a phase 3, randomised, double-blind, placebo-controlled study. *The Lancet* **388**, 2153–2163 (2016).
11. McCormack, F. X. *et al.* Efficacy and safety of sirolimus in lymphangioleiomyomatosis. *N. Engl. J. Med.* **364**, 1595–1606 (2011).
12. Bissler, J. J. *et al.* Sirolimus for Angiomyolipoma in Tuberous Sclerosis Complex or Lymphangioleiomyomatosis. *N. Engl. J. Med.* **358**, 140–151 (2008).
13. Franz, D. N. *et al.* Efficacy and safety of everolimus for subependymal giant cell astrocytomas associated with tuberous sclerosis complex (EXIST-1): a multicentre, randomised, placebo-controlled phase 3 trial. *The Lancet* **381**, 125–132 (2013).
14. Shepherd, C. W., Gomez, M. R., Lie, J. T. & Crowson, C. S. Causes of Death in Patients With Tuberous Sclerosis. *Mayo Clin. Proc.* **66**, 792–796 (1991).
15. Amin, S. *et al.* Causes of mortality in individuals with tuberous sclerosis complex. *Dev. Med. Child Neurol.* **59**, 612–617 (2017).
16. Thway, K. & Fisher, C. PEComa: morphology and genetics of a complex tumor family. *Ann. Diagn. Pathol.* **19**, 359–368 (2015).
17. Martignoni, G. *et al.* Molecular pathology of lymphangioleiomyomatosis and other perivascular epithelioid cell tumors. *Arch. Pathol. Lab. Med.* **134**, 33–40 (2010).
18. Zhe, X. & Schuger, L. Combined Smooth Muscle and Melanocytic Differentiation in Lymphangioleiomyomatosis. *J. Histochem. Cytochem.* **52**, 1537–1542 (2004).
19. Matsumoto, Y. *et al.* Markers of Cell Proliferation and Expression of Melanosomal Antigen in Lymphangioleiomyomatosis. *Am. J. Respir. Cell Mol. Biol.* **21**, 327–336 (1999).

20. Bonetti, F. *et al.* Transbronchial biopsy in lymphangiomyomatosis of the lung. HMB45 for diagnosis. *Am. J. Surg. Pathol.* **17**, 1092–1102 (1993).

21. Berger, U., Khaghani, A., Pomerance, A., Yacoub, M. H. & Coombes, R. C. Pulmonary lymphangioleiomyomatosis and steroid receptors. An immunocytochemical study. *Am. J. Clin. Pathol.* **93**, 609–614 (1990).

22. Fetsch, P. A. *et al.* Comparison of melanoma antigen recognized by T cells (MART-1) to HMB-45: additional evidence to support a common lineage for angiomyolipoma, lymphangiomyomatosis, and clear cell sugar tumor. *Mod. Pathol. Off. J. U. S. Can. Acad. Pathol. Inc* **11**, 699–703 (1998).

23. Chan, J. K. C. *et al.* Lymphangiomyomatosis and angiomyolipoma: closely related entities characterized by hamartomatous proliferation of HMB-45-positive smooth muscle. *Histopathology* **22**, 445–455 (1993).

24. Chilosi, M. *et al.* Cathepsin-k expression in pulmonary lymphangioleiomyomatosis. *Mod. Pathol.* **22**, 161–166 (2009).

25. D'Armiento, J. *et al.* Identification of the Benign Mesenchymal Tumor Gene HMGA2 in Lymphangiomyomatosis. *Cancer Res.* **67**, 1902–1909 (2007).

26. Siroky, B. J., Yin, H. & Bissler, J. J. Clinical and Molecular Insights into Tuberous Sclerosis Complex Renal Disease. *Pediatr. Nephrol.* **26**, 839–852 (2011).

27. Ashfaq, R., Weinberg, A. G. & Albores-Saavedra, J. Renal angiomyolipomas and HMB-45 reactivity. *Cancer* **71**, 3091–3097 (1993).

28. Jungbluth, A. A. *et al.* Expression of melanocyte-associated markers gp-100 and Melan-A/MART-1 in angiomyolipomas. *Virchows Arch.* **434**, 429–435 (1999).

29. D'Armiento, J. *et al.* Mesenchymal Tumorigenesis Driven by TSC2 Haploinsufficiency Requires HMGA2 and Is Independent of mTOR Pathway Activation. *Cancer Res.* (2016) doi:10.1158/0008-5472.CAN-15-1287.

30. Lam, H. C., Siroky, B. J. & Henske, E. P. Renal disease in tuberous sclerosis complex: pathogenesis and therapy. *Nat. Rev. Nephrol.* **14**, 704–716 (2018).

31. Cook, J. A., Oliver, K., Mueller, R. F. & Sampson, J. A cross sectional study of renal involvement in tuberous sclerosis. *J. Med. Genet.* **33**, 480–484 (1996).

32. Rakowski, S. K. *et al.* Renal manifestations of tuberous sclerosis complex: Incidence, prognosis, and predictive factors. *Kidney Int.* **70**, 1777–1782 (2006).

33. O'Callaghan, F. J., Noakes, M. J., Martyn, C. N. & Osborne, J. P. An epidemiological study of renal pathology in tuberous sclerosis complex. *BJU Int.* **94**, 853–857 (2004).

34. Casper, K. A., Donnelly, L. F., Chen, B. & Bissler, J. J. Tuberous Sclerosis Complex: Renal Imaging Findings. *Radiology* **225**, 451–456 (2002).

35. Ewalt, D. H., Sheffield, E., Sparagana, S. P., Delgado, M. R. & Roach, E. S. Renal lesion growth in children with tuberous sclerosis complex. *J. Urol.* **160**, 141–145 (1998).

36. Tsai, J.-D., Wei, C.-C., Chen, S.-M., Lue, K.-H. & Sheu, J.-N. Association between the growth rate of renal cysts/angiomyolipomas and age in the patients with tuberous sclerosis complex. *Int. Urol. Nephrol.* **46**, 1685–1690 (2014).

37. Kingswood, J. C. *et al.* Renal Manifestations of Tuberous Sclerosis Complex: Key Findings From the Final Analysis of the TOSCA Study Focussing Mainly on Renal Angiomyolipomas. *Front. Neurol.* **11**, (2020).

38. LeRoy, M. A. & Rao, P. Angiomyolipoma With Epithelial Cysts. *Arch. Pathol. Lab. Med.* **140**, 594–597 (2016).

39. Fittschen, A. *et al.* Prevalence of sporadic renal angiomyolipoma: a retrospective analysis of 61,389 in- and out-patients. *Abdom. Imaging* **39**, 1009–1013 (2014).

40. Abbott, G. F. *et al.* From the archives of the AFIP: lymphangioleiomyomatosis: radiologic-pathologic correlation. *Radiogr. Rev. Publ. Radiol. Soc. N. Am. Inc* **25**, 803–828 (2005).

41. Chu, S. C. *et al.* Comprehensive Evaluation of 35 Patients With Lymphangioleiomyomatosis. *Chest* **115**, 1041–1052 (1999).

42. Urban, T. *et al.* Pulmonary lymphangioleiomyomatosis. A study of 69 patients. Groupe d'Etudes et de Recherche sur les Maladies 'Orphelines' Pulmonaires (GERM"O"P). *Medicine (Baltimore)* **78**, 321–337 (1999).

43. McCormack, F. X., Travis, W. D., Colby, T. V., Henske, E. P. & Moss, J. Lymphangioleiomyomatosis, Calling it What it is: A low-grade, destructive, metastasizing neoplasm. *Am. J. Respir. Crit. Care Med.* **186**, 1210–1212 (2012).

44. Henske, E. P. & McCormack, F. X. Lymphangioleiomyomatosis — a wolf in sheep's clothing. *J. Clin. Invest.* **122**, 3807–3816 (2012).

45. Ryu, J. H. *et al.* The NHLBI Lymphangioleiomyomatosis Registry. *Am. J. Respir. Crit. Care Med.* **173**, 105–111 (2006).

46. Costello, L. C., Hartman, T. E. & Ryu, J. H. High frequency of pulmonary lymphangioleiomyomatosis in women with tuberous sclerosis complex. *Mayo Clin. Proc.* **75**, 591–594 (2000).

47. Moss, J. *et al.* Prevalence and Clinical Characteristics of Lymphangioleiomyomatosis (LAM) in Patients with Tuberous Sclerosis Complex. *Am. J. Respir. Crit. Care Med.* **164**, 669–671 (2001).

48. Kristof, A. S., Zhi Li, P., Major, P. & Landry, J. S. Lymphangioleiomyomatosis and Tuberous Sclerosis Complex in Quebec: Prevalence and Health-care Utilization. *Chest* **148**, 444–449 (2015).

49. Harknett, E. C. *et al.* Use of variability in national and regional data to estimate the prevalence of lymphangioleiomyomatosis. *QJM Int. J. Med.* **104**, 971–979 (2011).

50. Green, A. J., Smith, M. & Yates, J. R. W. Loss of heterozygosity on chromosome 16p13.3 in hamartomas from tuberous sclerosis patients. *Nat. Genet.* **6**, 193–196 (1994).

51. Giannikou, K. *et al.* Low-level mosaicism in tuberous sclerosis complex: prevalence, clinical features, and risk of disease transmission. *Genet. Med.* 1 (2019) doi:10.1038/s41436-019-0562-6.

52. Tyburczy, M. E. *et al.* Mosaic and Intronic Mutations in TSC1/TSC2 Explain the Majority of TSC Patients with No Mutation Identified by Conventional Testing. *PLoS Genet.* **11**, e1005637 (2015).

53. Verhoef, S. *et al.* High rate of mosaicism in tuberous sclerosis complex. *Am. J. Hum. Genet.* **64**, 1632–1637 (1999).

54. Giannikou, K. *et al.* Whole Exome Sequencing Identifies TSC1/TSC2 Biallelic Loss as the Primary and Sufficient Driver Event for Renal Angiomyolipoma Development. *PLOS Genet.* **12**, e1006242 (2016).

55. Martin, K. R. *et al.* The genomic landscape of tuberous sclerosis complex. *Nat. Commun.* **8**, 15816 (2017).

56. Qin, W. *et al.* Angiomyolipoma Have Common Mutations in TSC2 but No Other Common Genetic Events. *PLOS ONE* **6**, e24919 (2011).

57. Sato, T. *et al.* Mutation analysis of the TSC1 and TSC2 genes in Japanese patients with pulmonary lymphangioleiomyomatosis. *J. Hum. Genet.* **47**, 20–28 (2002).

58. Jones, A. C. *et al.* Molecular Genetic and Phenotypic Analysis Reveals Differences between TSC1 and TSC2 Associated Familial and Sporadic Tuberous Sclerosis. *Hum. Mol. Genet.* **6**, 2155–2161 (1997).

59. Jones, A. C. *et al.* Comprehensive mutation analysis of TSC1 and TSC2-and phenotypic correlations in 150 families with tuberous sclerosis. *Am. J. Hum. Genet.* **64**, 1305–1315 (1999).

60. Dabora, S. L. *et al.* Mutational Analysis in a Cohort of 224 Tuberous Sclerosis Patients Indicates Increased Severity of TSC2, Compared with TSC1, Disease in Multiple Organs. *Am. J. Hum. Genet.* **68**, 64–80 (2001).

61. Sancak, O. *et al.* Mutational analysis of the TSC1 and TSC2 genes in a diagnostic setting: genotype – phenotype correlations and comparison of diagnostic DNA techniques in Tuberous Sclerosis Complex. *Eur. J. Hum. Genet.* **13**, 731 (2005).

62. Au, K. S. *et al.* Genotype/phenotype correlation in 325 individuals referred for a diagnosis of tuberous sclerosis complex in the United States. *Genet. Med.* **9**, 88–100 (2007).

63. Curatolo, P., Moavero, R., Roberto, D. & Graziola, F. Genotype/Phenotype Correlations in Tuberous Sclerosis Complex. *Semin. Pediatr. Neurol.* **22**, 259–273 (2015).

64. Dibble, C. C. *et al.* TBC1D7 Is a Third Subunit of the TSC1-TSC2 Complex Upstream of mTORC1. *Mol. Cell* **47**, 535–546 (2012).

65. van Slegtenhorst, M. *et al.* Interaction Between Hamartin and Tuberin, the TSC1 and TSC2 Gene Products. *Hum. Mol. Genet.* **7**, 1053–1057 (1998).

66. Inoki, K., Li, Y., Xu, T. & Guan, K.-L. Rheb GTPase is a direct target of TSC2 GAP activity and regulates mTOR signaling. *Genes Dev.* **17**, 1829–1834 (2003).

67. Groenewoud, M. J. & Zwartkruis, F. J. T. Rheb and Rags come together at the lysosome to activate mTORC1. *Biochem. Soc. Trans.* **41**, 951–955 (2013).

68. Kim, D.-H. *et al.* mTOR Interacts with Raptor to Form a Nutrient-Sensitive Complex that Signals to the Cell Growth Machinery. *Cell* **110**, 163–175 (2002).

69. Peterson, T. R. *et al.* DEPTOR Is an mTOR Inhibitor Frequently Overexpressed in Multiple Myeloma Cells and Required for Their Survival. *Cell* **137**, 873–886 (2009).

70. Kim, D.-H. *et al.* GβL, a Positive Regulator of the Rapamycin-Sensitive Pathway Required for the Nutrient-Sensitive Interaction between Raptor and mTOR. *Mol. Cell* **11**, 895–904 (2003).

71. Sancak, Y. *et al.* PRAS40 Is an Insulin-Regulated Inhibitor of the mTORC1 Protein Kinase. *Mol. Cell* **25**, 903–915 (2007).

72. Laplante, M. & Sabatini, D. M. mTOR signaling in growth control and disease. *Cell* **149**, 274–293 (2012).

73. Saxton, R. A. & Sabatini, D. M. mTOR Signaling in Growth, Metabolism, and Disease. *Cell* **168**, 960–976 (2017).

74. Valvezan, A. J. & Manning, B. D. Molecular logic of mTORC1 signalling as a metabolic rheostat. *Nat. Metab.* **1**, 321–333 (2019).

75. Yang, H. *et al.* Mechanisms of mTORC1 activation by RHEB and inhibition by PRAS40. *Nature* **552**, 368–373 (2017).

76. Karbowniczek, M., Yu, J. & Henske, E. P. Renal Angiomyolipomas from Patients with Sporadic Lymphangiomyomatosis Contain Both Neoplastic and Non-Neoplastic Vascular Structures. *Am. J. Pathol.* **162**, 491–500 (2003).

77. Green, A. J., Sepp, T. & Yates, J. R. W. Clonality of tuberous sclerosis harmatomas shown by non-random X-chromosome inactivation. *Hum. Genet.* **97**, 240–243 (1996).

78. Siroky, B. J. *et al.* Evidence for pericyte origin of TSC-associated renal angiomyolipomas and implications for angiotensin receptor inhibition therapy. *Am. J. Physiol. - Ren. Physiol.* **307**, F560–F570 (2014).

79. Yue, M. *et al.* Evidence Supporting a Lymphatic Endothelium Origin for Angiomyolipoma, a TSC2− Tumor Related to Lymphangioleiomyomatosis. *Am. J. Pathol.* **186**, 1825–1836 (2016).

80. Gonçalves, A. F. *et al.* Evidence of renal angiomyolipoma neoplastic stem cells arising from renal epithelial cells. *Nat. Commun.* **8**, 1466 (2017).

81. Delaney, S. P., Julian, L. M. & Stanford, W. L. The neural crest lineage as a driver of disease heterogeneity in Tuberous Sclerosis Complex and Lymphangioleiomyomatosis. *Front. Cell Dev. Biol.* **2**, (2014).

82. Blair, J. D., Hockemeyer, D. & Bateup, H. S. Genetically engineered human cortical spheroid models of tuberous sclerosis. *Nat. Med.* **24**, 1568–1578 (2018).

83. Delaney, S. P. *et al.* Human pluripotent stem cell modeling of tuberous sclerosis complex reveals lineage-specific therapeutic vulnerabilities. *bioRxiv* 683359 (2020) doi:10.1101/683359.

84. Carsillo, T., Astrinidis, A. & Henske, E. P. Mutations in the tuberous sclerosis complex gene TSC2 are a cause of sporadic pulmonary lymphangioleiomyomatosis. *Proc. Natl. Acad. Sci.* **97**, 6085–6090 (2000).

85. Yu, J., Astrinidis, A. & Henske, E. P. Chromosome 16 Loss of Heterozygosity in Tuberous Sclerosis and Sporadic Lymphangiomyomatosis. *Am. J. Respir. Crit. Care Med.* **164**, 1537–1540 (2001).

86. Henske, E. P. Metastasis of benign tumor cells in tuberous sclerosis complex. *Genes. Chromosomes Cancer* **38**, 376–381 (2003).

87. Cai, X. *et al.* Phenotypic Characterization of Disseminated Cells with TSC2 Loss of Heterozygosity in Patients with Lymphangioleiomyomatosis. *Am. J. Respir. Crit. Care Med.* **182**, 1410–1418 (2010).

88. Crooks, D. M. *et al.* Molecular and genetic analysis of disseminated neoplastic cells in lymphangioleiomyomatosis. *Proc. Natl. Acad. Sci.* **101**, 17462–17467 (2004).

89. Bittmann, I., Rolf, B., Amann, G. & Löhrs, U. Recurrence of lymphangioleiomyomatosis after single lung transplantation: New insights into pathogenesis. *Hum. Pathol.* **34**, 95–98 (2003).

90. Karbowniczek, M. *et al.* Recurrent Lymphangiomyomatosis after Transplantation. *Am. J. Respir. Crit. Care Med.* **167**, 976–982 (2003).

91. Henske, E. P. Metastasis of benign tumor cells in tuberous sclerosis complex. *Genes. Chromosomes Cancer* **38**, 376–381 (2003).

92. Hayashi, T. *et al.* Prevalence of uterine and adnexal involvement in pulmonary lymphangioleiomyomatosis: a clinicopathologic study of 10 patients. *Am. J. Surg. Pathol.* **35**, 1776–1785 (2011).

93. Ogórek, B. *et al.* Generalised mosaicism for TSC2 mutation in isolated lymphangioleiomyomatosis. *Eur. Respir. J.* **54**, (2019).

94. Obraztsova, K. *et al.* mTORC1 activation in lung mesenchyme drives sex- and age-dependent pulmonary structure and function decline. *Nat. Commun.* **11**, 1–15 (2020).

95. Yu, J., Astrinidis, A., Howard, S. & Henske, E. P. Estradiol and tamoxifen stimulate LAM-associated angiomyolipoma cell growth and activate both genomic and nongenomic signaling pathways. *Am. J. Physiol. Lung Cell. Mol. Physiol.* **286**, L694-700 (2004).

96. Siroky, B. J. *et al.* Human TSC-associated renal angiomyolipoma cells are hypersensitive to ER stress. *Am. J. Physiol.-Ren. Physiol.* **303**, F831–F844 (2012).

97. Goncharova, E. A. *et al.* Tuberin regulates p70 S6 kinase activation and ribosomal protein S6 phosphorylation. A role for the TSC2 tumor suppressor gene in pulmonary lymphangioleiomyomatosis (LAM). *J. Biol. Chem.* **277**, 30958–30967 (2002).

98. Kobayashi, T. *et al.* A germ-line Tsc1 mutation causes tumor development and embryonic lethality that are similar, but not identical to, those caused by Tsc2 mutation in mice. *Proc. Natl. Acad. Sci.* **98**, 8762–8767 (2001).

99. Kwiatkowski, D. J. *et al.* A mouse model of TSC1 reveals sex-dependent lethality from liver hemangiomas, and up-regulation of p70S6 kinase activity in Tsc1 null cells. *Hum. Mol. Genet.* **11**, 525–534 (2002).

100. Zhou, J., Brugarolas, J. & Parada, L. F. Loss of Tsc1, but not Pten, in renal tubular cells causes polycystic kidney disease by activating mTORC1. *Hum. Mol. Genet.* **18**, 4428–4441 (2009).

101. Armour, E. A., Carson, R. P. & Ess, K. C. Cystogenesis and elongated primary cilia in Tsc1-deficient distal convoluted tubules. *Am. J. Physiol.-Ren. Physiol.* **303**, F584–F592 (2012).

102. Traykova-Brauch, M. *et al.* An efficient and versatile system for acute and chronic modulation of renal tubular function in transgenic mice. *Nat. Med.* **14**, 979–984 (2008).

103. Wu, Z. *et al.* Tsc1 ablation in Prx1 and Osterix lineages causes renal cystogenesis in mouse. *Sci. Rep.* **9**, 837 (2019).

104. Fang, Y. *et al.* Metformin effectively treats Tsc1 deletion-caused kidney pathology by upregulating AMPK phosphorylation. *Cell Death Discov.* **6**, (2020).

105. Gewin, L. *et al.* Inactivation of Tsc2 in Abcg2 Lineage Derived Cells Drives the Appearance of Polycystic Lesions and Fibrosis in the Adult Kidney. *Am. J. Physiol. Renal Physiol.* (2019) doi:10.1152/ajprenal.00629.2018.

106. Barone, S. *et al.* Kidney intercalated cells and the transcription factor FOXi1 drive cystogenesis in tuberous sclerosis complex. *Proc. Natl. Acad. Sci.* **118**, (2021).

107. Pema, M. *et al.* mTORC1-mediated inhibition of polycystin-1 expression drives renal cyst formation in tuberous sclerosis complex. *Nat. Commun.* **7**, 10786 (2016).

108. Bissler, J. J. *et al.* Tuberous sclerosis complex exhibits a new renal cystogenic mechanism. *Physiol. Rep.* **7**, e13983 (2019).

109. Prizant, H. *et al.* Uterine-specific loss of Tsc2 leads to myometrial tumors in both the uterus and lungs. *Mol. Endocrinol. Baltim. Md* **27**, 1403–1414 (2013).

110. Kwiatkowski, D. J. Animal Models of Lymphangioleiomyomatosis (LAM) and Tuberous Sclerosis Complex (TSC). *Lymphat. Res. Biol.* **8**, 51–57 (2010).

111. Fang, F. *et al.* Neural Crest-Specific TSC1 Deletion in Mice Leads to Sclerotic Craniofacial Bone Lesion. *J. Bone Miner. Res. Off. J. Am. Soc. Bone Miner. Res.* **30**, 1195–1205 (2015).

112. Liu, H.-J. *et al.* TSC2-deficient tumors have evidence of T cell exhaustion and respond to anti–PD-1/anti–CTLA-4 immunotherapy. *JCI Insight* **3**,.

113. Maisel, K. *et al.* Immune Checkpoint Ligand PD-L1 is Upregulated in Pulmonary Lymphangioleiomyomatosis (LAM). *Am. J. Respir. Cell Mol. Biol.* (2018) doi:10.1165/rcmb.2018-0123OC.

114. Li, C. *et al.* Faslodex Inhibits Estradiol-Induced Extracellular Matrix Dynamics and Lung Metastasis in a Model of Lymphangioleiomyomatosis. *Am. J. Respir. Cell Mol. Biol.* **49**, 135–142 (2013).

115. Goncharova, E. A. *et al.* Prevention of Alveolar Destruction and Airspace Enlargement in a Mouse Model of Pulmonary Lymphangioleiomyomatosis (LAM). *Sci. Transl. Med.* **4**, 154ra134-154ra134 (2012).

116. Yu, J. J. *et al.* Estrogen promotes the survival and pulmonary metastasis of tuberin-null cells. *Proc. Natl. Acad. Sci. U. S. A.* **106**, 2635–2640 (2009).

117. Sun, Y. *et al.* Progesterone and Estradiol Synergistically Promote the Lung Metastasis of Tuberin-Deficient Cells in a Preclinical Model of Lymphangioleiomyomatosis. *Horm. Cancer* **5**, 284–298 (2014).

118. Goncharova, E. A. *et al.* mTORC2 Is Required for Proliferation and Survival of TSC2-Null Cells. *Mol. Cell. Biol.* **31**, 2484–2498 (2011).

119. Lesma, E. *et al.* Development of a Lymphangioleiomyomatosis Model by Endonasal Administration of Human TSC2−/− Smooth Muscle Cells in Mice. *Am. J. Pathol.* **181**, 947–960 (2012).

120. Liu, F. *et al.* Real-time monitoring of tumorigenesis, dissemination, & drug response in a preclinical model of lymphangioleiomyomatosis/tuberous sclerosis complex. *PloS One* **7**, e38589 (2012).

121. Taveira-DaSilva, A. M., Hathaway, O., Stylianou, M. & Moss, J. Changes in lung function and chylous effusions in patients with lymphangioleiomyomatosis treated with sirolimus. *Ann. Intern. Med.* **154**, 797–805, W-292–293 (2011).

122. Dabora, S. L. *et al.* Multicenter phase 2 trial of sirolimus for tuberous sclerosis: kidney angiomyolipomas and other tumors regress and VEGF- D levels decrease. *PloS One* **6**, e23379 (2011).

123. Bee, J., Fuller, S., Miller, S. & Johnson, S. R. Lung function response and side effects to rapamycin for lymphangioleiomyomatosis: a prospective national cohort study. *Thorax* **73**, 369–375 (2018).

124. Yao, J. *et al.* Sustained effects of sirolimus on lung function and cystic lung lesions in lymphangioleiomyomatosis. *Am. J. Respir. Crit. Care Med.* **190**, 1273–1282 (2014).

125. Takada, T. *et al.* Efficacy and Safety of Long-Term Sirolimus Therapy for Asian Patients with Lymphangioleiomyomatosis. *Ann. Am. Thorac. Soc.* **13**, 1912–1922 (2016).

126. McCormack, F. X. *et al.* Efficacy and Safety of Sirolimus in Lymphangioleiomyomatosis. *http://dx.doi.org/10.1056/NEJMoa1100391* https://www.nejm.org/doi/full/10.1056/NEJMoa1100391?casa_token=S05qwimB6skAAAAA%3Aq3iC7Pw7kbsa8mCnhHJjGlnQ2sdrjsqKwMSB7T84PdjhTtWlq3OAbNsQpkTJuagCJIRjH83ekTFY (2011) doi:10.1056/NEJMoa1100391.

127. Parkhitko, A. *et al.* Tumorigenesis in tuberous sclerosis complex is autophagy and p62/sequestosome 1 (SQSTM1)-dependent. *Proc. Natl. Acad. Sci.* **108**, 12455–12460 (2011).

128. Medvetz, D., Priolo, C. & Henske, E. P. Therapeutic Targeting of Cellular Metabolism in Cells with Hyperactive mTORC1: A Paradigm Shift. *Mol. Cancer Res.* **13**, 3–8 (2015).

129. Khademhosseini, A. & Langer, R. A decade of progress in tissue engineering. *Nat. Protoc.* **11**, 1775–1781 (2016).

130. Tayler, I. M. & Stowers, R. S. Engineering hydrogels for personalized disease modeling and regenerative medicine. *Acta Biomater.* (2021) doi:10.1016/j.actbio.2021.04.020.

131. Shannon, A. E., Boos, C. E. & Hummon, A. B. Co-culturing multicellular tumor models: Modeling the tumor microenvironment and analysis techniques. *PROTEOMICS* **21**, 2000103 (2021).

132. Li, M. & Izpisua Belmonte, J. C. Organoids — Preclinical Models of Human Disease. *N. Engl. J. Med.* **380**, 569–579 (2019).

133. Rowe, R. G. & Daley, G. Q. Induced pluripotent stem cells in disease modelling and drug discovery. *Nat. Rev. Genet.* **20**, 377–388 (2019).

134. Shi, Y., Inoue, H., Wu, J. C. & Yamanaka, S. Induced pluripotent stem cell technology: a decade of progress. *Nat. Rev. Drug Discov.* **16**, 115–130 (2017).

135. G. Nadadhur, A. *et al.* Neuron-Glia Interactions Increase Neuronal Phenotypes in Tuberous Sclerosis Complex Patient iPSC-Derived Models. *Stem Cell Rep.* **12**, 42–56 (2018).

136. Zucco, A. J. *et al.* Neural progenitors derived from Tuberous Sclerosis Complex patients exhibit attenuated PI3K/AKT signaling and delayed neuronal differentiation. *Mol. Cell. Neurosci.* **92**, 149–163 (2018).

137. Li, Y. *et al.* Abnormal Neural Progenitor Cells Differentiated from Induced Pluripotent Stem Cells Partially Mimicked Development of TSC2 Neurological Abnormalities. *Stem Cell Rep.* **8**, 883–893 (2017).

138. Grabole, N. *et al.* Genomic analysis of the molecular neuropathology of tuberous sclerosis using a human stem cell model. *Genome Med.* **8**, 94 (2016).

139. Costa, V. *et al.* mTORC1 Inhibition Corrects Neurodevelopmental and Synaptic Alterations in a Human Stem Cell Model of Tuberous Sclerosis. *Cell Rep.* **15**, 86–95 (2016).

140. Sundberg, M. *et al.* Purkinje cells derived from TSC patients display hypoexcitability and synaptic deficits associated with reduced FMRP levels and reversed by rapamycin. *Mol. Psychiatry* **23**, 2167–2183 (2018).

141. Babaei-Jadidi, R. *et al.* Mast Cell Tryptase Release Contributes to Disease Progression in Lymphangioleiomyomatosis. *Am. J. Respir. Crit. Care Med.* (2021) doi:10.1164/rccm.202007-2854OC.

142. Caliari, S. R. & Burdick, J. A. A practical guide to hydrogels for cell culture. *Nat. Methods* **13**, 405–414 (2016).

143. Velez, D. O. *et al.* 3D collagen architecture regulates cell adhesion through degradability, thereby controlling metabolic and oxidative stress. *Integr. Biol.* **11**, 221–234 (2019).

144. Gan, B., Yoo, Y. & Guan, J.-L. Association of Focal Adhesion Kinase with Tuberous Sclerosis Complex 2 in the Regulation of S6 Kinase Activation and Cell Growth. *J. Biol. Chem.* **281**, 37321–37329 (2006).

145. Garreta, E. *et al.* Fine tuning the extracellular environment accelerates the derivation of kidney organoids from human pluripotent stem cells. *Nat. Mater.* **18**, 397–405 (2019).

146. Takasato, M. *et al.* Kidney organoids from human iPS cells contain multiple lineages and model human nephrogenesis. *Nature* **526**, 564–568 (2015).

147. Kim, J., Koo, B.-K. & Knoblich, J. A. Human organoids: model systems for human biology and medicine. *Nat. Rev. Mol. Cell Biol.* **21**, 571–584 (2020).

148. Newbold, A., Falkenberg, K. J., Prince, H. M. & Johnstone, R. W. How do tumor cells respond to HDAC inhibition? *FEBS J.* **283**, 4032–4046 (2016).

149. Filippakis, H. *et al.* Lysosomal regulation of cholesterol homeostasis in tuberous sclerosis complex is mediated via NPC1 and LDL-R. *Oncotarget* **8**, 38099–38112 (2017).

150. Munkacsi, A. B. *et al.* An "Exacerbate-reverse" Strategy in Yeast Identifies Histone Deacetylase Inhibition as a Correction for Cholesterol and Sphingolipid Transport Defects in Human Niemann-Pick Type C Disease *♦. *J. Biol. Chem.* **286**, 23842–23851 (2011).

151. Helquist, P., Maxfield, F. R., Wiech, N. L. & Wiest, O. Treatment of Niemann–Pick Type C Disease by Histone Deacetylase Inhibitors. *Neurotherapeutics* **10**, 688–697 (2013).

152. Cruz, D. L. *et al.* Inhibition of Histone Deacetylases 1, 2, and 3 Enhances Clearance of Cholesterol Accumulation in Niemann-Pick C1 Fibroblasts. *ACS Pharmacol. Transl. Sci.* **4**, 1136–1148 (2021).

153. Pipalia, N. H. *et al.* Histone deacetylase inhibitors correct the cholesterol storage defect in most Niemann-Pick C1 mutant cells. *J. Lipid Res.* **58**, 695–708 (2017).

154. Pipalia, N. H. *et al.* Histone deacetylase inhibitor treatment dramatically reduces cholesterol accumulation in Niemann-Pick type C1 mutant human fibroblasts. *Proc. Natl. Acad. Sci.* **108**, 5620–5625 (2011).

155. Subramanian, K. *et al.* Correction of Niemann-Pick type C1 trafficking and activity with the histone deacetylase inhibitor valproic acid. *J. Biol. Chem.* **295**, 8017–8035 (2020).

156. Bader, R. S. *et al.* Fetal rhabdomyoma: prenatal diagnosis, clinical outcome, and incidence of associated tuberous sclerosis complex. *J. Pediatr.* **143**, 620–624 (2003).

157. Henske, E. P. Tuberous sclerosis and the kidney: from mesenchyme to epithelium, and beyond. *Pediatr. Nephrol. Berl. Ger.* **20**, 854–857 (2005).

158. Bissler, J. J. & Kingswood, J. C. Renal manifestation of tuberous sclerosis complex. *Am. J. Med. Genet. C Semin. Med. Genet.* **178**, 338–347 (2018).

159. Nair, N. *et al.* Renal Manifestations of Tuberous Sclerosis Complex. *J. Kidney Cancer VHL* **7**, 5–19 (2020).

160. Nonomura, A. *et al.* Angiomyolipoma of the liver: a reappraisal of morphological features and delineation of new characteristic histological features from the clinicopathological findings of 55 tumours in 47 patients. *Histopathology* **61**, 863–880 (2012).

161. Davis, C. J., Barton, J. H. & Sesterhenn, I. A. Cystic angiomyolipoma of the kidney: a clinicopathologic description of 11 cases. *Mod. Pathol.* **19**, 669–674 (2006).

162. Filho, J. do E. P. *et al.* Renal epithelioid angiomyolipoma with epithelial cysts: demonstration of Melan A and HMB45 positivity in the cystic epithelial lining. *Ann. Diagn. Pathol.* **16**, 397–401 (2012).

163. de Vries, P. J. *et al.* Tuberous Sclerosis Associated Neuropsychiatric Disorders (TAND) and the TAND Checklist. *Pediatr. Neurol.* **52**, 25–35 (2015).

164. D'Gama, A. M. *et al.* Somatic mutations activating the mTOR pathway in dorsal telencephalic progenitors cause a continuum of cortical dysplasias. *Cell Rep.* **21**, 3754–3766 (2017).

165. Lantinga-van Leeuwen, I. S. *et al.* Kidney-specific inactivation of the Pkd1 gene induces rapid cyst formation in developing kidneys and a slow onset of disease in adult mice. *Hum. Mol. Genet.* **16**, 3188–3196 (2007).
166. Chang-Panesso, M. & Humphreys, B. D. Cellular plasticity in kidney injury and repair. *Nat. Rev. Nephrol.* **13**, 39–46 (2017).

Data Chapter #1

Three-dimensional drug screen identifies HDAC inhibitors as therapeutic agents in mTORC1-driven lymphangioleiomyomatosis

Authors: Adam Pietrobon[1,2,3], Julien Yockell-Lelièvre[1,3], Nicole Melong[4], Laura J. Smith[5,6,7], Sean P. Delaney[1,2,3], Nadine Azzam[4], Chang Xue[6,7], Nishanth Merwin[8], Eric Lian[1,2,3], Alberto Camacho-Magallanes[1,2,3], Carole Doré[1], Gabriel Musso[8], Lisa M. Julian[9], Arnold S. Kristof[10], Roger Y. Tam[11], Jason N. Berman[2,4], Molly S. Shoichet[5,6,7,12], William L. Stanford[1,2,3]*

Affiliations:
[1] The Sprott Centre for Stem Cell Research, Regenerative Medicine Program, Ottawa Hospital Research Institute; Ottawa, Canada.
[2] Department of Cellular and Molecular Medicine, University of Ottawa; Ottawa, Canada.
[3] Ottawa Institute of Systems Biology; Ottawa, Canada.
[4] Department of Pediatrics, CHEO Research Institute; Ottawa, Canada.
[5] Department of Chemical Engineering and Applied Chemistry, University of Toronto; Toronto, Canada.
[6] Institute for Biomaterials and Biomedical Engineering, University of Toronto; Toronto, Canada.
[7] The Donnelly Centre for Cellular and Biomolecular Research; Toronto, Canada.
[8] BioSymetrics, Inc; Toronto, Canada.
[9] Centre for Cell Biology, Development, and Disease, Department of Biological Sciences, Simon Fraser University; Burnaby, Canada.
[10] Meakins-Christie Laboratories and Translational Research in Respiratory Diseases Program, Research Institute of the McGill University Health Centre, Faculty of Medicine, Departments of Medicine and Critical Care; Montreal, Canada.
[11] Centre for Biologics Evaluation, Biologic and Radiopharmaceutical Drugs Directorate, Health Canada; Ottawa, Canada.
[12] Department of Chemistry, University of Toronto; Toronto, Canada.

* Corresponding author
Dr. William L. Stanford, Ph.D.
The Ottawa Hospital, 501 Smyth Rd, Box 511, CCW 5206c
Ottawa, ON K1H 8L6, Canada

One Sentence Summary: We performed a drug screen in 3D and discovered HDAC inhibitors exhibit therapeutic efficacy in models of the lung disease lymphangioleiomyomatosis.

ABSTRACT

Lymphangioleiomyomatosis (LAM) is a rare disease involving cystic lung destruction by invasive LAM cells. These cells harbor loss-of-function mutations in *TSC2*, conferring constitutive mTORC1 signalling. Rapamycin is the only clinically approved disease-modifying treatment, but its action is cytostatic and disease progresses upon its withdrawal. There is a critical need to identify novel agents that prevent the invasive phenotype and/or eradicate the neoplastic LAM cells. Here, we employed novel cellular and extracellular models to screen for candidate therapeutics in a physiologically relevant setting. We observed that lung-mimetic hydrogel culture of pluripotent stem cell-derived diseased cells more faithfully recapitulates human LAM biology compared to conventional culture on two-dimensional tissue culture plastic. Leveraging our culture system, we conducted a three-dimensional drug screen using a custom 800-compound library, tracking cytotoxicity and invasion modulation phenotypes at the single cell level. We identified histone deacetylase (HDAC) inhibitors as a group of anti-invasive agents that are also selectively cytotoxic towards *TSC2*$^{-/-}$ cells. Unexpectedly, we observed that next generation ATP-competitive mTORC1/2 inhibitors potentiate invasion. We determined anti-invasive effects of HDAC inhibitors to be independent of genotype, while selective cell death is mTORC1-dependent and mediated by apoptosis. Drug performance was subsequently evaluated at the single cell level in zebrafish xenografts. We observed consistent therapeutic efficacy *in vivo* at equivalent concentrations to those used *in vitro,* substantiating HDAC inhibitors as potential therapeutic candidates for pursuit in patients with LAM.

INTRODUCTION

Lymphangioleiomyomatosis (LAM) is a cystic lung disease predominately affecting women, at a prevalence of 1 to 10 per million *(1)*. LAM can occur sporadically or in association with the multisystem tumor-forming disorder, Tuberous Sclerosis Complex (TSC) *(2)*. The pulmonary histopathology is characterized by microscopic nodules consisting of immature smooth muscle-like cells that express markers of neural crest lineages *(3)*. These invading cells digest the lung parenchyma forming cystic lesions that lead to progressive respiratory decline and fatality if untreated *(4–6)*. The molecular etiology of LAM involves loss-of-function mutations in the endogenous mTORC1 suppressor *TSC2*, thereby inducing hyperactivation of mTORC1 anabolic and tumorigenic signalling *(7)*. The allosteric mTORC1-inhibitor rapamycin (clinically, sirolimus) slows disease progression and improves symptomatology *(8–11)*. While clinical approval of rapamycin by the FDA in 2015 has led to a dramatic new frontier in the LAM therapeutic landscape, significant limitations exist. A subset of patients do not respond to treatment, and rapamycin is invariably cytostatic, with rapid disease progression upon treatment withdrawal *(11, 12)*. There is a critical need to discover novel treatment strategies that can eradicate LAM cells.

A key step in the pathway to therapeutic development is the effective modelling of disease characteristics. In this domain, LAM has remained a challenge. Cultures of cells derived from human pulmonary LAM lesions grow as a heterogeneous mixture with rapid exhaustion of *TSC2*$^{-/-}$ cells, prohibiting the establishment of clonal primary cell lines *(13)*. While a genome engineering strategy would seem straightforward for this monogenic disease, the cell-of-origin of LAM remains unknown, begging the question of which cell type to engineer. While we have demonstrated that *TSC2*$^{-/-}$ human pluripotent stem cell-derived neural crest cells model several

phenotypic features of LAM *(14)*, neural crest cells consist of a diverse and plastic population that are not readily scalable for drug screening purposes. Animal models of LAM have been comparably challenging to establish, and none to date have recapitulated pathognomonic features such as histological premelanosome protein (PMEL) positivity and concomitant elevated serum levels of vascular endothelial growth factor D (VEGF-D) *(15)*.

An emerging consideration in disease modelling is the contribution of the extracellular matrix (ECM) to disease biology. Water-swollen networks of polymers termed hydrogels have arisen as effective tools for mimicking salient elements of the native ECM while exhibiting mechanics similar to many soft tissues *(16)*. Hydrogels can be broadly classified as either natural, synthetic, or hybrid materials. One such hybrid scaffold is hyaluronic acid, a naturally-sourced material that can be readily modified to independently tune ECM features of interest, such as elasticity, stiffness, and viscosity *(17)*. A viscoelastic hydrogel with a derivatized hyaluronic acid backbone has been shown to permit the study of invasive properties of LAM cellular models in three-dimensional culture *(18)*. Importantly, three-dimensional culture systems have been demonstrated as more predictive of *in vivo* drug responses compared to conventional culture on two-dimensional plastic *(19, 20)*.

In recent years, there has been a resurgence of interest in phenotype-based screens for drug discovery compared to target-based approaches *(21)*. An analysis of therapeutics approved between 1999 and 2008 revealed that 62% first-in-class drugs were discovered by phenotype-based screens, despite the fact that such screens represented only a small subset of the overall total *(22)*. The apparent superiority of phenotype-based approaches may in part arise from the ability to identify compounds which exhibit a therapeutic effect by modulating multiple targets simultaneously *(21)*. In addition, phenotypic drug screens can be multiplexed with counter-

screening, ensuring candidate therapeutics do not also confer undesirable side-effects, such as physiological toxicity. In the context of LAM, a monogenetic disease, this counter-screening takes shape by directly comparing *TSC2*$^{-/-}$ cells against matched wild type (WT) controls.

Here, we analyze a novel hydrogel culture system of pluripotent stem cell-derived models, and observe the cell type employed, genotype, and culture substrate all contribute to modelling features of LAM. We performed a three-dimensional drug screen, tracking cytotoxicity and invasion modulation phenotypes at the single cell level. We identified histone deacetylase (HDAC) inhibitors as anti-invasive and selectively cytotoxic towards *TSC2*$^{-/-}$ cells. Importantly, we observed consistent therapeutic efficacy upon xenotransplantation of human cell models into zebrafish larvae, highlighting HDAC inhibitors as potential therapeutic candidates for pursuit in patients.

RESULTS

Stem cell-derived models exhibit features of LAM, independent of genotype

As pulmonary LAM cells are not amenable to expansion upon lesion explant, *(13)* we established primary cell lines by *in vivo* differentiation of human pluripotent stem cells (hPSCs), as previously described *(23)*. Briefly, hPSCs were injected into NOD.Cg-*Prkdc*^{scid} *Il2rg*^{tm1Wjl}/SzJ (NSG) immunodeficient mice to form teratomas, which were explanted and expanded in smooth muscle-cell enriching conditions (Fig. S1A). We used a previously reported isogenic pair of female mCherry^{+} WT and genome-engineered *TSC2*$^{-/-}$ hPSCs *(14)*. Cell cultures exhibit a predominately spindle cell morphology and express α-smooth muscle actin (ACTA2) protein in all isolated cells (Fig. 1A, Fig. S1B). Further, immunofluorescence analysis identified a small fraction of PMEL^{+} cells (~0.13%), a hallmark marker of pulmonary LAM (Fig. 1A, Fig. S1C). The high fraction of ACTA2^{+} and low fraction of PMEL^{+} cells in culture is consistent with the relative abundance of these markers in heterogenous human LAM lesions *(3)*. Notably, the percentage of PMEL^{+} and ACTA2^{+} cells did not vary between WT and *TSC2*$^{-/-}$ (Fig. S1B-C). Secreted VEGF-D, a critical biochemical biomarker used in the diagnosis of LAM, was detected in the supernatant of both WT and *TSC2*$^{-/-}$ cultures and was insensitive to acute rapamycin treatment (Fig. 1B). Together, these data suggest the cell models employed exhibit features of LAM as a product of the cell type isolated, independent of genotype.

Three-dimensional hydrogel culture enables study of the LAM invasive phenotype at single cell resolution

We next sought to model the pulmonary invasive phenotype of LAM cells by adapting a lung-mimetic hydrogel culture system *(18)*. The hydrogel is synthesized by crosslinking

hyaluronic acid strands with matrix metalloprotease (MMP)-cleavable peptides, while embedding vitronectin peptides and methylcellulose to increase cell adhesion and matrix plasticity, respectively. Cells are plated on top of the synthesized hydrogel and actively invade through the material (Fig. 1C-D, Supplementary Movies 1-2). By staining with a nuclear dye and acquiring multiplanar images through the optically clear hydrogel, we identify every cell in XYZ planes and compute invasion distances at single cell resolution (Fig. S1D).

We observed all cells from both WT and *TSC2*$^{-/-}$ cultures to invade through the hydrogel, albeit at variable distances (Fig. 1E). On average, WT cultures invaded further than *TSC2*$^{-/-}$ in a manner insensitive to acute rapamycin treatment (Fig. 1F). We posited that differing invasion distances of cells in the same culture reflect a cell autonomous property, rather than a reflection of stochasticity. To test this, we isolated and expanded clones from WT and *TSC2*$^{-/-}$ bulk cultures and subjected these clones to hydrogel culture. We observed a subset of clones with dramatically high invasion speeds, and likewise, a subset with slow invasion speeds (Fig. S1E). These data suggest differential cell autonomous capacities for invasion in putative heterogenous cultures. Finally, we investigated modes of invasion employed by LAM cell models in this hydrogel system. Similar to previous findings *(18)*, we observed a decrease in invasion upon treatment with the pan-MMP inhibitor GM6001 or the Rho-kinase (ROCK) inhibitor Y27632, indicating both protease-dependent and independent modes of invasion employed (Fig. 1G).

Loss of *TSC2* and hydrogel culture both confer transcriptomic features of LAM

To profile our cell culture system more comprehensively, we conducted bulk RNA-seq of WT and *TSC2*$^{-/-}$ cells, in the presence or absence of rapamycin, and in both plastic and hydrogel culture, for a total of 8 sample conditions (Fig. 1H). Principal components analysis (PCA)

revealed sample genotype to be driving the primary axis of variation, and culture substrate to be driving the secondary axis of variation (Fig. 1I). Rapamycin treatment induced a substantial global transcriptomic change in the *TSC2*$^{-/-}$ cells, inducing a profile more similar to WT cells (Fig. 1I).

We conducted differential expression analysis comparing across genotype (*TSC2*$^{-/-}$ vs. WT) and culture substrate (hydrogel vs. plastic) in untreated samples, while holding the reciprocal covariate constant. At a false discovery rate (FDR) < 0.05, we identified 6,317 differentially expressed genes (DEGs, 1,793 with $|\log_2 FC| > 1$) between WT and *TSC2*$^{-/-}$, and 4,432 DEGs (771 with $|\log_2 FC| > 1$) between plastic and hydrogel (Table S1A-B, Fig. S1F-G). While exhibiting some overlap, these DEG lists were largely distinct (Fig. S1H). We found 78.8% of the DEGs distinguishing genotype to be reversed by rapamycin treatment, suggesting mTORC1-dependency (Fig. 1J, left panel). In contrast, the expression of DEGs distinguishing plastic versus hydrogel cultures remained largely unchanged in the presence of rapamycin (Fig. 1J, right panel). We next examined the overlap of these DEGs with a recently published LAM gene signature derived from single cell RNA-seq profiling of primary lesions *(24)*. We observed that both DEG lists overlap substantially (65.8% of the total 760 LAM genes) and share both common and distinct genes with the LAM gene signature (Fig. 1K).

To glean further biological insight, we conducted GO term enrichment (Table S2A-B, Fig. S1I-J). Both DEG lists ranked “extracellular matrix organization” as most highly enriched, which is also the top enriched term in a primary LAM lesion gene signature list *(24)*. The DEGs distinguishing genotype were also enriched in many terms related to development, similar to primary LAM lesions *(24)*. Interestingly, the DEGs distinguishing culture substrates were largely enriched in terms related to proliferation (Table S1B, Fig. S1J). LAM is an indolent disease

which progresses at a slow pace relative to other invasive diseases; only a small fraction of cells actively proliferative in primary LAM lesions *(3)*. On plastic, we found LAM cell models proliferated rapidly, with ~30% of cells incorporating EdU after a short 3-hour pulse (Fig. 1L). In contrast, *TSC2*$^{-/-}$ cells proliferated at a slightly slower pace, consistent with previous studies of loss of *TSC2* in primary cells *(25)*. Acute rapamycin treatment reduced proliferation of *TSC2*$^{-/-}$ cells but did not have a detectable effect on WT cultures. However, subjecting cells to hydrogel culture caused a dramatic decrease in cell proliferation (Fig. 1L), likely reflective of the proliferation-invasion dichotomy *(26)*. Together, these data suggest both genotype (loss of *TSC2*) and culture substrate (3D hydrogel) induce transcriptomic landscapes which model LAM features.

Hydrogel culture potentiates differential mTORC1-signalling between WT and *TSC2*$^{-/-}$ cells

mTORC1 hyperactivation is a hallmark feature of primary LAM lesions compared to normal adjacent WT tissue. To assess mTORC1 signalling status, we performed a low input western blot, probing for downstream mTORC1 effectors pS6RP and p4E-BP1. Culturing cells on plastic (2D) showed marginal differences in mTORC1 signalling between WT and *TSC2*$^{-/-}$ cells, and both cell types demonstrated activation of mTORC1 above rapamycin-treated levels (Fig. 2A). Remarkably, culturing on hydrogel potentiated a dramatic difference in mTORC1 signalling, with WT cells downregulating activity to rapamycin-treated levels and *TSC2*$^{-/-}$ cells upregulating signalling above levels seen on plastic alone. This is consistent with the PCA of transcriptomic landscapes, whereby WT untreated and WT rapamycin-treated samples from hydrogel culture cluster slightly more closely compared to plastic culture (Fig. 1I). To corroborate these findings at the single cell level, we examined mTORC1 signalling by

immunofluorescence (Fig. 2B, S2A). While a small difference in mTORC1 signalling was observed between WT and *TSC2*$^{-/-}$ cells cultured on plastic, this difference was potentiated in 3D hydrogel culture. Importantly, mTORC1 signalling in WT cells was seen to mirror rapamycin-treated levels only when cultured on hydrogel.

We sought to further explore the genotype-selective changes induced by hydrogel culture by interrogation of our bulk RNA-seq dataset. To do so, we tested for genes with a significant coefficient fit to the genotype:substrate interaction term (See Supplementary Materials and Methods) and identified 761 DEGs at FDR < 0.05 (Table S1C). Network analysis of GO terms enriched in this DEG list revealed two principal nodes, one related to sterol synthesis and the other to ribonucleotide metabolism (Fig. 2C, Table S2C). Notably, both these metabolic pathways have been associated with mTORC1 activity *(27)*.

To unearth mTORC1-dependent transcriptomic alterations between WT and *TSC2*$^{-/-}$ that differ between plastic and hydrogel culture, we clustered the 761 DEGs based on their expression pattern across the 8 experimental conditions (Fig. S2B). Strikingly, genes related to sterol synthesis and ribonucleotide metabolism partitioned largely into two distinct clusters (Fig. S2B). We next classified each gene cluster into one of three categories based on the magnitude of expression differences between WT and *TSC2*$^{-/-}$, and whether the expression changes were rescued by rapamycin (Fig. S2C). Remarkably, we find that 69% of the 761 DEGs showed a greater (or a unique) difference between WT and *TSC2*$^{-/-}$ cells in hydrogel culture compared to plastic, which was rescued by rapamycin (Fig. 2D). Together, these results demonstrate that hydrogel culture potentiates differential mTORC1 signalling between WT and *TSC2*$^{-/-}$ cells, reinforcing a physiologically relevant environment in which mTORC1-dependent phenotypes can be identified.

Three-dimensional drug screen identifies compounds that modulate invasion and cell viability

We next employed our hydrogel culture system to identify potential therapeutic compounds. Cell death was measured at the single cell level by application of the live cell imaging fluorophore SyTOX, which selectively permeates cells with compromised plasma membrane integrity. We first tested a known cytotoxic compound, the proteasome inhibitor carfilzomib, and identified substantial cell death by live cell imaging (Fig. 3A, S3A). Additionally, we confirmed the ability to detect invasion modulation effects at the single cell level by employing the known anti-invasion Src kinase inhibitor dasatinib (Fig. 3B, S3B). To achieve the throughput necessary for a therapeutic screen, we acquired live cell images by high content microscopy paired with automated image analysis tools developed in house. We calculated the drug screen Z' (a metric for assay quality) to be 0.873 for cytotoxicity measurements and 0.533 for invasion modulation. We subsequently screened a curated library of 800 structurally diverse, bioactive, membrane-penetrant compounds (Fig. 3C, Table S3A). Of these compounds, 39% have been trialed and shown to be safe for use in humans. We tested each compound on both WT and *TSC2*$^{-/-}$ cells in the presence and absence of rapamycin to elucidate mTORC1-dependency.

We found a wide variety of compounds with invasion modulatory and cytotoxic capabilities (Table S3B-C). Unsurprisingly, highly cytotoxic compounds also led to a reduction in bulk invasion (Fig. 3D). This trend was independent of genotype and rapamycin treatment (Fig. S3C). However, we observed many compounds which conferred an anti-invasive effect in the absence of detectable cytotoxicity (Fig. 3D, S3C). We next computed therapeutic invasion z-

scores (i.e., statistical measure of compound effect size) by comparing against the vehicle control invasion distribution. Remarkably, while we identified several anti-invasive compounds, numerous compounds significantly increased invasion (Fig. 3E-F), a phenotype that would be otherwise overlooked if screening on two-dimensional plastic and could lead to severe adverse consequences in the clinical setting. In general, more compounds in this library were identified to significantly attenuate rather than potentiate invasion (Fig. 3F). Importantly, we observed a substantial overlap in the compounds identified to be anti-invasive across genotypes and treatment conditions, with very few drugs demonstrating a genotype-selective block to invasion (Fig. 3G, S3D). Together, these data demonstrate the identification of a collection of compounds which block invasion in these cell populations, irrespective of *TSC2* genotype.

A key goal in the therapeutic development landscape for LAM is the identification of compounds which exert selective cytotoxicity towards *TSC2*$^{-/-}$ cells. Interestingly, we observed that *TSC2*$^{-/-}$ cells exhibited pan-compound resistance, with over 7-fold more compounds demonstrating significant cytotoxicity towards WT compared to *TSC2*$^{-/-}$ cells (Fig. 3H). This selectivity is reduced to half with the addition of rapamycin, suggesting generalized resistance is largely due to mTORC1 hyperactivation in *TSC2*$^{-/-}$ cells. (Fig. 3H). We compared the list of compounds that are selectively cytotoxic towards *TSC2*$^{-/-}$ cells in the presence versus absence of rapamycin, and observed only a 15% overlap, indicating therapeutic vulnerabilities vary depending on mTORC1 signalling activity (Fig. 3I). In summary, we identified a suite of anti-invasive and selectively cytotoxic therapeutics which can be mined for further development in LAM (Table S3B-C).

Enrichment analysis predicts HDAC inhibitors as anti-invasive and selectively cytotoxic towards *TSC2*$^{-/-}$ cells

To refine our small molecule list for further investigation, we sought to identify outperforming compounds which modulate targets of the same class. Using the known annotated targets of the employed compounds, we performed target enrichment analysis by adapting the Gene Set Enrichment Analysis (GSEA) algorithm. We identified targets conferring well-established selective cytotoxicity towards *TSC2*$^{-/-}$ and anti-invasive classes, including proteasome inhibition (cytotoxicity) and Src and Rho kinase inhibition (anti-invasive) (Fig. S3E-F, Table S4A-D). Of note, Src inhibition, a therapeutic route explored in LAM, was found to be selectively cytotoxic towards WT cells (Fig. S3E). Remarkably, pan-HDAC inhibition was observed to be the only class in the top 10 most significant annotations for selective cytotoxicity towards *TSC2*$^{-/-}$ and generalized anti-invasion. We note a substantial favourable enrichment of HDAC-targeting compounds by both metrics, however, not all compounds annotated to inhibit HDACs performed favourably (Fig 3J).

A limiting factor to our analyses was the small number of compounds which were identified to selectively eliminate *TSC2*$^{-/-}$ cells. We sought to extend our compound list *in silico* using a structure-based approach with a mechanism of action prediction algorithm (Elion^{TM}). In brief, chemical features are extracted from compound structures and matched with screen performance values to train a machine learning algorithm for prediction of other possibly efficacious compounds. Compounds predicted to be efficacious *in silico* are then analyzed by target enrichment and pathway analysis. Using this approach, we corroborated HDACs as highly enriched targets for both selective cytotoxicity and anti-invasion (Table S5A-B). GO term analysis on significant targets identifies nearly all top predicted pathways relate to deacetylation

activity, for both selective cytotoxicity and anti-invasion (Fig. 3K, Table S5C-D). These data together highlighted HDAC inhibitors as promising therapeutics which we explored further and present herein.

HDAC inhibitors are selectively cytotoxic towards *TSC2*$^{-/-}$ cells exclusively in hydrogel culture

We further tested 11 HDAC inhibitors from our compound library at a wider range of concentrations and identified three to be selectively cytotoxic towards *TSC2*$^{-/-}$ cells: SAHA (clinically, Vorinostat), SB939 (Pracinostat), and LBH589 (Panobinostat), all of which are pan-HDAC inhibitors (Fig. 4A). We note the atypical therapeutic dose-response curves and selectivity, demonstrating marginal differences in IC_{50} *per se* but substantial variation in maximal toxicity (Fig. 4B). Selective cytotoxicity was largely reversed by co-treatment with rapamycin, suggesting mTORC1-dependency. Importantly, the magnitude of cytotoxic selectivity between WT and *TSC2*$^{-/-}$ cells increased with treatment duration (Fig. S4A). We corroborated selective cell death functionally via clonogenic assays (Fig. S4B). Remarkably, when these HDAC inhibitors were tested with cells cultured on plastic, we did not observe any genotype-selectivity in their cytotoxic profile (Fig. 4A-B). In addition, inhibitor profiles employed in plastic culture did not change in the presence of rapamycin, suggesting a loss of mTORC1-dependency for cytotoxic effects (Fig. 4A-B). While HDAC inhibitors did modulate the proliferation of cells in hydrogel culture, a substantial proliferation blockade was exerted when cells were cultured on plastic, in both genotypes (Fig. S4C). Together, these data indicate a striking difference in cellular responses to HDAC inhibitor treatment while cultured on plastic versus hydrogel. Importantly, HDAC inhibitors only demonstrate mTORC1-dependent selective

toxicity towards *TSC2*$^{-/-}$ cells while treated in hydrogel culture. These data are consistent with observation of hydrogel culture potentiating differential mTORC1 signalling between WT and *TSC2*$^{-/-}$ cells (Fig. 2, S2).

HDAC inhibitors induce cell death via apoptosis

We next sought to probe the mode of cell death induced by HDAC inhibitors. Previous studies have provided evidence for both HDAC inhibitor-mediated apoptosis as well as autophagic cell death *(28)*. Considering we observed a reduction in cell death when co-treated with rapamycin, a potent inducer of autophagy, we hypothesized the predominant cell death mode to be apoptosis. To test this postulation, we employed live cell apoptosis imaging reagents, including cleaved caspase 3 (CASP3) and Annexin V. We validated their activity in our hydrogel culture using staurosporine, a known inducer of apoptosis (Fig. S4D-E). For all three HDAC inhibitors, we observed temporal accumulation of Annexin V and cleaved CASP3 with treatment duration in hydrogel (Fig. 4C-D, S4F). Importantly, we discerned a complete rescue of cell death by co-treatment with the caspase inhibitor Z-VAD (OMe)-FMK (Fig. 4E, S4G). Together, these data demonstrate the employed HDAC inhibitors induce apoptotic cell death in hydrogel culture.

HDAC inhibitors are anti-invasive, independent of cytotoxic effects

To separate the anti-invasive effects from cytotoxic effects of these HDAC inhibitors, we identified and computationally removed SyTOX^{+} cells from invasion calculations (Fig. S5A). We determined all three HDAC inhibitors exhibited a dose-dependent anti-invasion effect on SyTOX^{-} cells (Fig. 5A-B). HDAC inhibitors exerted anti-invasive effects on both WT and *TSC2*$^{-/-}$ cells in the presence or absence of rapamycin. (Fig 5A-B, S5B-C). Of note, the effect size was

generally larger in the *TSC2*$^{-/-}$ cells, and LBH589 demonstrated a trend towards reduced invasion that was not statistically significant. Remarkably, of the 11 HDAC inhibitors we tested, eight demonstrated anti-invasive effects in a dose-dependent manner (Fig. S5D). When aggregated as a class of therapeutics, there is a clear increase in anti-invasive effects with escalating doses, independent of cytotoxicity (Fig. 5C). Together, these data demonstrate HDAC inhibitors are effective anti-invasive agents independent of their cytotoxic profile.

ATP-competitive mTORC1/2 inhibitors potentiate cell invasion

A surprising result of our 3D drug screen is the classification of ATP-competitive mTORC1/2 inhibitors as invasion potentiators (Fig. S3F). We interrogated this further due to its clinical relevance, as ATP-competitive inhibitors are in active development for a wide range of hyperactive mTOR conditions *(29)*. Across a five-point dose-response curve, we observed an increase in invasion from three distinct mTORC1/2 inhibitors, independent of cytotoxic effects (Fig. 5D-E). Invasion potentiation was observed in both WT and *TSC2*$^{-/-}$ cells in the presence or absence of rapamycin (Fig. 5D-E, S5E-F). The extent of invasion potentiation varied across conditions: WT cells exhibited a greater increase in invasion compared to *TSC2*$^{-/-}$, and the effect was exaggerated in both genotypes by co-treatment with rapamycin (Fig. S5G). Aggregating the effects of all three mTOR inhibitors showed a dose-dependent potentiation of invasion for this class of compounds (Fig. 5F). Together, these data demonstrate ATP-competitive inhibition of mTORC1/2 increases cell invasion.

Xenotransplantation of LAM cell models into zebrafish larvae permits dynamic tracking of cell invasion

We next sought to evaluate the *in vivo* efficacy of the HDAC inhibitors SAHA, SB939, and LBH589. Consistent with previous findings, we found that loss of *TSC2* alone was insufficient to confer tumorigenicity upon subcutaneous xenotransplantation in immunodeficient mice (Fig. S6A). To avoid immortalization of our cell models- a process which dramatically alters cellular characteristics- we performed a well-established xenotransplantation assay in zebrafish larvae *(31, 32)*. In this system, WT or *TSC2*$^{-/-}$ cells are injected into the hindbrain ventricle of zebrafish larvae 3 days post-fertilization, imaged 1 day post-injection (dpi) to ensure successful engraftment, and then imaged again at 4 dpi to visualize local invasion (Fig. 6A-B). Cells were tracked by their endogenous mCherry expression *(14)*. The optical clarity of this system provides the advantage of enabling isogenic comparisons between WT and *TSC2*$^{-/-}$ human cells *in vivo* while dynamically tracking cell invasion.

To quantify invasion in an unbiased fashion, we computed the ratio of mCherry signal found outside the injection site compared to within (Fig. S6B-C). Using this method, we accurately detect near zero invasion scores 1 dpi, followed by a substantial increase 4 dpi (Fig. 6C). We observed comparable invasion scores between WT and *TSC2*$^{-/-}$ cells which were unaffected by rapamycin treatment, consistent with *in vitro* data (Fig. 6D). To quantify human cell proliferation and cell death, we digested and pooled whole larvae (15 - 20 per condition) followed by flow cytometry analysis, probing for mCherry and human-specific CASP3. Consistent with xenotransplantation in mice, these cells were not tumorigenic and the rate of clearance outstripped proliferation (Fig. S6D). The number of cells at 4 dpi was comparable between genotypes and unaffected by rapamycin treatment (Fig. 6E). The percentage of CASP3^{+} cells in the mCherry^{+} population was ~10% and equivalent across conditions, similar to baseline cell death rates seen in hydrogel culture (Fig. 3A, 6F).

HDAC inhibitors SAHA and SB939 block cell invasion and selectively eradicate *TSC2*$^{-/-}$ cells in vivo

We next employed our zebrafish xenograft system to assess the efficacy of HDAC inhibitors *in vivo*. To achieve the highest quality of pre-clinical evidence, experiments were conducted in a randomized, double-blinded, placebo-controlled fashion. We first established dose-toxicity profiles for each HDAC inhibitor: SB939 and LBH589 conferred an IC_{50} of 53.1 μM and 6.74 μM respectively, while the favourable toxicity profile of SAHA precluded calculation of an IC_{50} value (Fig. S6E). Of note, *in vivo* HDAC inhibitor potency correlated with the *in vitro* cytotoxicity profile. Zebrafish engrafted with either WT or *TSC2*$^{-/-}$ cells were treated with HDAC inhibitors by immersion therapy, in the presence or absence of rapamycin. Importantly, we used the same compound concentration as those employed *in vitro*, which was well below each compound's IC_{50} value.

After three days of treatment, we observed that SAHA and SB939 exerted a statistically significant anti-invasive effect in the absence of rapamycin, exclusively on the *TSC2*$^{-/-}$ cells (Fig. 6G). SB939 also demonstrated a statistically significant anti-invasive effect in the presence of rapamycin. We note that live cells could not be distinguished from dead or dying cells in this quantification. However, by flow cytometry we observed an increase in the percentage of human *TSC2*$^{-/-}$ cells to be CASP3^{+} upon treatment with SAHA and SB939 (Fig. 6H) This effect was abrogated upon combination treatment with rapamycin and was not observed in the human WT cells. Together, these data indicate the HDAC inhibitors SAHA and SB939 exhibit *in vivo* anti-invasion and selective cytotoxicity effects towards *TSC2*$^{-/-}$ cells.

DISCUSSION

Here, we subject novel tissue-engineered models of LAM to a three-dimensional drug screen to detect physiologically relevant therapeutics. We identified HDAC inhibitors as anti-invasive and selectively cytotoxic towards *TSC2*$^{-/-}$ cells, both *in vitro* and *in vivo*. In contrast, the gold standard therapeutic agent for LAM patients, rapamycin, did not exhibit any cytotoxic or anti-invasive effects. To our knowledge, this is the first high content compound screen to simultaneously track invasion modulation and cytotoxicity at the single cell level. Importantly, we report the first zebrafish xenotransplantation system using LAM-like cells, extending parametrization of therapeutic effects at the single cell level *in vivo* while comparing WT versus *TSC2*$^{-/-}$ cells.

Our research identifies pan-HDAC inhibitors as potential therapeutic candidates for pursuit in LAM patients. Notably, the selective cytotoxic effect towards *TSC2*$^{-/-}$ cells was only observed in hydrogel culture and would have otherwise been missed using standard screening in 2D tissue culture plastic (Fig. 4A-B). This finding complements a recent study evidencing therapeutic efficacy of HDAC inhibitors in a *Tsc1*$^{-/-}$-driven mouse model of lymphangiosarcoma *(33)*. HDAC inhibitors present an opportune class of molecules for pursuit due to the wide variety of compounds already approved for clinical use. Indeed, both SAHA and LBH589 are approved for use in cutaneous T cell lymphoma and multiple myeloma, respectively *(34, 35)*. The safe-in-human toxicity profile of these compounds will facilitate rapid translation for testing in LAM patients. Importantly, our employed HDAC inhibitors exhibit selective cytotoxicity in an mTORC1-dependent manner, suggesting generalizable efficacy to mTORC1-driven malignancies. Of note, cutaneous T cell lymphoma cells have been observed to exhibit mTORC1 hyperactivation compared to matched normal controls *(36)*.

In this work, we used equivalent HDAC inhibitor concentrations for *in vitro* and *in vivo* experiments; these concentrations were well-below dose-limiting toxicities in zebrafish (Fig. S6E). However, a critical outstanding question is whether the concentrations employed are physiologically attainable in humans. Pharmacokinetic studies of SAHA, SB939, and LBH589 in humans have demonstrated micromolar serum concentrations are achievable *(37–39)*. In fact, the original pre-clinical work which formed the foundation for testing SAHA as a treatment in cutaneous T cell lymphoma used the drug *in vitro* at micromolar concentrations *(40)*. Thus, we anticipate drug concentrations necessary to elicit a therapeutic effect are achievable in patients with LAM. We note that while LBH589 demonstrated a therapeutic effect *in vitro*, drug efficacy was not maintained upon *in vivo* testing, possibly due to altered bioavailability in the zebrafish. While SAHA and SB939 demonstrated *in vivo* efficacy, the majority of parameters assessed demonstrated mTORC1-dependency, similar to *in vitro*. Many LAM patients are on a chronic regime of rapamycin; thus, it is likely that clinical trials would require short-term withdrawal of rapamycin and acute treatment with HDAC inhibitors to elicit a therapeutic effect. Alternatively, these therapeutics may provide a benefit for LAM patients who are not currently treated with rapamycin, whether due to mild disease, intolerance, or resistance.

Our three-dimensional screening approach permitted the identification of many compounds with invasion modulatory capabilities. We encourage further mining of these data to uncover additional novel classes of therapeutics which modulate invasion and/or exert selectivity cytotoxic effects (Table S3B-C). As one example, we identified ATP-competitive inhibitors of mTOR to increase cellular invasion (Fig. 5D-F, S5E-G). This is of clinical significance and requires further investigation, considering this class of therapeutics is undergoing investigation in a broad range of oncogenic conditions *(29)*.

Throughout our study, we note both genotype (loss of *TSC2*) and culture substrate (3D hydrogel) contribute to modelling features of LAM. Importantly, hydrogel culture potentiated differential mTORC1-signalling between WT and *TSC2*$^{-/-}$ cells, reinforcing a physiologically relevant environment in which mTORC1-dependent phenotypes can be identified (Fig 2, S2). However, we also note a variety of LAM features in our cellular models that exist independently from loss of *TSC2*. For example, cells isolated from both WT and *TSC2*$^{-/-}$ teratomas are equally invasive, present matching ACTA2^{+}/PMEL^{+} profiles, and secrete similar levels of VEGF-D. Indeed, similar observations of LAM features in WT cells have been noted in a neural crest cell model *(14)*. These data suggest perhaps, while loss of *TSC2* is critical for disease pathogenesis, the hallmark features of the putative "LAM cell" may already exist in a physiological, if not transient, context (e.g., during development, injury repair and inflammation). Critical consideration of the cell context is essential, even while employing isogenic comparisons, as different cell types exhibit distinct therapeutic vulnerabilities *(14)*.

In summary, we have identified HDAC inhibitors as anti-invasive and selectively cytotoxic towards *TSC2*$^{-/-}$ cells *in vitro* and *in vivo*. While we have investigated three pan-HDAC inhibitors as potential candidates, our data points towards SAHA as the most efficacious against *TSC2*$^{-/-}$ cells while possessing the most favourable toxicity profile. On the path towards clinical translation, we anticipate testing of these compounds in diverse disease models. By validating compounds with orthogonal tools and techniques, we may elevate the most promising therapeutic for clinical trials.

MATERIALS AND METHODS

Study design

The objective of this research was to assess the LAM disease modelling capabilities of newly developed tissue-engineered cell models, and subsequently employ these models to identify novel therapeutic compounds. We conducted a 3D drug screen, and based on the acquired data, formulated and tested the following hypothesis: HDAC inhibitors are anti-invasive and selectively cytotoxic towards *TSC2*$^{-/-}$ cells. We employed a combination of *in vitro* and *in vivo* tools to test this hypothesis. Drug screen data was analyzed in a blinded, unbiased manner, and independently by two different researchers using distinct methods. Animal studies were conducted and analyzed in a double-blinded, randomized, placebo-controlled manner to generate the highest quality pre-clinical evidence. Blinding was achieved by codification of an investigator uninvolved in the experiments performed. A variety of experimental tools were employed to interrogate this hypothesis, described in subsequent Methods and in the Supplementary Materials and Methods. All reagents used and concentrations employed (if relevant) are reported in Supplementary Materials and Methods.

Sample sizes for both *in vitro* and *in vivo* studies were determined according to field-specific conventions. Power analysis was not employed. Data collection was not stopped prematurely, and every experimental replicate was analyzed. All data points were included in the data presentation; outliers were only excluded if there was definitive empirical evidence of technical error and noted as such in the figure legend. Experiments were repeated at least three times unless otherwise noted, with replicates collected at separate points in time and under independent conditions. RNA-seq data is accessible at the Gene Expression Omnibus (GEO) repository with accession GSE179044.

Cell derivation and maintenance culture

LAM cell models were established via a previously reported *in vivo* differentiation protocol of human pluripotent stem cells *(23)*. Briefly, we injected hPSCs into NSG mice to form teratomas, which were then explanted and expanded in smooth muscle-cell enriching conditions (Fig. S1A). We used a previously reported pair of mCherry^{+} WT and genome-engineered *TSC2*$^{-/-}$ hPSCs for establishment of isogenic lines *(14)*. Maintenance cultures were propagated on plastic containing a thin layer of Matrigel at 37ºC, 5% CO_2. hPSCs were cultured in Essential 8 medium and passaged in clumps by EDTA incubation, followed by cell scraping and wide-pore pipette transfer. LAM cells were cultured on Matrigel in Medium 231 containing Smooth Muscle Growth Supplement and passaged by 0.05% Trypsin as single cell suspensions.

Hydrogel culture

Hydrogel culture was conducted according to a previously established protocol *(18)*. Briefly, a hyaluronic acid polymer backbone was derivatized with methylfuran motifs (confirmed by ^{1}H NMR) and conjugated to bismaleimide-terminated vitronectin and collagen-I-derived peptides, synthesized in house. Hydrogel viscoelasticity was increased by incorporation of methylcellulose derivatized with reactive thiol groups. Chemically synthesized hydrogel components were mixed and directly added to culture plates (384-well format) to gel at 37ºC for 3 hours. Following gelation, wells were hydrated with PBS and then subjected to three media washes interspaced with incubations at 37ºC for 45 mins. LAM cells were then dissociated, added to plates containing hydrogel, and centrifuged for 3 min. at 10*g* to achieve immediate contact with the hydrogel.

Cell treatments and live cell staining

All compound treatments were conducted for 72 hours unless otherwise stated. See Supplementary Materials and Methods for 3D screen design, implementation, and analysis. Live cell imaging dyes (Hoechst, SyTOX, Annexin V, Cleaved Caspase 3) were incubated for 30 min. prior to imaging. Dyes were added as 10X concentrates in PBS; Annexin V diluent also contained 2.5mM $CaCl_2$. To avoid cell detachment in the miniaturized well format, live imaging dyes were not washed prior to imaging; this did not impact image acquisition as dyes are minimally fluorescent unless bound to the target molecule.

Microscopy

We employed a high content imager (Thermo Fisher Scientific, Arrayscan VTI) to acquire multi-well and multi-planar images. Whole-well images (384-well plate format) of cells invading through hydrogel, stained with live cell dyes, were acquired by widefield microscopy with 40µm interval z-stacks. Unstained cells were imaged using a brightfield module. Tiled images of cells grown and stained on plastic were also acquired by high content widefield microscopy. Rodent subcutaneous xenografts were visualized by *in vivo* imaging (PerkinElmer, IVIS®). Zebrafish larvae xenografts were imaged by epifluorescence widefield microscopy (Zeiss, AxioObserver 7). Image analysis methods are reported in Supplementary Materials and Methods.

Animal studies

All animal experiments were conducted with approval from the University of Ottawa Animal Care Committee (Protocols #OHRI1666 and #CHEOe-3171), in accordance with the Canadian Council on Animal Care Standards and the Province of Ontario's Animals for Research Act. NSG mice (Jackson Laboratory) were maintained in sterile housing conditions and fed autoclaved chow and water ad libitum. Adult *casper (41)* zebrafish (a gift from Dr. Leonard Zon, Boston Children's Hospital, Boston, MA) were maintained in a recirculating commercial housing system (Aquatic Habitats, now Pentair) at 28°C in 14h:10h light:dark conditions in the aquatics facility at the University of Ottawa, Ottawa, ON. Adult *casper* zebrafish were bred according to standard protocol *(42)*, and embryos were collected and grown in E3 medium (5mM NaCl, 0.17mM KCl, 0.33mM $CaCl_2$, 0.33mM $MgSO_4$) at 28°C in 10cm Petri dishes until the desired time point. Embryos were cleaned and provided with new media every 24hrs. See Supplementary Materials and Methods for additional experimental details.

Statistical analysis

All figures are presented with individual data points (where graphically appropriate), with measures of central tendency and error to be mean and standard deviation, respectively, unless otherwise stated. Data pre-processing, statistical tests employed, sample number, and measured of central tendency and spread are reported in the figure legends. Two-sided tests were employed, and significance was attributed when $p < 0.05$. All analyses were of data from three independent experiments without removal of statistical outliers. Statistical tests employed were parametric except for analyses of zebrafish invasion data, where a non-normal distribution was observed. Calculation of drug screen statistics (e.g., z-scores, selectivity scores) are described in the Supplementary Materials and Methods.

LIST OF SUPPLEMENTARY MATERIALS

Table S2. GO term enrichment analysis of DEG lists.

Table S3. Three-dimensional drug screen raw data.

Table S4. Enrichment results via adaptation of GSEA.

Table S5. Elion^{TM} structure-based compound analysis.

Movie S1. Brightfield Z-stack of WT invading through the hydrogel, counterstained with Hoechst.

Movie S2. Brightfield Z-stack of *TSC2*$^{-/-}$ invading through the hydrogel, counterstained with Hoechst.

REFERENCES

1. A. M. Taveira-DaSilva, J. Moss, Clinical features, epidemiology, and therapy of lymphangioleiomyomatosis, *Clin Epidemiol* **7**, 249–257 (2015).

2. J. Moss, N. A. Avila, P. M. Barnes, R. A. Litzenberger, J. Bechtle, P. G. Brooks, C. J. Hedin, S. Hunsberger, A. S. Kristof, Prevalence and Clinical Characteristics of Lymphangioleiomyomatosis (LAM) in Patients with Tuberous Sclerosis Complex, *Am J Respir Crit Care Med* **164**, 669–671 (2001).

3. X. Zhe, L. Schuger, Combined Smooth Muscle and Melanocytic Differentiation in Lymphangioleiomyomatosis, *J Histochem Cytochem.* **52**, 1537–1542 (2004).

4. G. F. Abbott, M. L. Rosado-de-Christenson, A. A. Frazier, T. J. Franks, R. D. Pugatch, J. R. Galvin, From the archives of the AFIP: lymphangioleiomyomatosis: radiologic-pathologic correlation, *Radiographics* **25**, 803–828 (2005).

5. S. C. Chu, K. Horiba, J. Usuki, N. A. Avila, C. C. Chen, W. D. Travis, V. J. Ferrans, J. Moss, Comprehensive Evaluation of 35 Patients With Lymphangioleiomyomatosis, *Chest* **115**, 1041–1052 (1999).

6. T. Urban, R. Lazor, J. Lacronique, M. Murris, S. Labrune, D. Valeyre, J. F. Cordier, Pulmonary lymphangioleiomyomatosis. A study of 69 patients. Groupe d'Etudes et de Recherche sur les Maladies "Orphelines" Pulmonaires (GERM"O"P)., *Medicine (Baltimore)* **78**, 321–337 (1999).

7. E. P. Henske, F. X. McCormack, Lymphangioleiomyomatosis — a wolf in sheep's clothing, *J Clin Invest* **122**, 3807–3816 (2012).

8. A. M. Taveira-DaSilva, O. Hathaway, M. Stylianou, J. Moss, Changes in lung function and chylous effusions in patients with lymphangioleiomyomatosis treated with sirolimus, *Ann. Intern. Med.* **154**, 797–805, W-292–293 (2011).

9. J. Bee, S. Fuller, S. Miller, S. R. Johnson, Lung function response and side effects to rapamycin for lymphangioleiomyomatosis: a prospective national cohort study, *Thorax* **73**, 369–375 (2018).

10. J. Yao, A. M. Taveira-DaSilva, A. M. Jones, P. Julien-Williams, M. Stylianou, J. Moss, Sustained effects of sirolimus on lung function and cystic lung lesions in lymphangioleiomyomatosis, *Am. J. Respir. Crit. Care Med.* **190**, 1273–1282 (2014).

11. F. X. McCormack, Y. Inoue, J. Moss, L. G. Singer, C. Strange, K. Nakata, A. F. Barker, J. T. Chapman, M. L. Brantly, J. M. Stocks, K. K. Brown, J. P. I. Lynch, H. J. Goldberg, L. R. Young, B. W. Kinder, G. P. Downey, E. J. Sullivan, T. V. Colby, R. T. McKay, M. M. Cohen, L. Korbee, A. M. Taveira-DaSilva, H.-S. Lee, J. P. Krischer, B. C. Trapnell, Efficacy and Safety of Sirolimus in Lymphangioleiomyomatosis. *http://dx.doi.org/10.1056/NEJMoa1100391* (2011), doi:10.1056/NEJMoa1100391.

12. J. J. Bissler, F. X. McCormack, L. R. Young, J. M. Elwing, G. Chuck, J. M. Leonard, V. J. Schmithorst, T. Laor, A. S. Brody, J. Bean, S. Salisbury, D. N. Franz, Sirolimus for Angiomyolipoma in Tuberous Sclerosis Complex or Lymphangioleiomyomatosis, *N Engl J Med* **358**, 140–151 (2008).

13. E. A. Goncharova, D. A. Goncharov, A. Eszterhas, D. S. Hunter, M. K. Glassberg, R. S. Yeung, C. L. Walker, D. Noonan, D. J. Kwiatkowski, M. M. Chou, R. A. Panettieri, V. P. Krymskaya, Tuberin regulates p70 S6 kinase activation and ribosomal protein S6

phosphorylation. A role for the TSC2 tumor suppressor gene in pulmonary lymphangioleiomyomatosis (LAM), *J. Biol. Chem.* **277**, 30958–30967 (2002).

14. S. P. Delaney, L. M. Julian, A. Pietrobon, J. Yockell-Lelièvre, C. Doré, T. T. Wang, V. C. Doyon, A. Raymond, D. A. Patten, A. S. Kristof, M.-E. Harper, H. Sun, W. L. Stanford, Human pluripotent stem cell modeling of tuberous sclerosis complex reveals lineage-specific therapeutic vulnerabilities, *bioRxiv* , 683359 (2020).
15. D. J. Kwiatkowski, Animal Models of Lymphangioleiomyomatosis (LAM) and Tuberous Sclerosis Complex (TSC), *Lymphatic Research and Biology* **8**, 51–57 (2010).
16. S. R. Caliari, J. A. Burdick, A practical guide to hydrogels for cell culture, *Nature Methods* **13**, 405–414 (2016).
17. J. A. Burdick, G. D. Prestwich, Hyaluronic Acid Hydrogels for Biomedical Applications, *Advanced Materials* **23**, H41–H56 (2011).
18. R. Y. Tam, J. Yockell-Lelièvre, L. J. Smith, L. M. Julian, A. E. G. Baker, C. Choey, M. S. Hasim, J. Dimitroulakos, W. L. Stanford, M. S. Shoichet, Rationally Designed 3D Hydrogels Model Invasive Lung Diseases Enabling High-Content Drug Screening, *Advanced Materials* **31**, 1806214 (2019).
19. R. Edmondson, J. J. Broglie, A. F. Adcock, L. Yang, Three-dimensional cell culture systems and their applications in drug discovery and cell-based biosensors., *Assay Drug Dev Technol* **12**, 207–218 (2014).
20. A. E. G. Baker, L. C. Bahlmann, R. Y. Tam, J. C. Liu, A. N. Ganesh, N. Mitrousis, R. Marcellus, M. Spears, J. M. S. Bartlett, D. W. Cescon, G. D. Bader, M. S. Shoichet, Benchmarking to the Gold Standard: Hyaluronan-Oxime Hydrogels Recapitulate Xenograft

Models with In Vitro Breast Cancer Spheroid Culture, *Advanced Materials* **31**, 1901166 (2019).

21. C. A. MacRae, R. T. Peterson, Zebrafish as tools for drug discovery, *Nature Reviews Drug Discovery* **14**, 721–731 (2015).
22. D. C. Swinney, J. Anthony, How were new medicines discovered?, *Nature Reviews Drug Discovery* **10**, 507–519 (2011).
23. L. M. Julian, S. P. Delaney, Y. Wang, A. A. Goldberg, C. Doré, J. Yockell-Lelièvre, R. Y. Tam, K. Giannikou, F. McMurray, M. S. Shoichet, M.-E. Harper, E. P. Henske, D. J. Kwiatkowski, T. N. Darling, J. Moss, A. S. Kristof, W. L. Stanford, Human Pluripotent Stem Cell–Derived TSC2-Haploinsufficient Smooth Muscle Cells Recapitulate Features of Lymphangioleiomyomatosis, *Cancer Res* (2017), doi:10.1158/0008-5472.CAN-17-0925.
24. M. Guo, J. J. Yu, A. K. Perl, K. A. Wikenheiser-Brokamp, M. Riccetti, E. Y. Zhang, P. Sudha, M. Adam, A. Potter, E. J. Kopras, K. Giannikou, S. S. Potter, S. Sherman, S. R. Hammes, D. J. Kwiatkowski, J. A. Whitsett, F. X. McCormack, Y. Xu, Single Cell Transcriptomic Analysis Identifies a Unique Pulmonary Lymphangioleiomyomatosis Cell, *American Journal of Respiratory and Critical Care Medicine* (2020), doi:10.1164/rccm.201912-2445OC.
25. H. Zhang, G. Cicchetti, H. Onda, H. B. Koon, K. Asrican, N. Bajraszewski, F. Vazquez, C. L. Carpenter, D. J. Kwiatkowski, Loss of Tsc1/Tsc2 activates mTOR and disrupts PI3K-Akt signaling through downregulation of PDGFR, *J Clin Invest* **112**, 1223–1233 (2003).
26. A. Giese, M. A. Loo, N. Tran, D. Haskett, S. W. Coons, M. E. Berens, Dichotomy of astrocytoma migration and proliferation, *Int. J. Cancer* **67**, 275–282 (1996).

27. A. J. Valvezan, B. D. Manning, Molecular logic of mTORC1 signalling as a metabolic rheostat, *Nat Metab* **1**, 321–333 (2019).

28. D. S. Schrump, Cytotoxicity Mediated by Histone Deacetylase Inhibitors in Cancer Cells: Mechanisms and Potential Clinical Implications, *Clin Cancer Res* **15**, 3947–3957 (2009).

29. A. S. Alzahrani, PI3K/Akt/mTOR inhibitors in cancer: At the bench and bedside, *Seminars in Cancer Biology* **59**, 125–132 (2019).

30. A. L. Fridman, M. A. Tainsky, Critical pathways in cellular senescence and immortalization revealed by gene expression profiling, *Oncogene* **27**, 5975–5987 (2008).

31. B. Adane, G. Alexe, B. K. A. Seong, D. Lu, E. E. Hwang, D. Hnisz, C. A. Lareau, L. Ross, S. Lin, F. S. Dela Cruz, M. Richardson, A. S. Weintraub, S. Wang, A. B. Iniguez, N. V. Dharia, A. S. Conway, A. L. Robichaud, B. Tanenbaum, J. M. Krill-Burger, F. Vazquez, M. Schenone, J. N. Berman, A. L. Kung, S. A. Carr, M. J. Aryee, R. A. Young, B. D. Crompton, K. Stegmaier, STAG2 loss rewires oncogenic and developmental programs to promote metastasis in Ewing sarcoma, *Cancer Cell* **39**, 827-844.e10 (2021).

32. A. M. El-Naggar, C. J. Veinotte, H. Cheng, T. G. P. Grunewald, G. L. Negri, S. P. Somasekharan, D. P. Corkery, F. Tirode, J. Mathers, D. Khan, A. H. Kyle, J. H. Baker, N. E. LePard, S. McKinney, S. Hajee, M. Bosiljcic, G. Leprivier, C. E. Tognon, A. I. Minchinton, K. L. Bennewith, O. Delattre, Y. Wang, G. Dellaire, J. N. Berman, P. H. Sorensen, Translational Activation of HIF1α by YB-1 Promotes Sarcoma Metastasis, *Cancer Cell* **27**, 682–697 (2015).

33. F. Yang, S. Sun, C. Wang, M. Haas, S. Yeo, J.-L. Guan, Targeted therapy for mTORC1-driven tumours through HDAC inhibition by exploiting innate vulnerability of mTORC1 hyper-activation, *British Journal of Cancer* , 1–12 (2020).

34. B. S. Mann, J. R. Johnson, M. H. Cohen, R. Justice, R. Pazdur, FDA approval summary: vorinostat for treatment of advanced primary cutaneous T-cell lymphoma, *Oncologist* **12**, 1247–1252 (2007).

35. L. A. Raedler, Farydak (Panobinostat): First HDAC Inhibitor Approved for Patients with Relapsed Multiple Myeloma, *Am Health Drug Benefits* **9**, 84–87 (2016).

36. T. E. Witzig, C. Reeder, J. J. Han, B. LaPlant, M. Stenson, H. W. Tun, W. Macon, S. M. Ansell, T. M. Habermann, D. J. Inwards, I. N. Micallef, P. B. Johnston, L. F. Porrata, J. P. Colgan, S. Markovic, G. S. Nowakowski, M. Gupta, The mTORC1 inhibitor everolimus has antitumor activity in vitro and produces tumor responses in patients with relapsed T-cell lymphoma, *Blood* **126**, 328–335 (2015).

37. E. H. Rubin, N. G. B. Agrawal, E. J. Friedman, P. Scott, K. E. Mazina, L. Sun, L. Du, J. L. Ricker, S. R. Frankel, K. M. Gottesdiener, J. A. Wagner, M. Iwamoto, A Study to Determine the Effects of Food and Multiple Dosing on the Pharmacokinetics of Vorinostat Given Orally to Patients with Advanced Cancer, *Clin Cancer Res* **12**, 7039–7045 (2006).

38. F. Giles, T. Fischer, J. Cortes, G. Garcia-Manero, J. Beck, F. Ravandi, E. Masson, P. Rae, G. Laird, S. Sharma, H. Kantarjian, M. Dugan, M. Albitar, K. Bhalla, A Phase I Study of Intravenous LBH589, a Novel Cinnamic Hydroxamic Acid Analogue Histone Deacetylase Inhibitor, in Patients with Refractory Hematologic Malignancies, *Clin Cancer Res* **12**, 4628–4635 (2006).

39. W. P. Yong, B. C. Goh, R. A. Soo, H. C. Toh, K. Ethirajulu, J. Wood, V. Novotny-Diermayr, S. C. Lee, W. L. Yeo, D. Chan, D. Lim, E. Seah, R. Lim, J. Zhu, Phase I and pharmacodynamic study of an orally administered novel inhibitor of histone deacetylases, SB939, in patients with refractory solid malignancies, *Ann Oncol* **22**, 2516–2522 (2011).

40. C. Zhang, V. Richon, X. Ni, R. Talpur, M. Duvic, Selective Induction of Apoptosis by Histone Deacetylase Inhibitor SAHA in Cutaneous T-Cell Lymphoma Cells: Relevance to Mechanism of Therapeutic Action, *Journal of Investigative Dermatology* **125**, 1045–1052 (2005).

41. R. M. White, A. Sessa, C. Burke, T. Bowman, J. LeBlanc, C. Ceol, C. Bourque, M. Dovey, W. Goessling, C. E. Burns, L. I. Zon, Transparent Adult Zebrafish as a Tool for In Vivo Transplantation Analysis, *Cell Stem Cell* **2**, 183–189 (2008).

42. M. Westerfield, *THE Zebrafish Book a Guide for the Laboratory Use of Zebrafish Danio**.

43. A. Subramanian, P. Tamayo, V. K. Mootha, S. Mukherjee, B. L. Ebert, M. A. Gillette, A. Paulovich, S. L. Pomeroy, T. R. Golub, E. S. Lander, J. P. Mesirov, Gene set enrichment analysis: A knowledge-based approach for interpreting genome-wide expression profiles, *Proc. Natl. Acad. Sci.* **102**, 15545–15550 (2005).

44. D. P. Corkery, G. Dellaire, J. N. Berman, Leukaemia xenotransplantation in zebrafish – chemotherapy response assay in vivo, *Br. J. Haematol.* **153**, 786–789 (2011).

45. H. M, T. C, S. Wl, M. P, Human melanoma cells transplanted into zebrafish proliferate, migrate, produce melanin, form masses and stimulate angiogenesis in zebrafish., *Angiogenesis* **9**, 139–151 (2006).

ACKNOWLEDGEMENTS

We thank Catherine Lawrence for her inspiration, members of our labs for continued insights, the Ottawa Bioinformatics Core Facility (particularly Christopher Porter) for assistance in processing RNA-seq data, and the Human Pluripotent Stem Cell Core Facility and Rima Al-awar (Ontario Institute for Cancer Research) for the custom designed drug library.

Funding:

Canadian Institutes for Health Research (CIHR) grant FRN-153188 (WLS)

LAM Foundation pilot grant LAM0123P01-17 (WLS)

Funds from Green Eggs and LAM (WLS and MSS)

CIHR Vanier Canada Graduate Scholarship (AP)

CIHR Tier 1 Canada Research Chair Program in Integrative Stem Cell Biology (WLS)

Author contributions:

Conceptualization: AP, JYL, SPD, RYT, JNB, MSS, WLS

Methodology: AP, JYL, NM, LJS, NA, CX, NM, LMJ, RYT, MSS, WLS

Investigation: AP, JYL, NM, NA, NM, EL, AC, CD

Visualization: AP, JYL

Funding acquisition: MSS, WLS

Supervision: GM, LMJ, ASK, RYT, JNB, MSS, WLS

Writing – original draft: AP, WLS

Writing – review & editing: AP, JYL, NM, LJS, SPD, NA, CX, EL, AC, CD, GM, LMJ, ASK, RYT, JNB, MSS, WLS

Competing interests: Authors declare that they have no competing interests.

Data and materials availability: Processed data are available in the main text and the supplementary materials. Raw RNA-seq data is accessible at the GEO repository with accession GSE179044. Code written in house for data processing is available on request.

FIGURES

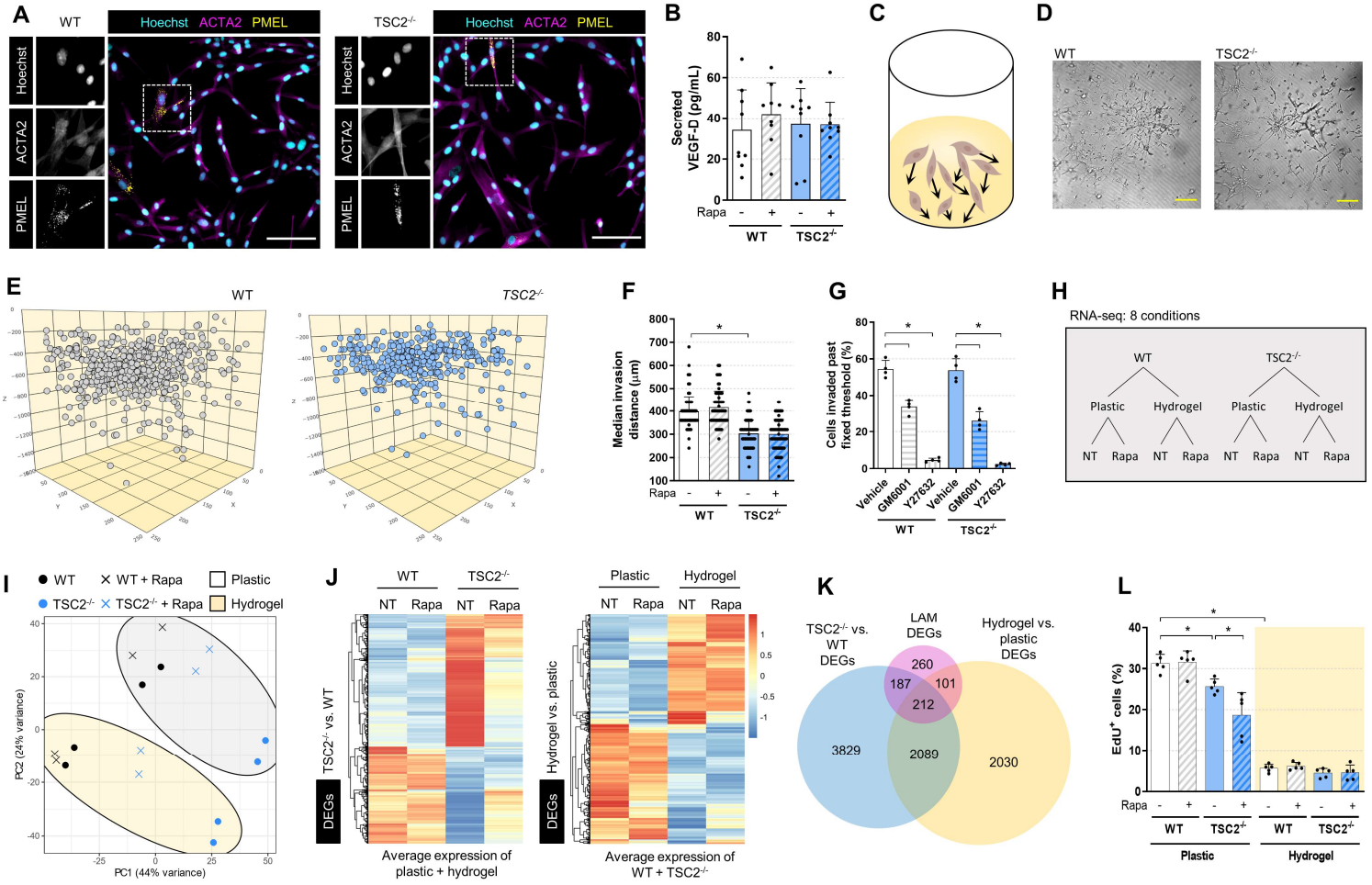

Fig. 1. Hydrogel culture of stem cell-derived disease models exhibits features of LAM. (**A**) Representative immunofluorescence images of *WT* and *TSC2*$^{-/-}$ cells. Inset showing punctate PMEL and fibril ACTA2 staining. Scale bars of 100μM. (**B**) VEGF-D secreted into conditioned media measured by ELISA, following 16hr incubation in serum-free media ± 20nM rapamycin (mean ± SD; * = $p < 0.05$ by Student t-test; n = 9-10). (**C-E**) Visualization of LAM cell invasion after three days in hydrogel culture, as (**C**) a schematic, (**D**) brightfield image of single Z plane, scale bars of 250μm, and (**E**) computational reconstruction of cellular spatial positions. (**F**) Median invasion distance of cellular populations plated on the hydrogel and cultured for three days ± 20nM rapamycin (mean ± SD; * = $p < 0.05$ by Student t-test; n = 124). (**G**) Percentage of

cells invaded past fixed threshold set by median invasion distance of genotype-matched vehicle control. Cells were cultured and treated for three days (10μM GM6001, a pan-MMP inhibitor, and 20μM Y27632, a ROCK inhibitor, mean ± SD; * = $p < 0.05$ by Student t-test; n = 4). (**H**) Schematic of the sample conditions tested in the bulk RNA-seq experiment. NT = no treatment, Rapa = rapamycin treatment (20nM, 72 hrs). (**I**) Principal components analysis (PCA) of bulk RNA-seq samples. (**J**) Heatmap and hierarchal clustering of differentially expressed genes (DEGs) between *TSC2*$^{-/-}$ and WT samples, and between hydrogel and plastic samples, while controlling for the reciprocal covariate. Left panel: transcript expression for plastic and hydrogel cultures were averaged. Right panel: transcript expression for WT and *TSC2*$^{-/-}$ samples were averaged. DEG analysis was performed with no treatment samples; genes noted as differentially expressed if FDR < 0.05 and $|\log_2 FC| > 1$. (**K**) Overlap in DEG between genotype and ECM gene lists and LAM cell signature gene list *(24)*. Genes noted as DE if FDR < 0.05. (**L**) Percentage of EdU^+ (proliferating) cells from 3-hour pulse (5μM), after three days cultured on plastic or hydrogel ± 20nM rapamycin (mean ± SD; * = $p < 0.05$ by Student t-test; n = 5).

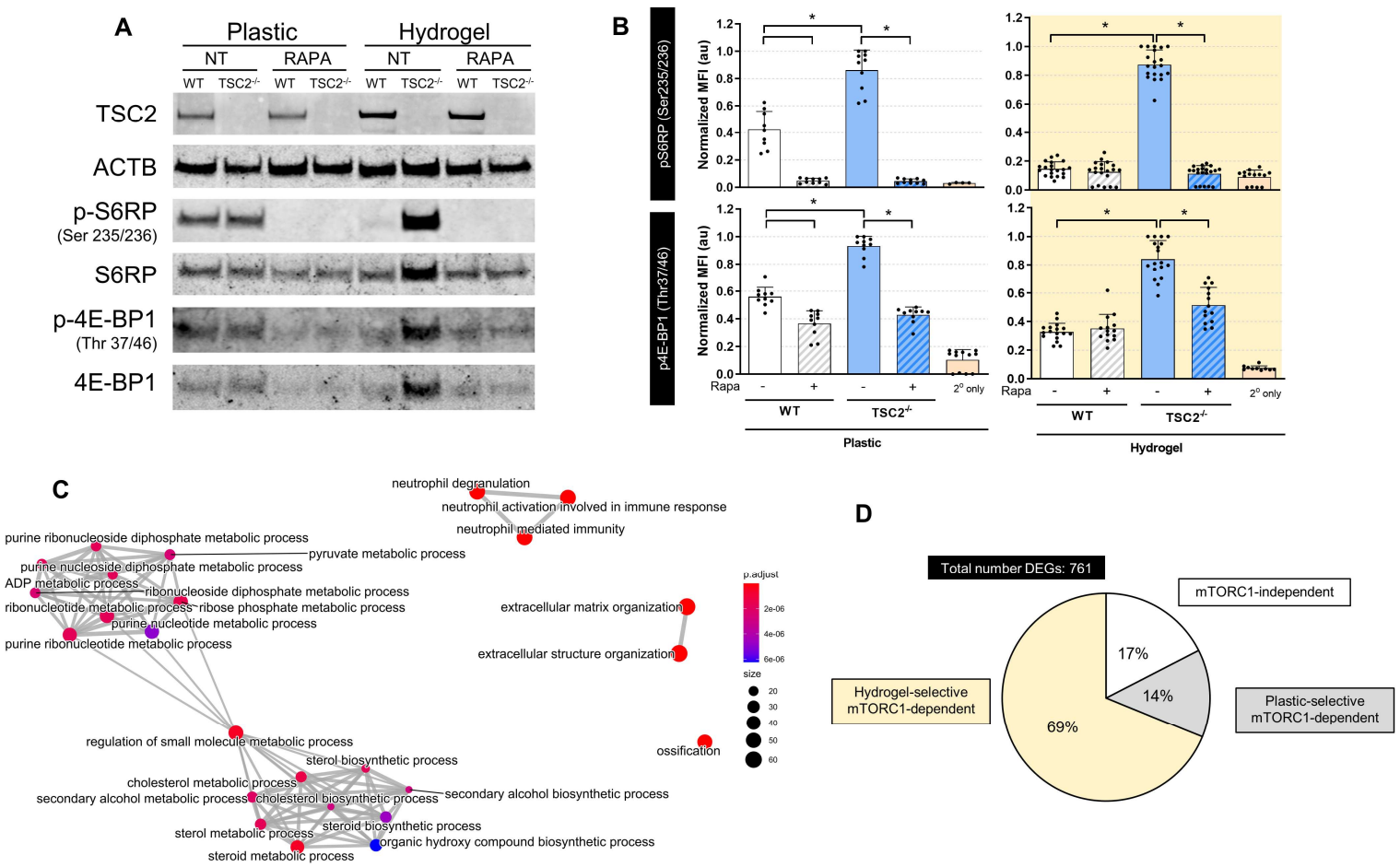

Fig. 2. Hydrogel culture potentiates differential mTORC1-signalling between WT and TSC2$^{-/-}$ cells. (**A**) Low input Western blot of protein collected from cells cultured for three days on plastic or hydrogel ± 20nM rapamycin. NT = no treatment, Rapa = rapamycin treatment. (**B**) Quantification of immunofluorescence values reported in normalized (scaled by replicate maximum value) mean fluorescence intensity. Each point indicates the mean fluorescence intensity from a well of cells cultured on hydrogel or plastic for three days ± 20nM rapamycin. Secondary only values are determined from wells probed with fluorescent secondary antibody only (mean ± SD; * = $p < 0.05$ by Student t-test; n = 9-20). (**C**) Network analysis of GO terms enriched in the list of DEGs found significant (FDR < 0.05) in the interaction between genotype and culture substrate. The 25 most significantly enriched terms are plotted. (**D**) Classification of

DEGs according to pattern of expression across genotypes, ECM condition, and in the presence or absence of rapamycin. Gene clusters and classification scheme shown in Fig. S2B-C).

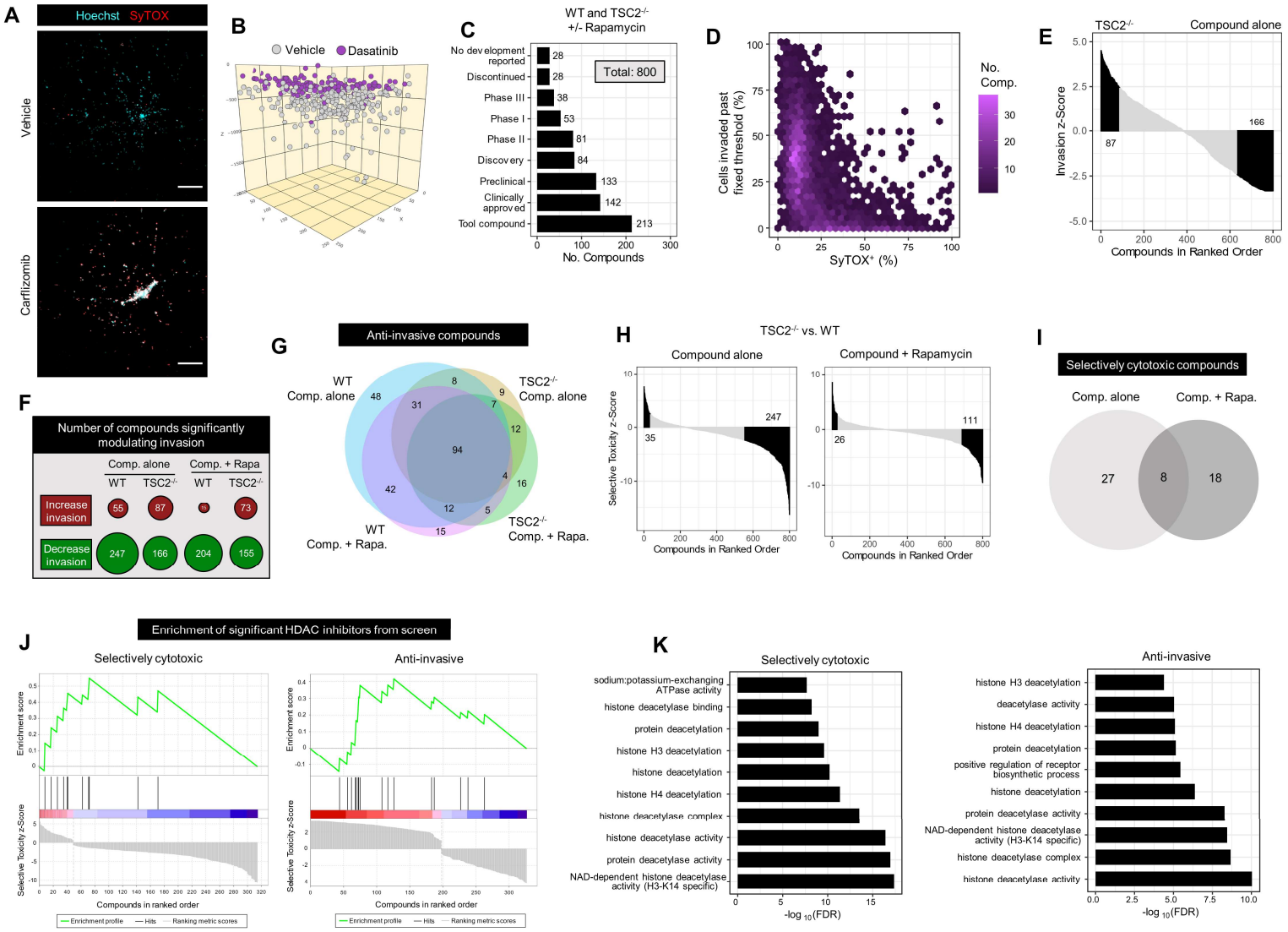

Fig. 3. Three-dimensional drug screen identifies HDAC inhibitors as anti-invasive and selectively cytotoxic towards TSC2$^{-/-}$ LAM cells. (**A**) Representative maximum intensity projection image of *TSC2*$^{-/-}$ cells in hydrogel culture for three days ± 200nM carfilzomib. Scale bars of 250µm. (**B**) Computational reconstruction of cellular spatial positions following three-day hydrogel culture of *TSC2*$^{-/-}$ cells ± 40nM dasatinib. Note that treated and untreated were in separate wells; cells were plotted in the same volume for ease of visualizing relative distances travelled. (**C**) Highest development status reported for the 800 compounds contained in the curated kinase inhibitor and tool compound libraries. A 3D drug screen was conducted on WT

and *TSC2*$^{-/-}$ cells following three-day treatment with 5μM compounds ± 20nM rapamycin. (**D**) Compound invasion modulation plotted against cytotoxicity, aggregating results across genotype and rapamycin treatment. Fixed invasion threshold determined by median invasion distance of untreated controls. Hexagonal plot employed to demonstrate compound densities. (**E**) Waterfall plot of compound invasion z-scores in ranked order; positive values indicate invasion potentiation, while negative values indicate invasion attenuation. Compounds conferring statistically significant invasion modulation highlighted in black. Data presented for *TSC2*$^{-/-}$, no rapamycin treatment condition. (**F**) Number of compounds significantly modulating invasion (potentiating or attenuating) for each genotype in the presence of absence of 20nM rapamycin. Bubble area proportional to number of statistically significant targets. (**G**) Overlap of compounds identified as anti-invasive in each listed condition. (**H**) Waterfall plots of compound selective toxicity z-scores in ranked order; positive values indicate increased cytotoxicity towards *TSC2*$^{-/-}$ cells, negative values indicate increased cytotoxicity towards WT cells. Compounds conferring statistically significant selective cytotoxicity highlighted in black. (**I**) Overlap of compounds identified to be selectivity cytotoxic towards *TSC2*$^{-/-}$ cells, with or without 20nM rapamycin. (**J**) Enrichment plot for compounds annotated to target HDACs, derived from an adapted implementation of GSEA. Hits (black vertical lines) in the red region indicate compounds with a favourable effect, hits in the blue region indicate compounds with an undesirable effect. (**K**) Top 10 most statistically significant GO terms. Analysis performed using targets identified as statistically significantly enriched in screen data by Elion^{TM} algorithm.

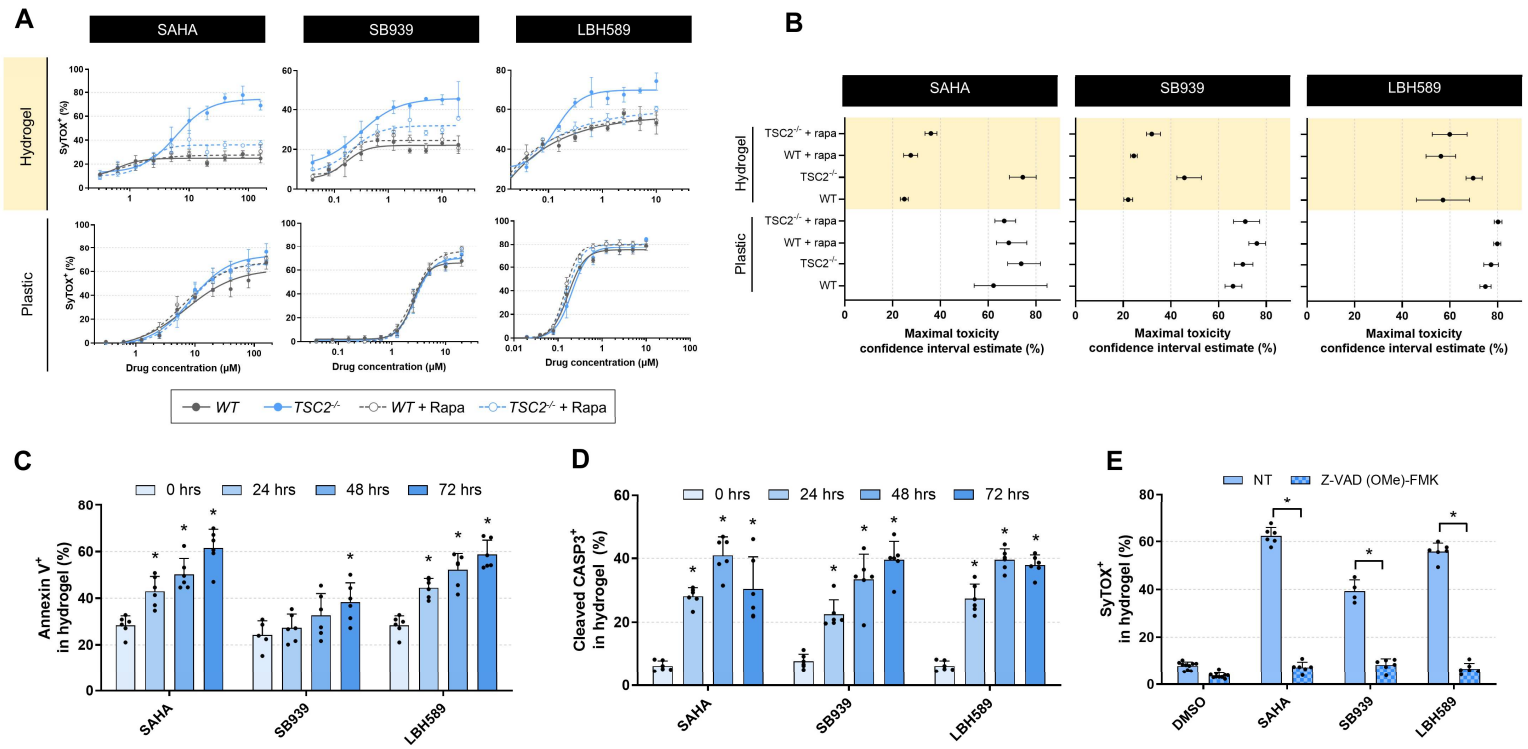

Fig. 4. Three safe-in-human HDAC inhibitors induce mTORC1-dependent selective cytotoxicity exclusively in hydrogel culture. (**A**) Dose-response cytotoxicity curves of cells treated with the indicated HDAC inhibitor for three days while cultured on plastic or hydrogel ± 20nM rapamycin. Data fit via four-parameter logistic regression (mean ± SD; n = 3). (**B**) Confidence intervals of HDAC inhibitor maximal toxicity, estimated by four-parameter logistic regression models generated in A. (**C-D**) Quantification of *TSC2*$^{-/-}$ cells positive for (**C**) Annexin V or (**D**) cleaved caspase 3, following three-day treatment with HDAC inhibitors in hydrogel (20μM SAHA, 5μM SB939, and 1μM LHB589, mean ± SD; * = $p < 0.05$ by ANOVA with Dunnett post-hoc comparison to 0 hrs; n = 6). (**E**) Quantification of *TSC2*$^{-/-}$ cells positive for SyTOX following three-day HDAC inhibitor treatment (20μM SAHA, 5μM SB939, and 1μM LHB589) in hydrogel ± 25μM Z-VAD (OMe)-FMK (mean ± SD; * = $p < 0.05$ by Student t-test; n = 4-6).

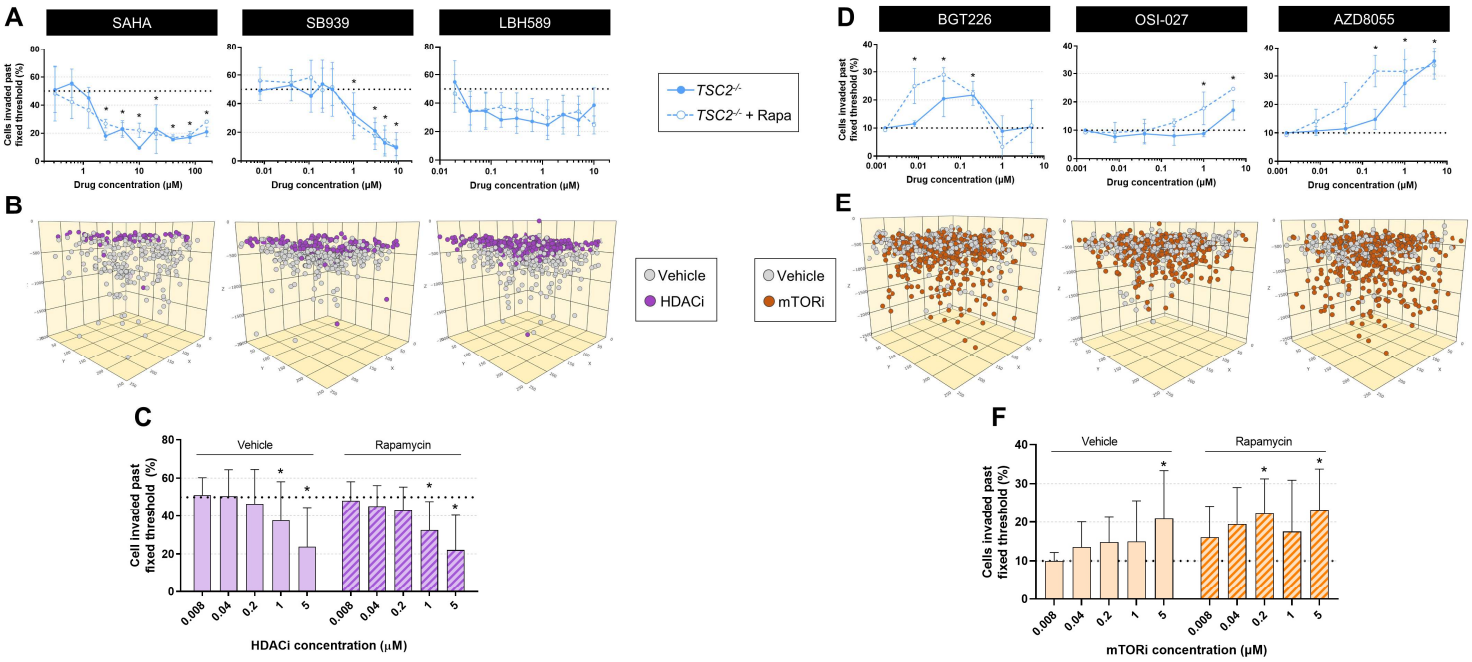

Fig. 5. HDAC inhibitors attenuate cell invasion independent of cytotoxicity while mTOR inhibitors potentiate the invasion phenotype. (**A**) Live *TSC2*$^{-/-}$ cells invaded past fixed threshold set by median invasion distance of vehicle control, upon three-day HDAC inhibitor treatment ± 20nM rapamycin (mean ± SD; * = $p < 0.05$ by ANOVA with Dunnett post-hoc comparison to untreated; n = 3). (**B**) Computational reconstruction of live cell spatial positions upon three-day hydrogel culture of *TSC2*$^{-/-}$ cells ± HDAC inhibitor (HDACi) treatment (5μM SAHA, 5μM SB939, 1μM LBH589). Note that treated and untreated cells were in separate wells; cells were plotted in the same volume for ease of visualizing relative distances travelled. (**C**) Aggregated effect of 11 HDAC inhibitors on *TSC2*$^{-/-}$ live cell invasion ± 20nM rapamycin. Fixed threshold set by median invasion distance of vehicle control (mean ± SD; * = $p < 0.05$ by ANOVA with Dunnett post-hoc comparison to untreated; n = 33 via 11 HDACi, n = 3 each). (**D**) Live *TSC2*$^{-/-}$ cells invaded past fixed threshold set by 90th percentile invasion distance of vehicle control, upon three-day mTOR inhibitor treatment ± 20nM rapamycin (mean ± SD; * = $p < 0.05$ by ANOVA with Dunnett post-hoc comparison to untreated; n =3). (**E**) Computational

reconstruction of live cell spatial positions upon three-day hydrogel culture of *TSC2*$^{-/-}$ ± mTOR inhibitor treatment (40nM BGT226, 5μM OSI-027, 5μM AZD8055). (**F**) Aggregated effect of 3 mTOR inhibitors (mTORi) on *TSC2*$^{-/-}$ live cell invasion ± 20nM rapamycin. Fixed threshold set by 90th percentile invasion distance of vehicle control (mean ± SD; * = $p < 0.05$ by ANOVA with Dunnett post-hoc comparison to untreated; n = 9 via 3 mTORi, n = 3 each).

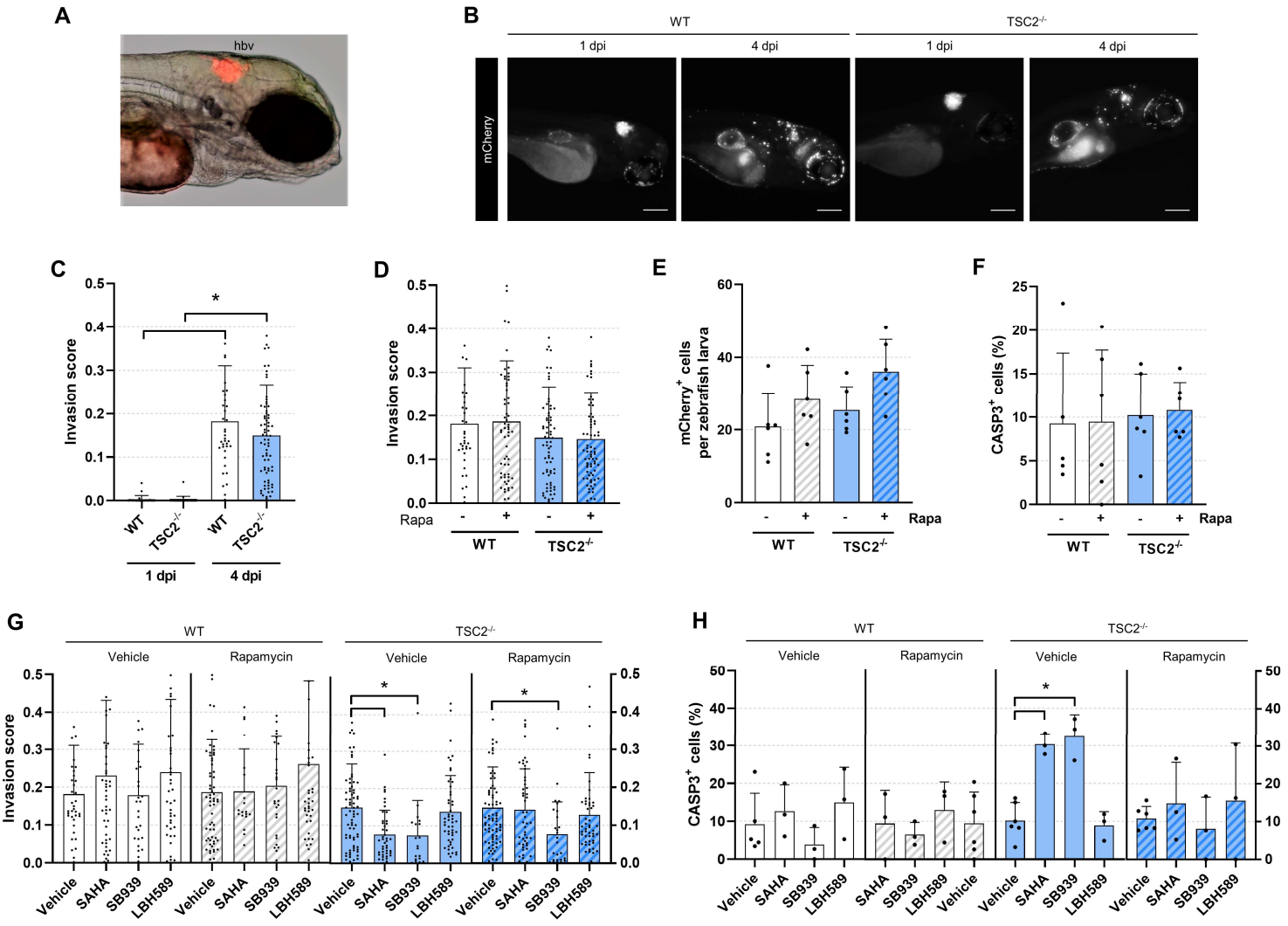

Fig. 6. HDAC inhibitors are anti-invasive and selectively cytotoxic towards TSC2$^{-/-}$ cells xenotransplanted into zebrafish. (**A**) Representative phase contrast image of 1 day post-injection (dpi) zebrafish larvae injected with *TSC2*$^{-/-}$ mCherry^{+} cells into the hindbrain ventricle (hbv). (**B**) Representative images of zebrafish larvae injected with mCherry^{+} WT or *TSC2*$^{-/-}$ cells into the hbv. Fish were imaged 1 and 4 dpi. Scale bars of 200µm. (**C-D**) Quantification of cell invasion using automated invasion analysis. Images analyzed in (D) were taken 4 dpi following three-day treatment ± 20nM rapamycin (mean ± SD; * = $p < 0.05$ by Mann–Whitney U test; n = 38 - 73). (**E**) Number of mCherry^{+} cells detected per zebrafish following whole larvae dissociation at 4 dpi and analysis by flow cytometry. Samples were treated for three days ±

20nM rapamycin. Each replicate is a pool of 15 – 20 zebrafish larvae (mean ± SD; * = $p < 0.05$ by Student t-test; n = 6). (**F**) Percentage of $CASP3^+$ cells in the $mCherry^+$ population from whole larvae dissociation at 4 dpi, following 3-day treatment ± 20nM rapamycin. Each replicate is a pool of 15 – 20 zebrafish larvae (mean ± SD; * = $p < 0.05$ by Student t-test; n = 5 – 6). (G-H) Effect of three-day HDAC inhibitor treatment (20μM SAHA, 5μM SB939, 1μM LBH589) ± 20nM rapamycin. (**G**) Invasion scores calculated on images acquired 4dpi (mean ± SD; * = $p < 0.05$ by the Kruskal-Wallis test with Dunn's post-hoc comparison to vehicle treated; n = 27 – 73). (**H**) Percentage of $CASP3^+$ cells in the $mCherry^+$ population from whole larvae dissociation at 4 dpi. Each replicate is a pool of 15 – 20 zebrafish larvae (mean ± SD; * = $p < 0.05$ by ANOVA with Dunnett post-hoc comparison to vehicle treated; n = 3 – 6). Not all outliers in (C-D) and (G) are visualized due to trimmed axes (although outliers were included in mean ± SD and the statistical calculation).

SUPPLEMENTARY FIGURES

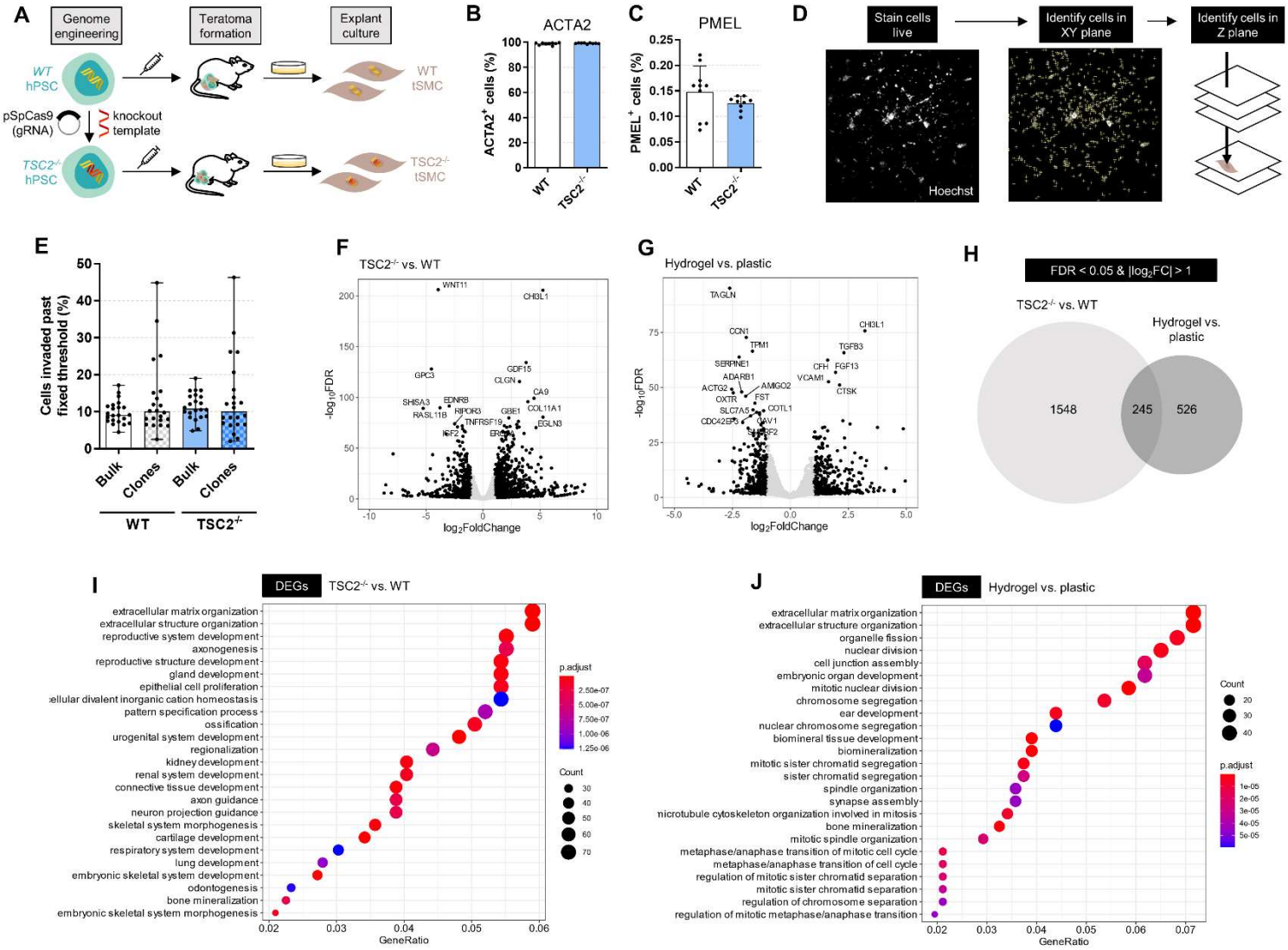

Fig. S1. Hydrogel culture of stem cell-derived disease models exhibits features of LAM. (A) Schematic of generation of LAM cellular models. (B-C) Quantification of LAM markers by flow cytometry from cells in maintenance culture (mean ± SD; * = $p < 0.05$ by Student t-test; n = 10). (D) Schematic of cell position identification in XYZ planes. (E) Percentage of cells invaded past threshold set by 90th percentile invasion distance of bulk cultures, following three-day hydrogel culture. Bulk cultures are maintenance cultures of LAM cell lines; clones are populations of cells expanded from a single cell isolated from maintenance cultures prior to seeding on hydrogel

(mean ± data range; no statistical test). (F-G) Volcano plot upon comparing *TSC2*$^{-/-}$ vs. WT cells (F) and hydrogel vs. plastic samples (G). Points highlighted in black are considered differentially expressed (FDR < 0.05 and $|\log_2 FC| > 1$). The 20 most significantly DEGs are noted. (H) Overlap in DEG between genotype and culture substrate gene lists; genes considered as DEGs if FDR < 0.05 and $|\log_2 FC| > 1$. (I-J) Dotplot of GO term enrichment analysis of DEG lists (FDR < 0.05 and $|\log_2 FC| > 1$) upon comparing *TSC2*$^{-/-}$ vs. WT cells (I) and hydrogel vs. plastic samples (J). The 25 most significantly enriched terms are plotted.

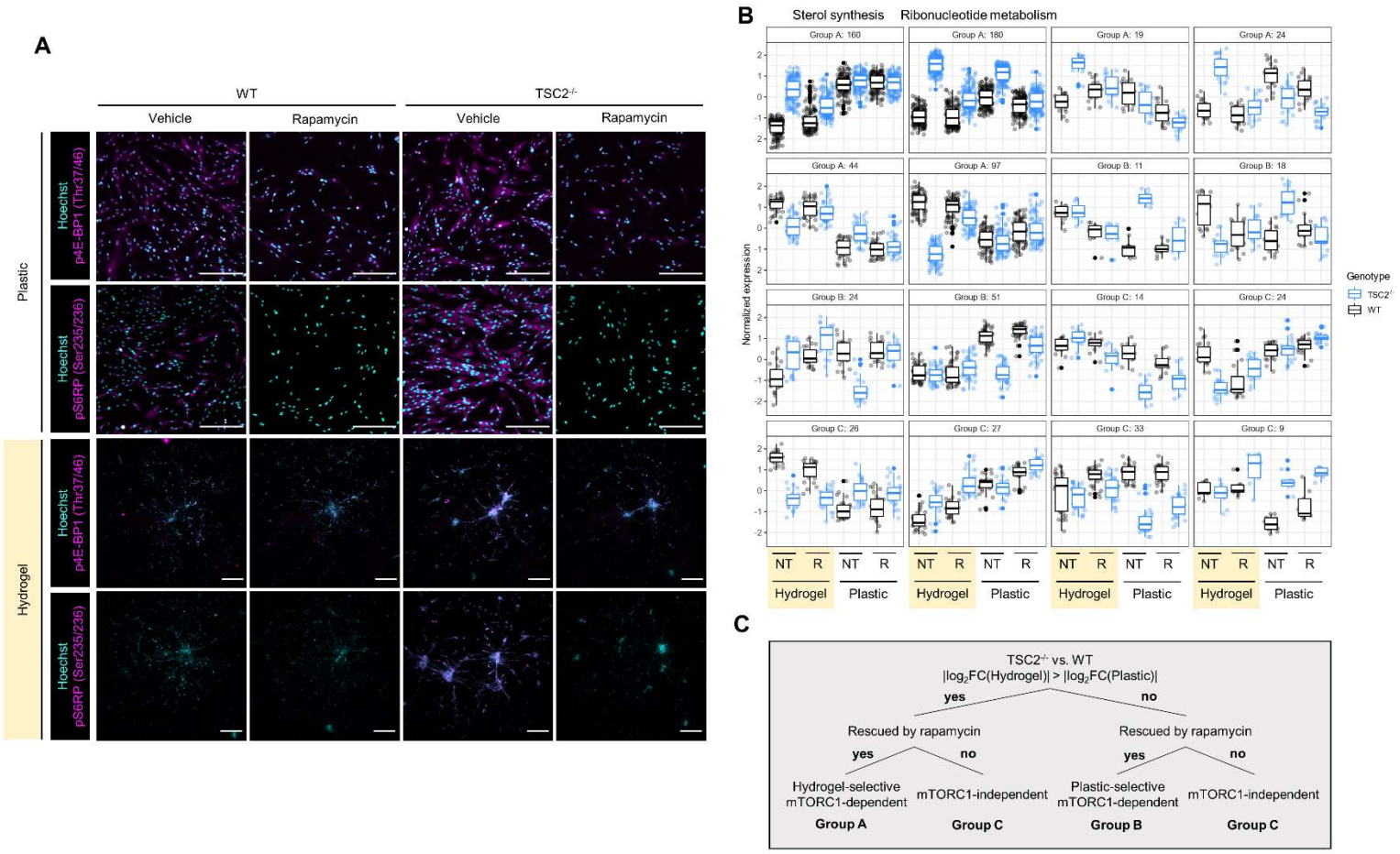

Fig. S2. Hydrogel culture potentiates differential mTORC1-signalling between WT and TSC2$^{-/-}$ cells. (A) Representative maximum intensity projection images used for quantification, following culture on hydrogel or plastic for three days ± 20nM rapamycin. Scale bars of 250µm. (B) Gene clusters following hierarchal clustering of DEGs found significant (FDR < 0.05) in the interaction between genotype and ECM (761 genes). Clustering was based on the pattern of gene expression across the 8 employed conditions. The first two clusters are annotated to be enriched in sterol synthesis and ribonucleotide metabolism terms. (C) Classification scheme applied to the gene clusters visualized in (B). Labelling of Groups A, B, and C is for ease of visualization in (B) and does not confer any specific biological meaning.

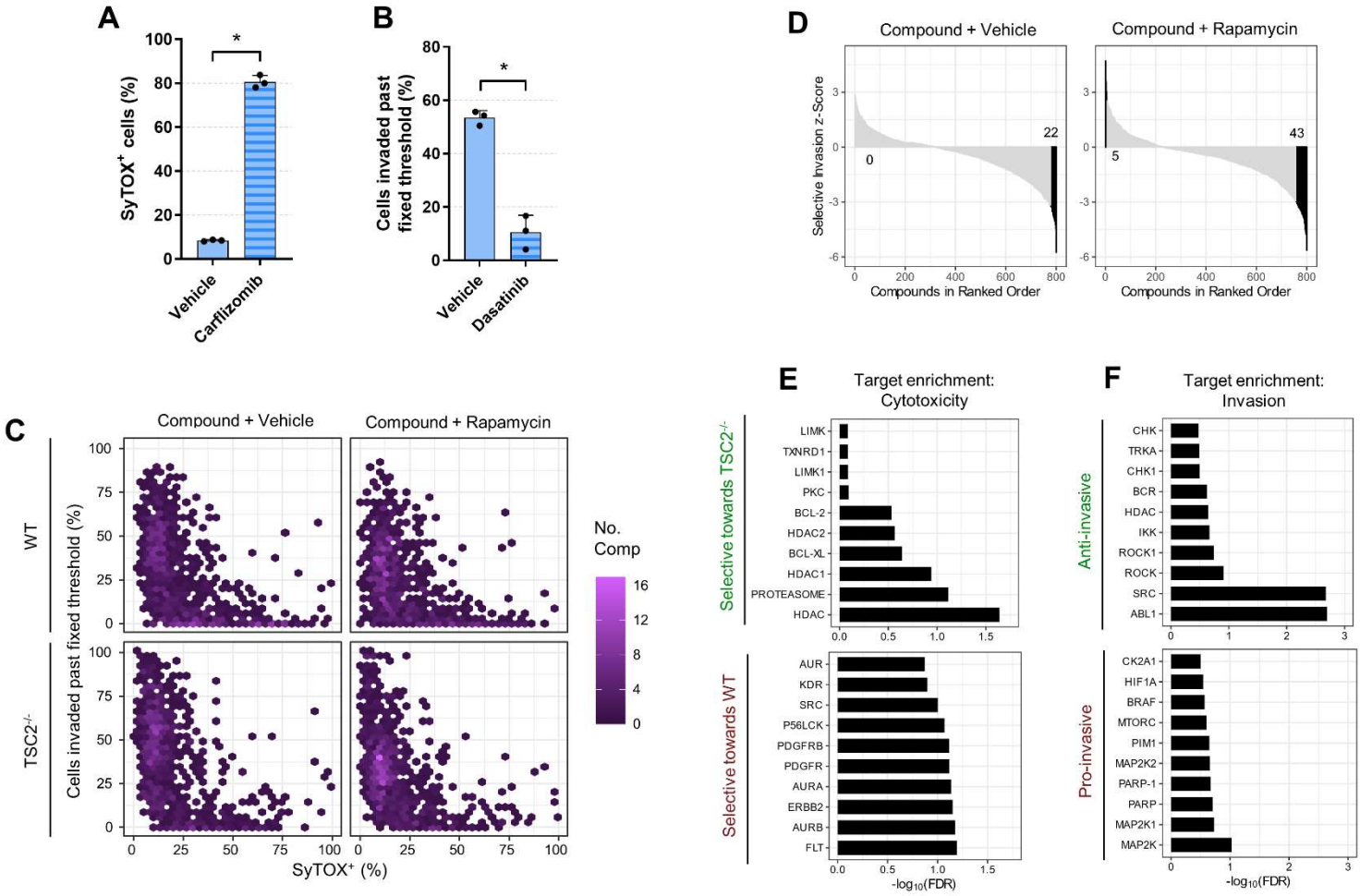

Fig. S3. Three-dimensional drug screen identifies HDAC inhibitors as anti-invasive and selectively cytotoxic towards TSC2$^{-/-}$ LAM cells. (A) Percentage of SyTOX^{+} *TSC2*$^{-/-}$ cells in hydrogel culture for three days ± 200nM carfilzomib (mean ± SD; * = $p < 0.05$ by Student t-test; n = 3). (B) Percentage of *TSC2*$^{-/-}$ cells invaded past fixed threshold (determined by median invasion distance of untreated controls), following three-day hydrogel culture ± 40nM dasatinib (mean ± SD; * = $p < 0.05$ by Student t-test; n = 3). (C) Compound invasion modulation plotted against cytotoxicity, separated by genotype and rapamycin treatment. Fixed threshold determined by median invasion distance of genotype-specific untreated controls. Hexagonal plot employed to demonstrate compound densities. (D) Waterfall plots of compound selective invasion z-scores in ranked order; positive values indicate greater anti-invasive effects towards *TSC2*$^{-/-}$, negative

values indicate greater anti-invasive effects towards WT. Compounds conferring statistically significant selective invasion modulation highlighted in black. (E-F) Top 10 most statistically significant targets enriched in screen data, stratified by screen parameter. Enrichment analysis was performed via adaptation of the GSEA algorithm, using annotated targets of the compound library.

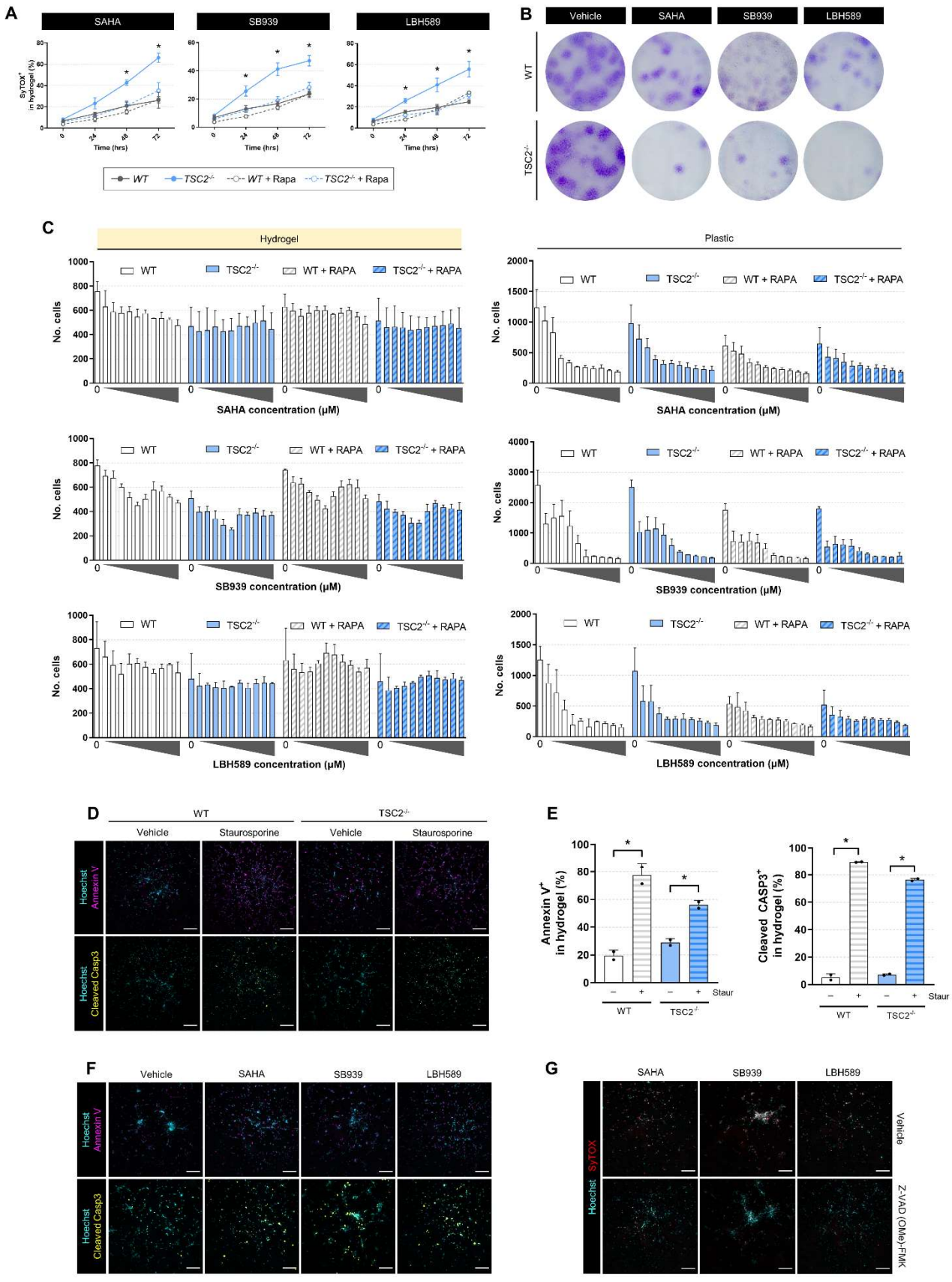
A
SAHA
SB939
LBH589
SyTOX+ in hydrogel (%)
Time (hrs)
WT
TSC2-/-
WT + Rapa
TSC2-/- + Rapa
B
Vehicle
SAHA
SB939
LBH589
WT
TSC2-/-
C
Hydrogel
Plastic
WT
TSC2-/-
WT + RAPA
TSC2-/- + RAPA
No. cells
SAHA concentration (μM)
SB939 concentration (μM)
LBH589 concentration (μM)
D
WT
TSC2-/-
Vehicle
Staurosporine
Hoechst
Annexin V
Cleaved Casp3
E
Annexin V+ in hydrogel (%)
Cleaved CASP3+ in hydrogel (%)
Staur
F
Vehicle
SAHA
SB939
LBH589
G
SyTOX
Z-VAD (OMe)-FMK

Fig. S4. Three safe-in-human HDAC inhibitors induce mTORC1-dependent selective cytotoxicity exclusively in hydrogel culture. (A) Percentage of $SyTOX^+$ cells following time-lapse HDAC inhibitor treatment (20μM SAHA, 5μM SB939, 1μM LBH589) of cells cultured in hydrogel ± 20nM rapamycin (mean ± SD; * = $p < 0.05$ by two-factor ANOVA with Tukey's post-hoc comparison; n = 3). (B) Clonogenic assay following three-day HDAC inhibitor treatment (20μM SAHA, 5μM SB939, 1μM LBH589) of cells cultured in hydrogel. After treatment, cells were extracted from hydrogel and replated in 2D to assess clonogenicity. (C) Number of cells detected in culture by high content imaging following three-day HDAC inhibitor treatment in hydrogel or plastic culture ± 20nM rapamycin. Inhibitor concentrations escalated in two-fold increments: SAHA (0.31μM min, 160μM max), SB939 (0.04μM min, 20μM max), and LBH589 (0.02μM min, 10μM max). Mean ± SD, n = 3. (D-E) Representative maximum intensity projection images and quantification of live cell imaging dyes used in hydrogel culture, following 4hr treatment of 1μM staurosporine (mean ± SD; * = $p < 0.05$ by Student t-test; n = 2). Scale bars of 250μm. (F-G) Representative maximum intensity projection images of live cell imaging dyes used in hydrogel culture, following three-day treatment with HDAC inhibitors (20μM SAHA, 5μM SB939, 1μM LBH589) ± 25μM Z-VAD (OMe)-FMK. Scale bars of 250μm.

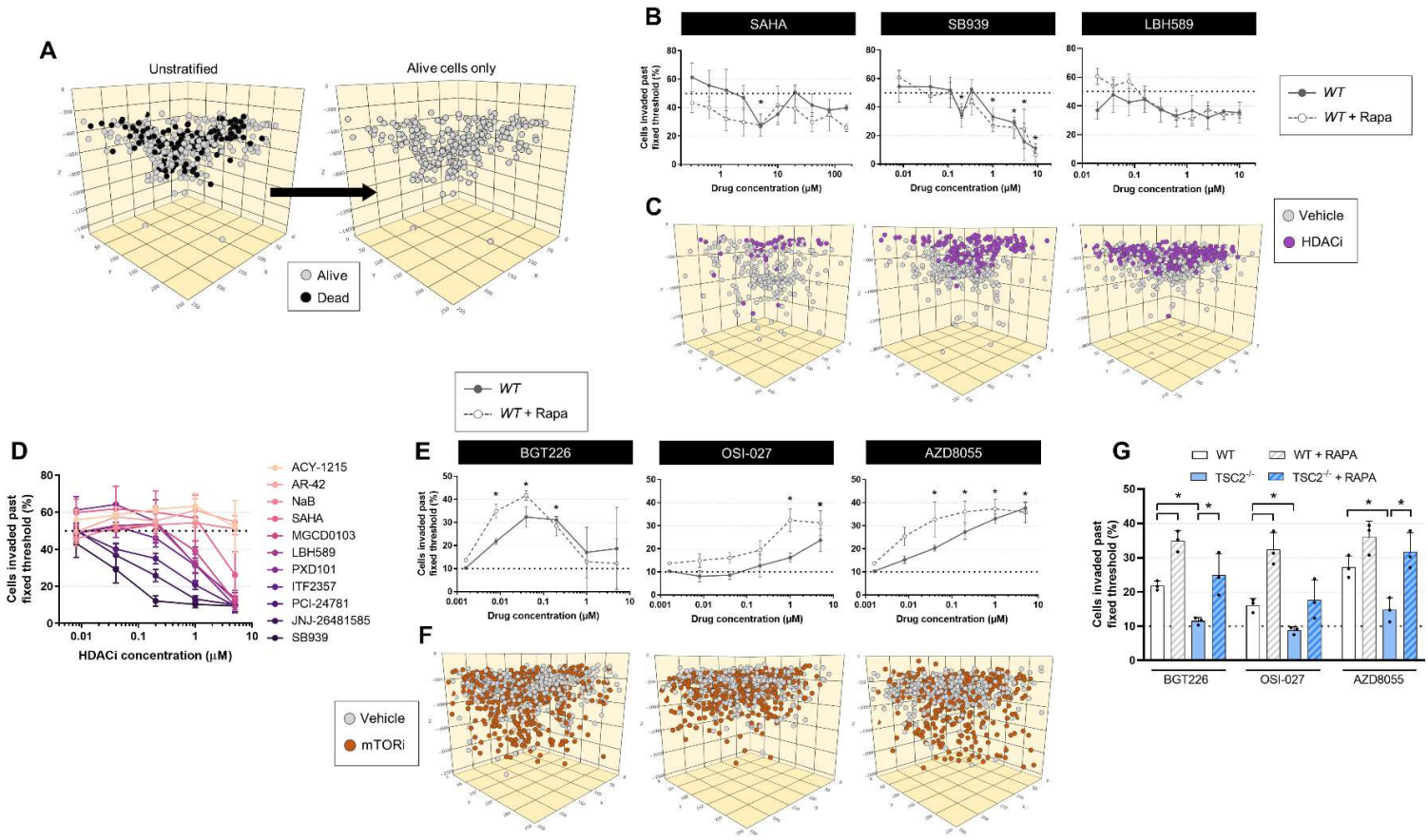

Fig. S5. HDAC inhibitors attenuate cell invasion independent of cytotoxicity while mTOR inhibitors potentiate the invasion phenotype. (A) Schematic for removal of SyTOX^{+} cells to determine invasion distribution of live cells. (B) Live WT cells invaded past fixed threshold set by median invasion distance of vehicle control, upon three-day HDAC inhibitor treatment ± 20nM rapamycin (mean ± SD; * = $p < 0.05$ by ANOVA with Dunnett post-hoc comparison to untreated; n = 3). (C) Computational reconstruction of live cell spatial positions upon three-day hydrogel culture of WT ± HDAC inhibitor treatment (5μM SAHA, 5μM SB939, 1μM LBH589). Note that treated and untreated were in separate wells; cells were plotted in the same volume for ease of visualizing relative distances travelled. (D) Effect of 11 HDAC inhibitors on *TSC2*$^{-/-}$ live cell invasion ± 20nM rapamycin. Fixed threshold set by median invasion distance of vehicle control. (E) Live WT cells invaded past fixed threshold set by 90th percentile invasion distance of

vehicle control, upon three-day mTOR inhibitor treatment ± 20nM rapamycin (mean ± SD; * = $p < 0.05$ by ANOVA with Dunnett post-hoc comparison to untreated; n = 3). (F) Computational reconstruction of live cell spatial positions upon three-day hydrogel culture of WT ± mTOR inhibitor treatment (40nM BGT226, 5μM OSI-027, 5μM AZD8055). (G) Live cells invaded past fixed threshold set by 90^{th} percentile invasion distance of genotype-matched vehicle control, upon three-day mTOR inhibitor treatment (8nM BGT226, 1μM OSI-027, 200nM AZD8055) ± 20nM rapamycin (mean ± SD; * = $p < 0.05$ by Student t-test; n = 3).

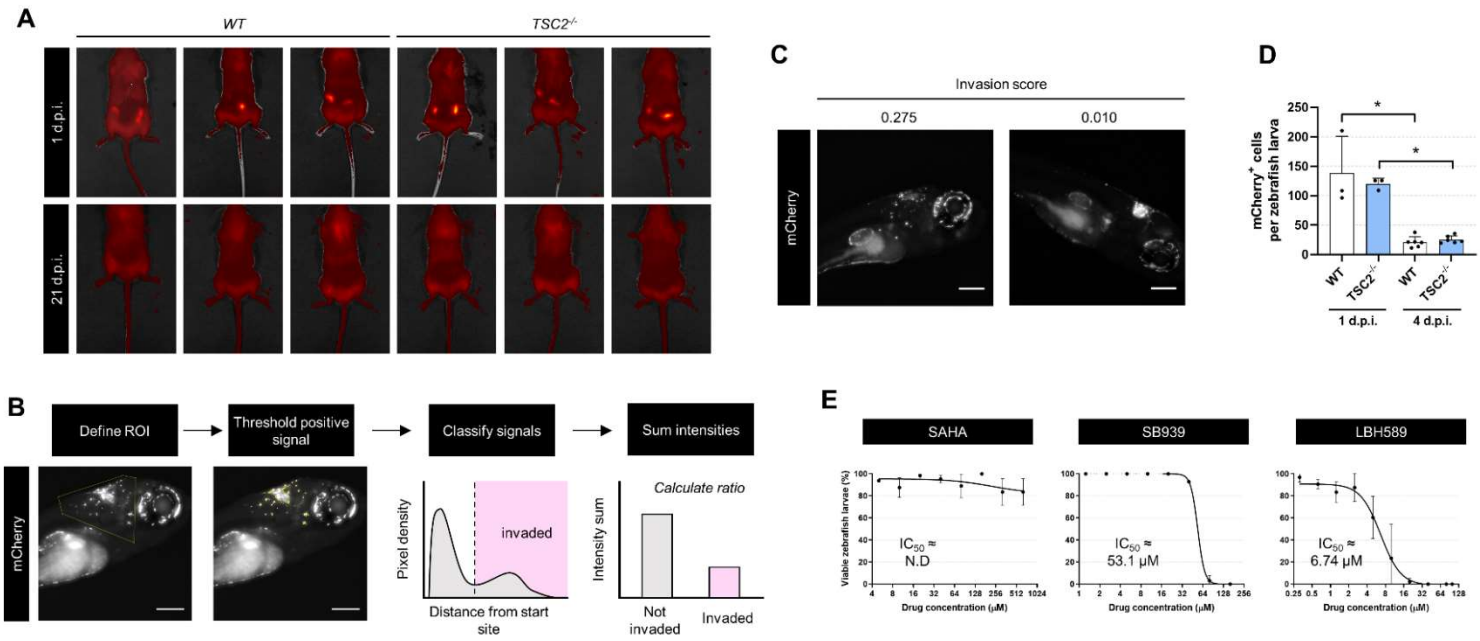

Fig. S6. HDAC inhibitors are anti-invasive and selectively cytotoxic towards TSC2$^{-/-}$ cells xenotransplanted into zebrafish. (A) Visualization of mCherry^{+} cells by IVIS following subcutaneous transplantation into rear flanks of immunodeficient NSG mice. (B) Schematic representation of invasion score calculation in zebrafish larvae. See Supplementary Materials and Methods for more details. Scale bars of 200µm. (C) Representative images of *TSC2*$^{-/-}$ mCherry^{+} cells disseminated 4 dpi with the associated invasion score. Scale bars of 200µm. (D) Number of mCherry^{+} cells per zebrafish detected by flow cytometry following whole larvae dissociation at 1 and 4 dpi. Each replicate is a pool of 15 – 20 zebrafish larvae (mean ± SD; * = $p < 0.05$ by Student t-test; n = 3 – 6). (E) Dose-toxicity curves of zebrafish larvae treated with HDAC inhibitors by immersion therapy.

SUPPLEMENTARY TABLES

Table S1. Differential gene expression analysis of bulk RNA-seq data, untreated samples only. (A) DEG analysis of genotype (*TSC2*$^{-/-}$ vs. WT), controlling for substrate covariate. (B) DEG analysis of substrate (hydrogel vs. plastic), controlling for genotype covariate. (C) DEG analysis of interaction between genotype and ECM.

Table S2. GO term enrichment analysis of DEG lists. (A) GO term enrichment in *TSC2*$^{-/-}$ vs. WT DEG list (FDR < 0.05, $|\log_2 FC| > 1$). (B) GO term enrichment in hydrogel vs. plastic DEG list (FDR < 0.05, $|\log_2 FC| > 1$). (C) GO enrichment of genotype:substrate interaction DEG list (FDR < 0.05).

Table S3. Three-dimensional drug screen raw data. (A) Compound information from Ontario Institute of Cancer Research kinase inhibitor and tool compound libraries. (B-C) Cytotoxicity and invasion modulation effects of compounds, (B) statistic descriptions and (C) raw data.

Table S4. Enrichment results via adaptation of GSEA. Results for statistics of (A) selective cytotoxicity, positive enrichment (i.e., selectively cytotoxic towards *TSC2*$^{-/-}$), (B) selective cytotoxicity, negative enrichment (i.e., selectively cytotoxic towards WT), (C) invasion modulation, positive enrichment (i.e., attenuate invasion), (D) invasion modulation, negative enrichment (i.e., potentiate invasion).

Table S5. Elion^{TM} structure-based compound analysis. (A-B) Significantly enriched targets and mechanisms of action by (A) selective cytotoxicity towards *TSC2*$^{-/-}$ cells and (B) invasion attenuation. (C-D) Significantly enriched GO and PFAM terms (based on significantly enriched targets) by (C) selective cytotoxicity towards *TSC2*$^{-/-}$ cells and (D) invasion attenuation.

SUPPLEMENTARY MOVIES

Movie S1. Brightfield Z-stack of WT invading through the hydrogel, counterstained with Hoechst.

Movie S2. Brightfield Z-stack of *TSC2*$^{-/-}$ invading through the hydrogel, counterstained with Hoechst.

SUPPLEMENTARY MATERIALS AND METHODS

Study reagents and resources

Please see below (**Table 1**) for a list of key reagents and resources used in this study.

Table 1: List of key reagents and resources used in this study.

REAGENTS and RESOURCES	SOURCE	IDENTIFIER
Antibodies		
PMEL	Thermo Fisher Scientific	MA5-13232
ACTA2	Abcam	ab5694
mCherry	Abcam	ab167453
pS6RP (Ser 235/236)	CST	2211
p4E-BP1(Thr 37/46)	CST	2855
S6RP	CST	2317
4E-BP1	Thermo Fisher Scientific	AHO1382
TSC2	CST	4308
ACTB	CST	370
Cleaved CASP3	CST	9661
mCherry	Thermo Fisher Scientific	M11217
AlexaFluor 488 Goat Anti-Rabbit IgG (H+L)	Thermo Fisher Scientific	A11034
AlexaFluor 488 Goat Anti-Mouse IgG (H+L)	Thermo Fisher Scientific	A11001
AlexaFluor 555 Goat Anti-Rabbit IgG (H+L)	Thermo Fisher Scientific	A21428
AlexaFluor 555 Goat Anti-Mouse IgG (H+L)	Thermo Fisher Scientific	A32727
AlexaFluor 647 Goat Anti-Rabbit IgG (H+L)	Thermo Fisher Scientific	A21245
AlexaFluor 647 Goat Anti-Mouse IgG (H+L)	Thermo Fisher Scientific	A21235
AlexaFluor 680 Goat Anti-Rabbit IgG (H+L)	Thermo Fisher Scientific	A21076
AlexaFluor 680 Goat Anti-Mouse IgG (H+L)	Thermo Fisher Scientific	A28183
DyLight 800 Goat Anti-Rabbit IgG (H+L)	Thermo Fisher Scientific	SA535571
DyLight 800 Goat Anti-Mouse IgG (H+L)	Thermo Fisher Scientific	SA535521
Live cell imaging dyes		
Hoechst 33342	Thermo Fisher Scientific	H3570
SyTOX Green	Thermo Fisher Scientific	S7020
NucView 488 Caspase-3 Enzyme Substrate	Biotium	10402
Annexin V	Biotium	29003
Small molecules		
Kinase Inhibitor library	Ontario Institute for Cancer Research	N/A
Tool Compound library	Ontario Institute for Cancer Research	N/A
Rapamycin	MilliporeSigma	553211
Staurosporine	AdooQ Bioscience	A10864
SAHA	AdooQ Bioscience	A10979
SB939	AdooQ Bioscience	A10830
LBH589	AdooQ Bioscience	A10518
BGT226	AdooQ Bioscience	A11162
OSI-027	Toronto Research Chemicals	A611910

AZD8055	AdooQ Bioscience	A10114
Y-27632	AdooQ Bioscience	A11001
PR-171 (Carfilzomib)	AdooQ Bioscience	A11278
BMS-354825 (Dasatinib)	AdooQ Bioscience	A10290
EdU	Thermo Fisher Scientific	A10044
Sulfo-Cy5-N_3	Lumiprobe	A333
Buprenophrine	Provided by animal facility	N/A
Hydrogel reagents		
Sodium hyaluronate	Lifecore	HA-200K
5-Methylfurfurylamine	TCI Chemicals	MFCD00143471
Methylcellulose	Spectrum Chemicals	ME137
Vitronectin peptide	Synthesized in house	N/A
MMP-degradable cross-linker	Synthesized in house	N/A
Silica beads	VWE	CA75873-698
Hyaluronidase	Sigma-Aldrich	H3884
Cell culture reagents		
Essential 8	Prepared in house	N/A
Matrigel	Corning	354230
Dispase	Stem Cell Technologies	7913
Medium 231	Thermo Fisher Scientific	M-231-500
Smooth Muscle Growth Supplement	Thermo Fisher Scientific	S00725
Trypsin	Thermo Fisher Scientific	25300062
Collagenase from Clostridium histolyticum	Sigma-Aldrich	C0130
Ethyl 3-aminobenzoate methanesulfonate (Tricaine)	Sigma-Aldrich	E10521
Accutase	Stem Cell Technologies	7920
Commercial kits and materials		
VEGF-D DuoSet ELISA Kit	R&D Systems	DY622
BOLT 4-12% 1 mm, 10-well gel	Thermo Fisher Scientific	NW04120BOX
Stain-Free 4–20% 1mm 15-well gel	Bio-Rad	4568096
NucleoSpin® RNA 740955.250 D-Mark Bio	Machery-Nagel	740955.250
Cell models		
H9 human embryonic stem cell, WT	WiCell	WB67614
H9 *TSC2*$^{-/-}$	Generated in house *(14)*	N/A
H9 teratoma-derived LAM cells (WT and *TSC2*$^{-/-}$)	Generated in house	N/A
Animal models		
NOD.Cg-*Prkdc*^{scid} *Il2rg*^{tm1Wjl}/SzJ (NSG)	Jackson Laboratory	005557
casper mutant zebrafish	Gift from Dr. Leonard Zon *(41)*	N/A
Software and algorithms		
ImageJ 1.53c	ImageJ	N/A
R 4.0.3	R	N/A
RStudio 1.3.1093	RStudio	N/A
Gene Set Enrichment Analysis (GSEA)	*(43)*	N/A
Mechanism of Action Miner (Elion™)	BioSymetrics	Described here

Cell culture

Pluripotent stem cell culture

H9 hPSCs (female) were maintained on a thin layer of 0.16 mg/mL Matrigel at 37ºC, 10% CO_2. Cells were fed with Essential 8 media, prepared in house. Cells were passaged by incubation with 500 µM EDTA for 3 min., then cell scraping and transfer to a new pre-coated plate by wide-bore pipette.

LAM and control cell model derivation and culture

LAM cell models were established via a previously reported *in vivo* differentiation protocol of human pluripotent stem cells *(23)*. We differentiated a previously reported pair of mCherry^{+} WT and genome-engineered *TSC2*$^{-/-}$ hPSCs, derived from the H9 parental lineage (female cells) *(14)*. First, we generated teratomas in female NOD.Cg-*Prkdc*^{scid} *Il2rg*^{tm1Wjl}/SzJ (NSG) mice as described in Mouse teratoma formation section. At end point, mice were euthanized and dissected under sterile conditions. The teratomas were extracted while carefully ensuring minimal mouse tissue remnants. The teratoma was minced and then rotated in a 5 U/mL Dispase solution at 37ºC for 30 mins. Digested tissue was plated on a thin layer of 0.16 mg/mL Matrigel at 37ºC, 5% CO_2 in Medium 231 containing Smooth Muscle Growth Supplement. Tissue clumps were removed the following day. The remaining monolayer was expanded and passaged by treatment with 0.05% Trypsin for 5 min. Maintenance culture conditions included a thin layer of 0.16 mg/mL Matrigel at 37ºC, 5% CO_2 in Medium 231 containing Smooth Muscle Growth Supplement. Cells were expanded for two passages before cryopreservation and use in subsequent experiments at passages 3-5.

LAM and control cell model clonal isolation

LAM cells were clonally isolated by limiting dilution. Briefly, bulk cell cultures were dissociated and serially diluted to a concentration of ~ 0.3 cells / 100 μL. We used this concentration to optimize number of single cells isolated while minimizing two or more cells contributing to a single clone. We added 100 μL of the suspension to each well of a 96-well plate containing a thin layer of 0.16 mg/mL Matrigel. Clones were expanded for 10 days before dissociating and plating onto the hydrogel.

Hydrogel culture

Reagent production

Hydrogel culture was conducted according to a previously established protocol *(18)*. Briefly, a hyaluronic acid polymer backbone was derivatized with 5-methylfurfurylamine to 65% substitution (confirmed by ^{1}H NMR). A vitronectin-mimetic peptide (maleimide)-KGGPQVTRGDVFTMPG, and MMP-degradable peptide crosslinker (maleimide)-KKGRGPQGIWGQKGPQGIWGQ-K(maleimide)S were synthesized using microwave-assisted Fmoc solid phase peptide synthesis with a CEM Liberty Blue automated peptide synthesizer. Hydrogel viscoelasticity was increased by incorporation of methylcellulose derivatized with reactive thiol groups.

Hydrogel gelation and culture

All chemically synthesized hydrogel components were mixed to the following final concentrations: 0.9 % methylfuronated hyaluronate, 2.3 mM MMP crosslinker, 100 μM vitronectin peptide, and 0.05 mg/mL thiolated methylcellulose. 15 μL of the solution was added

to each well of a 384-well plate and permitted to gel at 37ºC for 3 hours. Following gelation, wells were hydrated with PBS and then subjected to three media washes interspaced with incubations at 37ºC for 45 mins. LAM or control cells were then dissociated, added to plates containing hydrogel, and spun for 3 min. at 10*g* to achieve immediate contact with the hydrogel.

Cell treatments

Drug treatments

All small molecule compounds were diluted in either DMSO or PBS, unless otherwise stated. The appropriate diluent-matched vehicle control was included in every experiment. Drug treatments were added directly to wells containing cells at 5X concentrations to avoid washing off any cells, particularly in sensitive miniaturized formats. Rapamycin was consistently used at a 20nM concentration. All compound treatments were conducted for 72 hours unless otherwise stated.

Live cell staining

Live cell staining dyes were used at the following final concentrations: 10 µg/mL Hoechst 33342, 50 nM SyTOX Green, 4 µM Caspase-3 Enzyme Substrate, and 0.2 µg/mL Annexin V. Dyes were incubated for 30 min. prior to imaging and added as 10X concentrates in PBS; Annexin V diluent also contained 2.5mM $CaCl_2$. To avoid cell detachment in the miniaturized well format, live imaging dyes were not washed prior to imaging; this did not impact image acquisition as dyes are minimally fluorescent unless bound to the target molecule.

Cytotoxicity-invasion assay

Cells were permitted to invade through the hydrogel (384-well format) for 72 hrs while incubated at 37ºC and 5% CO_2. At end point, Hoechst and SyTOX were added directly to all wells as described in **Cell treatments** section. Whole-well multi-planar images were acquired by widefield microscopy with 40 µm separation between z-stacks. Following image acquisition, wells were fixed overnight in 10% formalin. We then added 1µg of silica beads to each well and acquired multiplanar brightfield images, with the plane of maximal contrast used to determine hydrogel-liquid interface (described in **Image analysis**). Acquiring location of the hydrogel interface (i.e., start of the cellular position) is essential for accurate invasion distance calculation; the hydrogel exhibits a meniscus which leads to a variable Z starting position depending on the XY location.

Three-dimensional drug screen

Screen design

Both WT and *TSC2*$^{-/-}$ cells were treated with every drug from the Ontario Institute for Cancer Research (OICR) Kinase Inhibitor and Tool Compound library (total of 800 compounds) at a concentration of 5 µM ± 20nM rapamycin. Cells were treated for 72 hr. while cultured in hydrogel and assessed at end point for cytotoxicity and invasion modulation as described in **Cytotoxicity-invasion assay**. Each plate included internal vehicle-treated only controls. Z' was calculated for cytotoxicity and invasion modulation using vehicle-treated samples (negative control), 10 µM Y27632-treated (positive control, invasion), and 5 µM Carflizomib-treated (positive control, cytotoxicity).

Compound score calculation

To identify drugs with statistically significant effect(s), we computed z-scores for invasion modulation, cytotoxicity, selective invasion modulation, and selective cytotoxicity, for each WT and *TSC2*$^{-/-}$ in the presence or absence of rapamycin. We confirmed that the reference population of vehicle-treated controls for each metric was normally distributed and variance did not vary with effect mean. Cytotoxicity is determined by the percentage of SyTOX^{+} cells; invasion modulation is determined by the percentage of cells invading past the vehicle-control median threshold (See Image analysis section). Selective cytotoxicity is determined by the difference in cytotoxicity between WT and *TSC2*$^{-/-}$ cells, where positive values indicate more dead cells in the *TSC2*$^{-/-}$ condition. Selective invasion modulation is determined by the difference in cytotoxicity between *TSC2*$^{-/-}$ and WT cells, where positive values indicate fewer invading cells in the *TSC2*$^{-/-}$ condition. We then calculated p-values and corrected for multiple hypothesis testing by computing false discovery rates. All computation was performed using R 4.0.3 and RStudio 1.3.1093.

Target enrichment analysis

To refine our candidate compound list, we performed target enrichment analysis using a modified version of the GSEA algorithm *(43)*. Enrichment analysis was performed separately for cytotoxicity and invasion modulation. For cytotoxicity, we focused our compound list to drugs that showed selective cytotoxicity, either in the presence or absence of rapamycin. If a drug was shown to be significantly beneficial in one condition but significantly detrimental in the other, it was excluded. We then derived a singular compound score by computing the arithmetic mean across the two conditions. Similarly, for invasion modulation, we focused our compound list to

drugs that exhibit anti-invasion effects towards WT or *TSC2*$^{-/-}$ cells, either in the presence or absence of rapamycin. Again, we excluded compounds that showed opposing effects, and derived a singular compound score by arithmetic mean across conditions.

We next generated a background target list using known compound targets as annotated by the OICR. We created generalizable categories wherever possible, however, there were many targets that could not be grouped and conferred an n = 1 category. To avoid the possibility of bias, these categories were established by an independent author blinded to the original compound results. Using this background list and our compound score lists as described above, we determined target enrichment using the GSEA algorithm *(43)*.

Elion^{TM} *analysis*

A limitation to our analyses is the small number of compounds which were identified to selectively eliminate *TSC2*$^{-/-}$ cells. We sought to extend our compound list *in silico* using a structure-based approach with Elion^{TM} (Mechanism of Action Miner), conducted by an independent group. Elion^{TM} is a software package that ingests binary phenotypic data linked to individual drug treatments to suggest possible underlying protein targets and molecular pathways. The platform inputs phenotypic screening data in the form of a two-column CSV file corresponding to the chemical structure in SMILES format alongside a binary bioactivity reading.

Using this dataset, a total of 8,000 features are generated for each supplied chemical structure. These features are comprised of chemical fingerprints (ECFP4, FCFP4, RDK-layered fingerprint, and MACCS) alongside physical properties (e.g., molecular weight, total polar surface area, LogP). If there are fewer than 8,000 rows in the input data set, a subset of features

are chosen for downstream machine learning. The size of this feature subset is set to be 70% of the number of rows in the input data set. Feature selection is performed using a bootstrapped logistic regression strategy. In brief, a set number of features are sampled from the original feature set and are used to train a logistic regression model. The coefficients of this model are then used to rank feature importance. This process is repeated 5,000 times and the resulting coefficients are averaged for each feature to create a summarized feature importance score.

Once a feature set is chosen, a total of 6 machine learning models are built and evaluated on the input data set (XGBoost, random forest, Gaussian naive Bayes, uniform and distance weighted K-nearest neighbours, and Gaussian process classifiers). Each model is trained and evaluated using 10-fold cross validation while recording classification performance according to accuracy, ROC-AUC, precision and recall. The best performing model is then chosen and used to rank a set of 1 million compounds (curated from public databases) according to probability of inducing the given phenotype.

Of the 1M ranked compounds, several are annotated according to experimentally validated protein targets and mechanisms of action. The GSEA algorithm is used to determine which of these targets and MoAs are most positively enriched within the ranked set of compounds. We then subset this list using an FDR threshold to identify a set of enriched targets and MoAs. Using the enriched targets, we perform gene ontology and protein family pathway enrichment using the Fisher exact test. A Bonferroni corrected p-value threshold of 0.05 is used to identify cellular pathways corresponding to the phenotype of interest.

As a result of this process, Elion^{TM} translates an input phenotypic screen into three informative outputs. First, it supplies a ranked list of publicly available compounds prioritized according to their likelihood to induce the given phenotype. Second, it provides a list of targets

and MoAs likely to mitigate the provided phenotype. Last, it annotates these targets with enriched cellular pathways. All of these results are presented in a web application annotated with rich descriptions and link-outs to relevant genetic databases.

Image analysis

Identification of cell spatial positions and cell invasion distance

We identified XYZ cell positions in the hydrogel by analysis of the Hoechst channel z-stack. We first determined XY positions by employing the ImageJ 1.53c "Find maxima" function on the z-stack maximum intensity projection. We automated the determination of the noise (or background) threshold by empirical iteration. Using the assumption that true Hoechst signal should be substantially above background fluorescence, we computed "Find maxima" with a liberal threshold, and then progressively increased threshold stringency until the number of identified points did not vary with each stepwise threshold change. Each maxima was determined to correspond to a single cell spatial location. Following, for each XY spatial position, we iterated through the Hoechst z-stack and identified to the point of maximal intensity, corresponding to the cell Z position.

To determine the invasion distance of each single cell, we must first know the cell starting position, which varied across XY positions due to the meniscus exhibited by the hydrogel. To identify determine hydrogel interface Z position across the XY plane, we used the silica bead brightfield images (described in Cytotoxicity-invasion assay). For each XY cell spatial position, we iterated through the brightfield z-stack and identified the point of maximal contrast, which corresponded to the layer containing silica beads (due to diffraction). We then determined individual cell distances travelled by computing the difference between cell starting

and final positions. This process, automated for high throughput analysis, was scripted in ImageJ 1.53c.

Binarization of live cell stains

Live cell stains (i.e. SyTOX, Caspase-3 enzyme substrate, and Annexin V) were binarized into a positive or negative signal for each cell. We first created a masking around the Hoechst signal of each cell in the maximum intensity projection image, then measured the total fluorescent signal of the live cell stain within each masking. To binarize in an automated fashion, we fit an empirical probability density function (ePDF) by kernel density estimation on the vehicle control sample values. Assuming the majority of untreated samples should be negative for cell death stains, we determined the threshold for binarization to by the first local minimum of the negative control ePDF. Cells across conditions were then binarized according to their matched control threshold. This process, automated for high throughput analysis, was scripted in ImageJ 1.53c and R 4.0.3 within the RStudio 1.3.1093 environment.

Quantification of cellular invasion

Cellular invasion was determined by number of cells invading past a fixed distance. As the invasion distance varied slightly batch to batch (see Fig. 1F), distance thresholds for each experiment were based on within-experiment vehicle controls. We used both the median invasion of vehicle controls, which is sensitive to detecting decreases in invasion, and 90^{th} percentile invasion of vehicle controls, which is sensitive to detecting increases in invasion. Genotype-specific thresholds were employed due to the differing invasion distances between WT and *TSC2*$^{-/-}$ cells. To determine invasion of alive cells only, SyTOX^{+} positive cells were removed

from the distribution prior to calculation of invasion percentages. This process, automated for high throughput analysis, was scripted in R 4.0.3 within the RStudio 1.3.1093 environment.

Immunofluorescence stain quantification

Immunofluorescence experiments were quantified using the raw image files, ensuring the absence of detector saturation. We created a masking around the Hoechst signal of each cell in the maximum intensity projection image, then measured the mean fluorescent signal of the protein-of-interest within the total masking area. Measurements per replicate were re-scaled from 0 – 1 by dividing by the replicate maximum value. We note that comparisons between plastic and hydrogel samples cannot be directly made, as the imaging parameters differ between the two-dimensional vs. three-dimensional environment (see Fig. 2B).

Invasion quantification upon zebrafish xenotransplantation

Invasion of transplanted mCherry$^+$ cells was performed in a semi-automated fashion on blinded images (Fig. S6B). For each image, a region of interest was manually selected on the maximum intensity Z projection, to distinguish areas with mCherry$^+$ cells from surrounding auto-fluorescent regions (e.g., zebrafish eye, yolk sac, ossicle). Images were then binarized using a constant threshold to distinguish positive signal from background. Pixels were classified into "invaded" or "not invaded" based on the distance from the center of the initial injection site. We used the average of the first local minima of the positive pixel histogram from 1 day post injected images to determine the distance for classification of invaded or not. Following pixel classification, the ratio of the total positive pixel intensity in each group was computed to

determine the zebrafish invasion score. Groups were then unblinded and graphed. This process was scripted in ImageJ 1.53c and R 4.0.3 within the RStudio 1.3.1093 environment.

RNA-seq

RNA extraction and quality control

Extraction of RNA from cells embedded in hydrogel is made challenging by the low cellular density relative to the abundant extracellular matrix. To extract RNA, we developed an extraction protocol that combines phenol-chloroform phase separation with column-based purification. We first added TriZOL directly to wells and homogenized the cell-hydrogel mixture using a 26-gauge needle. We then centrifuged the lysate for 5min, 12,000*g*, at 4ºC to pellet the cross-linked hyaluronic acid matrix. We extracted the supernatant and mixed in chloroform, followed by centrifugation to induce phase separation. The colourless aqueous phase was extracted and mixed with equal volumes of 70% EtOH. Following a brief incubation at room temperature, the solution was eluted through a Machery-Nagel Nucleospin column. We proceeded with column-based purification as per manufacturing protocol.

RNA-sequencing and raw data processing

RNA samples were shipped to the Donnelly Sequence Centre (Toronto, Canada) for RNA quality-control, library preparation, and next-generation sequencing. RNA integrity was assessed via Bioanalyzer (Agilent) and only samples with RIN > 8 were prepared for sequencing. Oligo(dT) priming via SMART-Seq v4 (Takara Bio) preparation kit was used to generate full-length cDNA libraries. Samples were subjected to paired-end sequencing on a NovaSeq 6000, 100c (Illumina) to a depth of ~50 million reads per sample.

Raw sequence read quality was assessed by *FastQC*. Read feature assignments and duplication rates were determined using *featureCounts* and *Picard*. Overall mapping rate was assessed with *HISAT2*. Finally, read assignment to transcripts was performed using *Salmon*, generating a final pseudocount abundance matrix. All QC processing was summarized using *MultiQC* and programmed in R 4.0.3 within the RStudio 1.3.1093 environment. RNA-seq data is accessible at the Gene Expression Omnibus (GEO) repository with accession GSE179044.

Differential gene expression and enrichment analysis

Pseudocount abundance data generated by *Salmon* was imported into the *DEseq2* framework in R for differential expression and enrichment analysis. Principal components analysis was conducted on all samples to visualize transcriptomes in a two-dimensional space. For single variable differential expression testing, we subsetted samples to only include the untreated and fit the following model: ~ *batch* + *genotype* + *substrate*. We then tested for genes with significant coefficients by Wald test, separately for genotype and for culture substrate. To assess for changes across genotype that differs between matrix condition, we again subsetted for untreated samples and fit the following model: ~ *batch* + *genotype* + *substrate* + *genotype:substrate*. The interaction term coefficient for each gene was tested for significance by Wald test. Differentially expressed genes were called when false discovery rate (FDR) < 0.05, $\pm$ $|\log2FoldChange| > 1$ (as indicated in the text).

To visualize expression values by heatmap or gene cluster, sample conditions were collapsed by abundance summation, normalized, and then transformed by regularized $\log_2$ transformation (implemented in *DEseq2*). Heatmaps were generated using the *pheatmap* package in R and gene clusters were generated by hierarchal clustering. GO term enrichment was

performed using *clusterProfiler* on significant DEGs (FDR < 0.05, ± |log2FoldChange| > 1). All analysis was conducted using R 4.0.3 within the RStudio 1.3.1093 environment.

Animal studies

Mouse teratoma formation

hPSCs were dissociated into single cells by Accutase treatment for 15 min at 37ºC. Single cells were harvested, washed, and resuspended in 5 mg/mL Matrigel. Female 8-week-old NSG mice were treated with buprenophrine 1 hour before injection, then anesthetized by isofluorane under a continuous stream of O_2. We bilaterally injected $1x10^6$ hPSC into the mouse tibialis anterior. We allowed teratomas to grow over a 12-week period, after which mice were sacrificed and teratomas extracted.

Mouse subcutaneous xenografts

LAM cells were dissociated into single cells by 0.05% Trypsin treatment for 5 min. at 37ºC, washed, and resuspended in 5 mg/mL Matrigel. Female 8-week-old NSG mice were anesthetized by isofluorane under a continuous stream of O_2 and injected with $1x10^6$ cells subcutaneously in each rear flank. We monitored for palpable tumor growth weekly over a four-month period, after which animals were sacrificed.

Mouse IVIS image acquisition

Female 8-week-old NSG mice that were injected with LAM cells in each rear flank were monitored for tumor growth by endogenous mCherry expression of LAM cells. Mice were anesthetized by isofluorane under a continuous stream of O_2 and shaved to eliminate background

fluorescence from the fur coat. Mice were then imaged at fixed exposure times by *in vivo* imaging (PerkinElmer, IVIS®).

Zebrafish toxicity assay

72-hour post-fertilization (hpf) zebrafish larvae were arrayed one larva per well in a 96-well plate and treated with increasing concentrations of each inhibitor for 72 hrs to ascertain toxicity thresholds. There were no *in vivo* toxic effects at the experimental *in vitro* concentrations and thus, zebrafish experimental doses were chosen to stay consistent with *in vitro* treatment doses.

Zebrafish hindbrain ventricle xenotransplantation

For each injection experiment, a separate cryovial of cells was thawed and cultured 3 days prior to zebrafish transplantation, without any subculturing. On the day of transplantation, cells were dissociated by 0.25% trypsin, centrifuged for 5 mins at 300*g*, and resuspended in approximately 30 μL of culture medium for injection. 72 hpf zebrafish larvae were anesthetized with 0.09 mg/mL tricaine (Millipore Sigma) and arrayed in troughs of an agarose injection plate and used for cell transplantation using protocols described previously *(44, 45)*. The cells were backloaded into a pulled capillary needle and allowed to settle for approximately 20 mins at 35°C to ensure a cell pellet at the bottom of the needle. A PLI-100A Pico-liter Microinjector (Warner Instruments) was used to manually inject 50-100 cells into the hindbrain ventricle (HBV) of each larva. Following injections, the larvae were kept at 35°C for the remainder of the experiment.

Zebrafish drug treatments

1 day post injection (dpi), injected larvae were screened on an Axio Observer 7 fluorescent microscope under an mCherry filter to ensure the presence of cells only in the HBV. Groups of 20-30 positively injected larvae were randomized into groups to be treated with either vehicle control (DMSO), 20 nM rapamycin alone, 5 μM SB939 alone, 20 μM SAHA alone, 1 μM LBH589 alone or with one HDACi in combination with rapamycin by immersion therapy for 72hrs. At the experimental endpoint (3 days post-treatment) the groups of larvae were blinded and imaged on the Axio Observer 7 using the z-stack function to capture cell movement in all planes. Blinded groups of images were then subjected to automated invasion analysis by an independent study author.

Zebrafish whole larval dissociation and fixation

At 1 dpi (baseline) and 4 dpi (three days post-treatment), 20 larvae from each group were euthanized and dissociated in 100mg/mL collagenase solution for approximately 30 mins. Upon completion of dissociation (i.e., single cell suspension formed), 200 μL of 100% FBS was added to slow the enzymatic reaction. The samples were then centrifuged for 5 min. at 300 *g* and the supernatant was removed, leaving a pellet of human tumor cells among the zebrafish cells. The samples were washed once in 30% FBS in PBS and centrifuged once more for 5 min. at 300 *g*. The supernatant was removed and 250μL of 4% PFA in PBS was added to each sample for 20 min. in the dark. 1mL of PBS was added and samples were centrifuged and PFA supernatant was removed. Samples were resuspended in 500 μL PBS, stored at 4°C, and blinded prior to flow cytometry analysis.

Immunofluorescence staining

The following protocol is for immunofluorescence staining of cells in monolayer culture on plastic. Modifications for whole-mount (WM) staining of cells in three-dimensional hydrogel are indicated throughout.

Cells were fixed with 4% PFA for 15 min. (WM: 30 min.) at room temperature. Wells were washed 3 x 5 min. (WM: 20 min.) with PBS, then permeabilized with 0.1% Triton-X in PBS for 20 min. (WM: 40 min) at room temperature. Wells were washed 3 x 5 min. (WM: 20 min.) with PBS, then blocked with 1% BSA in PBS for 1 hr. (WM: 2 hr.) at room temperature. We then added primary antibody diluted in blocking solution for overnight incubation at 4°C. The following concentrations of antibodies were employed: PMEL (1:50), ACAT2 (1:100), pS6RP$^{Ser235/236}$(1:100), and p4E-BP1$^{Thr37/46}$(1:200). The next day, wells were wash 3 x 5 min. (WM: 5 x 30 min.) with PBS, then incubated with fluorescent secondary antibodies diluted blocking solution for 1 hr. (WM: 2 hr.) at room temperature. All fluorescent secondary antibodies were used at a 1:1000 dilution. Wells were then washed 3 x 5 min. (WM: 5 x 30 min.) with PBS then counterstained with 10 µg/mL Hoechst 33342 for 30 min. (WM: 45 min.) Wells were washed 3 x 5 min (WM: 5 x 30 min.), then mounted with a 90% glycerol (WM: PBS, as the hydrogel disintegrates in glycerol) solution made in house, prior to imaging.

Enzyme-linked immunosorbent assay (ELISA)

Maintenance cultures of cells at equivalent densities were incubated for 16 hr. in Medium 231 ± 20nM rapamycin, without serum supplement. Conditioned media was collected and centrifuged to remove any cellular debris, then assayed by VEGF-D ELISA kit (R&D Systems, DY622) following the manufacturer protocol.

Flow cytometry

LAM cells were dissociated into single cells by 0.05% Trypsin treatment for 5 min. at 37°C, washed, and then fixed with 4% PFA for 15 min. at room temperature. Fixing solution was diluted out 1/10 in PBS, cells were pelleted by centrifugation, and supernatant discarded. For details on zebrafish single cell preparation, see Zebrafish whole organism dissociation and fixation section. Fixed single cell suspensions were permeabilized with 0.1% Triton-X in PBS for 20 min. at room temperature. Permeabilizing solution was diluted out 1/10 in PBS, cells were pelleted by centrifugation, and supernatant discarded. Samples were then blocked with 1% BSA or 5% Goat Serum in PBS for 1 hr. Cells were pelleted by centrifugation, supernatant discarded, and primary antibodies diluted in blocking solution were added for overnight incubation at 4°C. The following concentrations of antibodies were employed: PMEL (1:50), ACAT2 (1:100), mCherry (1:1000), and Cleaved CASP3 (1:500). The next day, primary antibody solution was diluted out 1/10 in PBS, cells were pelleted by centrifugation, and supernatant discarded. Samples were then incubated with fluorescent secondary antibodies diluted blocking solution for 1 hr. at room temperature. All fluorescent secondary antibodies were used as a 1:1000 dilution. Secondary antibody solution was diluted out 1/10 in PBS, cells were pelleted by centrifugation, and supernatant discarded. Samples were next counterstained with 10 µg/mL Hoechst 33342 for 20 min. at room temperature. Hoechst 33342 solution was diluted out 1/10 in PBS, cells were pelleted by centrifugation, and supernatant discarded. Finally, cells were strained and analyzed using the LSRFortessa (BD) flow cytometer.

Low input western blot

Hydrogel culture must be performed in a miniaturized format to maintain the appropriate mechanics as previously reported *(18)*. Naturally, this poses a challenge for collecting sufficient protein for standard molecular biology methods, such as a western blot. To address this challenge, we developed a method for a low input western blot that includes in-well lysis and sample preparation, followed by a gel-based method for sample normalization.

Samples were cultured on plastic or in hydrogel for 72 hr. Following, sample media was aspirated to the hydrogel interface (leaving a similar volume in plastic wells) and an equivalent volume of 2X Laemmli-RiPA buffer was added to each well. Samples were incubated for 10 min. at 37^{o}C and triturated up and down, careful not to disturb the hydrogel. The sample volume was then extracted and boiled for 10 min. at 70^{o}C. As this extraction contains a large amount of non-cellular derived protein components (due to degradation of the hydrogel MMP-cleavable crosslinkers), standard protein quantification by colorimetric methods (e.g., BCA, and Bradford) are not reliable. Instead, we performed total protein quantification on gel-separated samples. First, an aliquot of each sample was electrophoresed on a stain-free 4–20% 1 mm 15-well gel, along with a serial dilution of a sample of known concentration. The gel was then activated by UV exposure and total protein visualized by ChemiDoc Gel Imager (Bio-Rad). We then calculated individual sample concentrations by comparing against the within-gel standard curve, without including bands corresponded to the hydrogel MMP peptides.

After sample extraction and quantification, we analyzed samples following standard western blotting procedures. To maximize sample input, Thermo Fisher Scientific BOLT gels were used, which contain space for up to 60 µL of sample per lane. We first separated samples by SDS-PAGE using a BOLT 4-12% 1 mm 10-well gel and MES running buffer. Samples were transferred onto a 0.45 µm PVDF membrane overnight at 4^{o}C by wet transfer with Towbin

buffer (containing 0.025% SDS and 10% MeOH). The membrane was then blocked by 5% BSA in PBS-T (0.1% Tween-20) for 1 hr. at room temperature. Following, the membrane was incubated overnight at 4°C in primary antibodies diluted in blocking buffer at the following concentrations: pS6RP$^{Ser235/236}$(1:5000), p4E-BP1$^{Thr37/46}$(1:1000), S6RP (1:500), 4E-BP1 (1:1000), TSC2 (1:5000), and ACTB (1:5000). The membrane was washed 3 x 5 min. with PBS-T, and then incubated for 1 hr. at room temperature in fluorescent secondary antibodies diluted 1:10,000 in blocking buffer. The membrane was washed 3 x 5 min. with PBS-T and then imaged using Odyssey Gel Imager (LI-COR Biosciences).

EdU proliferation assay

Cells were pulsed with 5 μM of EdU for 3 hr. Subsequently, cells were fixed with 4% PFA for 15 min. at room temperature. Wells were washed 3 x 5 min. with PBS, permeabilized with 0.1% Triton-X in PBS for 20 min. at room temperature, then washed again 3 x 5 min. We prepared the click reaction by mixing the following components in the described order, in PBS, to the indicated final concentrations: 4 mM Cu_2SO_4, 5 μM Sulfo-Cy5-N_3, and 100 mM L-ascorbic acid. The click reaction mix was added to wells containing cells and incubated at room temperature for 30 min. Wells were washed 3 x 5 min. with PBS, counterstained with 10 μg/mL Hoechst 33342 for 30 min, washed again 3 x 5 min., and then imaged.

Clonogenic assay

Cells were plated on the hydrogel and treated with HDAC inhibitors at the designated concentration for 72 hr. Following treatment, wells were washed 3 x 20 min. with media to remove the drug from solution. The hydrogel was then solubilized by addition of 150 U hyaluronidase per 15 μL hydrogel and incubated for 1 hr. at 37°C. Following, 0.05% Trypsin

was added to the wells for 10 min. at 37ºC to dissociate cells. Wells were triturated and then plated on two-dimensional tissue cultures plates, in serial dilution. Cells were permitted to proliferate for 10 days, forming colonies from single cells. Following, wells were fixed with 4% PFA for 15 min. at room temperature, then washed 3 x 5 min. with PBS. Colonies were stained with 0.1% crystal violet for 1 hr. at room temperature, washed 3 x 5 min. with ddH_2O, air dried, and imaged.

Data Chapter #2

Renal organoid modelling of tuberous sclerosis complex reveals lesion features arise from multiple aberrant developmental processes

Authors: Adam Pietrobon[1,2,3]*, Julien Yockell-Lelièvre[1,3], Trevor Flood[4], William L. Stanford[1,2,3]*

Affiliations:
[1] The Sprott Centre for Stem Cell Research, Regenerative Medicine Program, Ottawa Hospital Research Institute, Ottawa, Canada.
[2] Department of Cellular and Molecular Medicine, University of Ottawa, Ottawa, Canada.
[3] Ottawa Institute of Systems Biology, Ottawa, Canada.
[4] The Ottawa Hospital, Department of Pathology and Laboratory Medicine, Ottawa, Canada.

* Corresponding authors
Adam Pietrobon
The Ottawa Hospital, 501 Smyth Rd, Box 511, CCW 5206c
Ottawa, ON K1H 8L6, Canada

Dr. William L. Stanford, Ph.D.
The Ottawa Hospital, 501 Smyth Rd, Box 511, CCW 5206c
Ottawa, ON K1H 8L6, Canada

Author contributions:
Conceptualization: AP, WLS
Methodology: AP, JY
Investigation: AP, JY, TF
Visualization: AP, JY
Funding acquisition: WLS
Supervision: AP, WLS
Writing – original draft: AP
Writing – review & editing: AP, JY, TF, WLS

Funding:
Canadian Institutes for Health Research (CIHR) grant FRN-153188 (WLS)
CIHR Vanier Canada Graduate Scholarship (AP)
CIHR Tier 1 Canada Research Chair Program in Integrative Stem Cell Biology (WLS)

Running title: TSC renal organoid

Main text word count: 3434

Competing interests: Authors declare that they have no competing interests.

Data and materials availability: Processed data are available in the main text and the supplementary materials. Raw scRNA-seq data are accessible at the GEO repository with accession GSE182632. Additional raw data is available upon reasonable request.

Acknowledgements:
We thank members of Stanford Lab for their continued insights, the Ottawa Hospital Research Institute (OHRI) Stem Core (particularly Kathy Sheikheleslamy and Dr. Pearl Campbell) for assistance in processing scRNA-seq samples, the OHRI Bioinformatics Core (particularly Christopher Porter) for assistance in processing scRNA-seq data, the OHRI Human Pluripotent Stem Cell Core, Anthony Carter and Dr. Chris Kennedy for their assistance with kidney subcapsular transplantations, and the University of Ottawa Cell Biology and Image Acquisition Core (particularly Dr. Chloë Van Oostende-Triplet and Redaet Daniel) for guidance on microscopy and image acquisition.

ABSTRACT

Tuberous sclerosis complex (TSC) is a multisystem tumor-forming disorder caused by loss of *TSC1* or *TSC2*. Renal manifestations predominately include cysts and angiomyolipomas. Despite a well-described monogenic etiology, the cellular pathogenesis has remained elusive. Here, we report a novel genetically-engineered human renal organoid model which recapitulates pleiotropic features of TSC kidney disease *in vitro* and upon orthotopic xenotransplantation. We find that loss of *TSC1/2* affects multiple developmental processes in the renal epithelial, stromal, and glial compartments. First, loss of *TSC1/*2 leads to an expanded stroma by favouring stromal cell fate acquisition and alters terminal stromal cell identity. Second, epithelial cells in the *TSC1/2*$^{-/-}$ organoids exhibit a rapamycin-insensitive epithelial-to-mesenchymal transition. Third, a melanocytic population forms exclusively in *TSC1/2*$^{-/-}$ organoids, branching from MITF^{+} Schwann cell precursors of a *bona fide* neural crest-to-Schwann cell differentiation trajectory. Together, these results illustrate the pleiotropic developmental consequences of biallelic inactivation of *TSC1/2* and offer insight into the pathogenesis of TSC kidney lesions.

MAIN TEXT

Tuberous sclerosis complex (TSC) is a monogenic multisystem disorder characterized by tumor formations in multiple organ systems.[1,2] The genetic etiology is biallelic inactivating mutations in either *TSC1* or *TSC2* (henceforth denoted *TSC1/2*),[3–5] canonically leading to hyperactive mTORC1 signaling.[6] Kidney lesions affect approximately 60-80% of TSC patients[7–10] and are the leading cause of mortality.[11,12] The most common renal lesions are cysts and angiomyolipomas (AMLs), while 2–4% of TSC patients also develop renal cell carcinomas.[13] AMLs are solid masses that contain a varying composition of dysmorphic vasculature, adipose tissue, and smooth muscle-like components.[13,14] Often, patients with TSC will possess multiple renal cysts and AMLs, and the two lesions may co-occur in a phenomenon known as AML with epithelial cysts.[15] TSC renal cysts and AMLs are classically considered disorders of aberrant tissue development that arise from second hit mutations.[16–19]

TSC renal lesion pleiotropy is enigmatic. AMLs are of clonal origin[20,21] and biallelic inactivation of *TSC1/2* is sufficient for pathogenesis,[22–24] yet pathological analyses of the TSC kidney have shown remarkable diversity in lesion morphology, size, cellular composition, and molecular expression.[14,25–30] While between-patient disease expressivity is likely attributable to variable mosaicism,[16–19] the cellular mechanisms underlying within-patient lesion diversity is elusive. Progress has been hindered by the absence of an animal model which fully recapitulates human renal disease.[31] Since *TSC1/2* null embryos die *in utero*,[32,33] attempts at generating knockout animal models have been limited by the *a priori* selection of the temporal and spatial context of mutagenesis. Fortunately, recent advances in organoid technology enables physiologically relevant investigations of otherwise lethal germline homozygous mutations.[34] Pluripotent stem cell-derived renal organoids have been shown to resemble the 1st/2nd trimester

human kidney,[35,36] offering a novel system for studying the developmental consequences of loss of *TSC1/2*.

RESULTS

Engineering of a comprehensive hPSC allelic series to study TSC

We first expanded upon a human pluripotent stem cell (hPSC) allelic series of TSC which contains wild type (WT) and *TSC2*$^{-/-}$ genotypes in four distinct hPSC lines.[37] We engineered *TSC1*$^{-/-}$ mutants in each of the four lines via CRISPR/Cas9, targeting a knockout template to exon 7 of the *TSC1* locus (**Fig. 1A, S1A**). Mutagenesis was confirmed by restriction enzyme digestion and Sanger sequencing (**Fig. S1B-C**). All hPSC genotypes were karyotypically normal, maintained pluripotency in culture, and could differentiate into progeny of all three germ layers (**Fig. 1B, S1D-F**). Loss of *TSC1/2* led to hypomorphic expression of the reciprocal protein product (**Fig. 1C, S1G**). We confirmed that *TSC1/2*$^{-/-}$ mutants failed to downregulate mTORC1 signaling in response to acute hypoxic stress (**Fig. 1D, S1H**). Together, these data validate a comprehensive hPSC allelic series for studying TSC.

TSC1 and *TSC2* are dispensable for renal organoid formation

We next sought to establish a model of TSC kidney disease by adapting a self-organizing renal organoid differentiation protocol (**Fig. 1E, S1I**).[38] We observed that all hPSC genotypes were able to differentiate into epithelialized nephron structures of ~0.5 – 1 mm in diameter (**Fig. S1J**). We note however that all genotypes in two backgrounds (H1 and H7) epithelialized at very low efficiency, thus, the remainder of this worked used only the allelic series in H9 (female embryonic stem cell line) and 168 1d2 (male induced pluripotent stem cell line) cells.

Epithelialized structures expressed markers of podocytes (NPHS1), proximal tubules (LRP2), and distal tubules (CDH1) in a segmental and spatial arrangement that resembles human nephron patterning (**Fig. 1F**). Differentiation efficiency across genotypes was comparable, with a slight reduction in bulk LRP2 expression in *TSC1/2*$^{-/-}$ organoids (**Fig. S1K**). Together, these data demonstrate that hPSCs can differentiate into primitive renal lineages in the absence of *TSC1/2*.

Temporal single cell RNA-seq (scRNA-seq) reveals stromal, nephron, and neural-glial differentiation trajectories

To comprehensively study the consequence of *TSC1/2* ablation in renal organoid differentiation, we performed temporal scRNA-seq via MULTI-seq sample preparation.[39] We analyzed all three genotypes in two cell lines across four timepoints, generating data on 27,808 cells split between 24 samples (**Fig. 1G**). We observed that cells from each genotype were present throughout the Uniform Manifold Approximation and Projection (UMAP) containing all samples (**Fig. 1H**). Early timepoint cells were grouped together in the UMAP center, while later timepoints radiated outwards, indicating greater transcriptional diversity with increased differentiation time (**Fig 1I**).

We next clustered cells and identified marker genes highly expressed in each cluster (**Fig. S1L-M**, **Table S1**). To annotate cell types, we overlapped cluster marker genes with marker genes reported in four distinct scRNA-seq datasets of the mouse and human fetal kidney (**Table S2**).[40–43] This analysis identified three major cell fates in our renal organoid differentiation, including stromal, nephron (epithelial), and neural-glial, as well as a very small population of endothelial cells (**Fig. 1J**). Early timepoint cells in the UMAP center did not express distinguishing cell identity markers, so we annotated this population as “Unspecified

progenitors." Together, these data demonstrate three major cell populations form during renal organoid differentiation; we rely on this dataset in subsequent sections to study the effects of *TSC1/2* ablation on renal development.

TSC1/2$^{-/-}$ renal organoids exhibit molecular features of AMLs

Melanocytic genes, including *PMEL* and *MLANA*, are pathognomonic markers of AMLs.[28] At differentiation endpoint (day 21), these genes were near uniquely expressed in *TSC1/2*$^{-/-}$ organoids compared to WT, with the highest expression in *TSC2*$^{-/-}$ and intermediate in *TSC1*$^{-/-}$ (**Fig. 2A-B, S2A-B**). In contrast, *VIM*, a mesenchymal gene expressed in AMLs,[25] was transcriptionally expressed in all genotypes yet uniquely expressed at high protein levels in *TSC1/2* organoids (**Fig. 2C-E, S1C-D**). To more comprehensively appraise AML feature expression, we analyzed a list of genes reported to be upregulated in primary human AMLs compared to normal kidney.[23] Globally, we observed the highest expression of these genes in *TSC2*$^{-/-}$ organoids, followed by *TSC1*$^{-/-}$ (**Fig. 2F**). Together, these data demonstrate *TSC1/2*$^{-/-}$ renal organoids exhibit a molecular profile reminiscent of primary human AMLs.

TSC2 ablation induces greater transcriptomic aberrations compared to loss of *TSC1*

Increased expression of AML marker genes in *TSC2*$^{-/-}$ organoids compared to *TSC1*$^{-/-}$ led us to ask whether disruption of *TSC2* causes greater transcriptomic aberrations compared to *TSC1*. To answer this question, we performed differential gene expression analysis between WT and *TSC1/2*$^{-/-}$ cells globally, within general clusters, and within specific clusters (**Table S3**). Globally, we observed more differentially expressed genes (DEGs) upon *TSC2* loss in comparison to loss of *TSC1*, with overlapping genes exhibiting a greater effect size in *TSC2*$^{-/-}$

organoids (**Fig. 2G-H**). Similar observations were made when analyzing DEGs across genotypes within general and specific clusters (**Table S3**). Global DEGs that followed the expression pattern of WT < *TSC1*$^{-/-}$ < *TSC2*$^{-/-}$ included those associated with cholesterol transport (*APOE, NPC2*), antigen presentation (*B2M*), and iron transport (*FTL, FTH1*) (**Fig. S2E**). GO term enrichment analysis of all genes significantly upregulated by both *TSC1/2*$^{-/-}$ organoids revealed a network of metabolic-associated terms (**Fig. S2F**). Together, these data demonstrate conserved transcriptomic changes upon ablation of *TSC1* or *TSC2*, but the extent and magnitude of changes are further potentiated in the *TSC2*$^{-/-}$ setting.

AML-like lesions form upon orthotopic xenotransplantation of *TSC1/2*$^{-/-}$ renal organoids

While our *TSC1/2*$^{-/-}$ renal organoids exhibited molecular features of AMLs, we did not observe the classic triphasic AML histology. We speculated that niche-specific cues are required to differentiate *TSC1/2*$^{-/-}$ renal organoids into AML constituents. To test this hypothesis, we orthotopically xenotransplanted WT, *TSC1*$^{-/-}$, and *TSC2*$^{-/-}$ renal organoids under the kidney capsule of immunodeficient mice (**Fig. S2G**). Harvesting 12 weeks later, we observed successful engraftment of all three genotypes (**Fig. S2H**). Histological analysis revealed basophilic tubular structures, as previously reported in WT renal organoid transplants (**Fig. S2I**).[44] Uniquely in the *TSC1/2*$^{-/-}$ transplants, we identified well-demarcated vascularized lesions with associated smooth muscle and lipomatous components, which strikingly resemble human AML (**Fig. 2I**). We observed human-specific XRCC5 staining in all parts of the lesion, proving the vascular, smooth muscle, and adipose tissue elements arise cell autonomously (**Fig. 2J**). Together, these data indicate *TSC1/2*$^{-/-}$ renal organoids contain progenitor populations which can form AML-like lesions *in vivo*.

130

131 ***TSC1/2*$^{-/-}$ renal organoids confer both cell autonomous and non-autonomous cystogenesis**

132 During renal organoid differentiation, we observed ~20% of epithelialized structures in
133 the *TSC1/2*$^{-/-}$ cultures formed cysts that grew to ~0.5 mm in diameter (**Fig. 3A-B, S3A-B**). The
134 cyst epithelium was cuboidal and CDH1^{+}/LRP2^{+}, suggesting a mature proximal tubule cell
135 identity (**Fig. 3C**). Interestingly, LRP2 was expressed on the basolateral rather than apical
136 surface. Cysts formed as early as day 16 of differentiation exclusively from epithelialized
137 structures, yet began to regress following day 21. We tested whether cysts would continue to
138 expand long-term if detached from the culture stratum, as previously described in a polycystic
139 kidney disease model;[45] however, cysts still regressed shortly after detachment (**Fig. S3C**).

140 We next examined whether rapamycin treatment could prevent the onset of cystogenesis.
141 We observed nephron epithelialization could proceed in the presence of rapamycin, albeit at
142 statistically insignificant reduced efficiencies (**Fig. S3D-E**). We confirmed reduction in a S6RP
143 rapamycin-sensitive phosphorylation site in epithelialized segments, although loss of
144 pS6RP$^{Ser235/236}$ was not achieved in all cells of the bulk culture (**Fig. 3D, S3F**). Remarkably, we
145 observed near complete rescue of cystogenesis in *TSC1/2*$^{-/-}$ renal organoids, indicating cell
146 autonomous cyst formation is rapamycin-sensitive. (**Fig. 3E**).

147 In addition to AML-like lesions, we also observed that large cysts formed in *TSC1/2*$^{-/-}$
148 xenotransplants, sometimes in association with AMLs (**Fig. 3F, S3G)**. These cysts were
149 proliferative and expressed CDH1 but not LRP2 (**Fig. 3G**). In contrast to AML-like lesions, the
150 cystic epithelium was not XRCC5^{+}, indicating cell non-autonomous cystogenesis conferred by
151 *TSC1/2*$^{-/-}$ xenotransplanted cells. Together, these data demonstrate *TSC1/2*$^{-/-}$ renal organoids
152 form cell autonomous and non-autonomous cysts that are histologically distinct.

153

154 **Loss of *TSC1/2* results in an expanded stroma by favouring stromal cell fate acquisition**

155 We next further interrogated our scRNA-seq dataset to untangle mechanisms of
156 pathogenesis. We were intrigued by the finding that AML marker genes are expressed in WT
157 renal organoid cells, albeit at lower levels compared to *TSC1/2*$^{-/-}$ (**Fig. 2F**). Stratifying WT cells
158 by cluster, we observed that these genes are upregulated in the stromal compartment, while genes
159 downregulated in AMLs were enriched in renal epithelial cells (**Fig. 4A, S4A**). As these data
160 suggest AMLs resemble stromal cells during development, we examined how loss of *TSC1/2*
161 affects the stromal differentiation trajectory. We found a higher proportion of stromal cells in
162 *TSC1/2*$^{-/-}$ organoids compared to WT (**Fig. 4B**). This observation was not exclusively attributable
163 to increased proliferation (**Fig. 4C, S4B**). However, *TSC1/2*$^{-/-}$ renal organoids upregulated
164 stromal marker genes early in the progenitor cluster, a pattern not observed with nephron or
165 neural-glial marker genes (**Fig. 4D, Fig. S4C-D**).

166

167 **Stromal cell identity diverges in *TSC1/2*$^{-/-}$ renal organoids**

168 We observed that genotype proportions in a subset of stromal clusters varied widely (**Fig.**
169 **S4E**). Compositional analysis indicated the greatest variation between WT and *TSC1/2*$^{-/-}$
170 organoids occurred in the stromal compartment at later timepoints (**Fig. 4E**). Interestingly,
171 stromal cell fates appeared much more plastic, as trajectory inference fit a network with loops
172 and many branches and upregulated marker genes of stromal compartments were in fact shared
173 across clusters (**Fig. 4F**, **Fig. S4F**). We subsetted and re-analyzed day 21 stromal cells and
174 observed cells partitioned by genotype (**Fig. 4G**). Together, these data suggest that *TSC1/2*
175 ablation favours stromal cell fate acquisition and alters terminal cell identity (**Fig. 4H**).

Loss of *TSC1/2* causes a rapamycin insensitive epithelial-to-mesenchymal transition

We next sought to determine the pathogenesis of VIM^{high} cells identified in *TSC1/2*$^{-/-}$ organoids (**Fig 2E**). We observed VIM^{high} cells arise directly from $NPHS1^{+}$ and $CDH1^{+}$ cells following epithelialization (**Fig. 5A-B**). VIM^{high} formation was correlated with efficiency of epithelialization (**Fig. S5A**). Epithelial cells lost CDH1 expression and acquired a mesenchymal morphology as they became VIM^{high} (**Fig. 5A**), suggesting an epithelial-to-mesenchymal (EMT).

We further interrogated the organoid nephron branch by subsetting cells, computing a new UMAP, and annotating clusters based on known markers (**Fig. 5C, S5B-D, Table S4-S5**). Phylogenetic analysis indicated cluster relationships that roughly resemble physiological development, notwithstanding the presence of a cluster enriched in *TSC1/2* cells which we failed to annotate (**Fig. S5E-F**). We examined *VIM* and *CDH1* transcript expression in the podocyte, loop of Henle/distal tubule, and proximal tubule clusters and did not observe clear changes across genotypes that mirrored protein-level data (**Fig. 5D**). We analyzed expression of a larger panel of epithelial and mesenchymal genes and did not observe EMT-like changes in the *TSC1/2*$^{-/-}$ cells (**Fig. S5G**), suggesting EMT may not initially be reflected at the transcript-level.

We queried whether hyperactive mTORC1 signaling is driving the EMT. Prior to EMT, we observed p4E-$BP1^{Thr37/46}$ to be expressed in all nephron cells equivalently across genotypes (**Fig. S5H**). In contrast, $pS6RP^{Ser235/236}$ was expressed in scattered $CDH1^{+}$ tubular cells but largely absent from $NPHS1^{+}$ podocytes; however, this pattern was shared across genotypes (**Fig. S5H**). Thus, hyperphosphorylation of $pS6RP^{Ser235/236}$ in *TSC1/2*$^{-/-}$ renal tubular cells did not proceed EMT *per se*. Finally, we treated cultures with rapamycin prior to EMT and did not

observe any rescue in VIM^{high} formation (**Fig. 5E, S5I**). Together, these data indicate *TSC1/2* ablation induces a rapamycin insensitive EMT (**Fig. 5F**).

PMEL expression does not partition with a single cell identity

PMEL is a pathognomonic marker of AMLs and is generally considered a marker of physiological melanocytes. While PMEL is near exclusively expressed in *TSC1/2*$^{-/-}$ renal organoids at day 21 (**Fig. 2B**), WT cells expressed PMEL throughout differentiation (**Fig. 6A, S6A**). $PMEL^{+}$ cells arose in multiple lineages distinct from epithelialized segments but were often localized to regions adjacent to $CDH1^{+}$ cells (**Fig. 6A-C**). PMEL expression rose and fell upon treatment and withdrawal of CHIR-99021, a GSK3β inhibitor, corresponding to a high and low fraction of $pS6RP^{Ser235/236+}$ cells; however, elevated $pS6RP^{Ser235/236}$ alone was not sufficient to confer PMEL expression (**Fig. S6B**). Treatment with rapamycin during differentiation led to a repression of the percentage of $PMEL^{+}$ cells in *TSC1/2*$^{-/-}$ organoids to WT levels (**Fig. 6D**), together suggesting mTORC1 activity is necessary but not sufficient to induce PMEL expression.

A melanocytic population predominately composed of *TSC1/2* cells arise in the glial cluster

As we concluded $PMEL^{+}$ is not attributable to a single cell identity, we looked for co-expression of multiple AML melanocytic markers. We observed that cells in the glial cluster expressed *MITF*, *PMEL*, and *MLANA* (**Fig. 6E**). We subsetted this branch and recalculated the UMAP (**Fig. 6F**). Unsupervised clustering identified a population of cells enriched in melanocytic markers that branched from the linear differentiation pattern (**Fig. 6G-H, Table S6**). Remarkably, the cluster was almost exclusively composed of *TSC1/2*$^{-/-}$ cells. (**Fig. 6I**).

The glial cell cluster is a *bona fide* neural crest to Schwann cell differentiation trajectory

Expression of melanocytic AML markers motivated us to more thoroughly investigate the cell identity of the glial cluster. To do so, we fit a trajectory and analyzed differential gene expression across pseudotime (**Fig. S6C**), identifying 2,008 DEGs which varied throughout differentiation (**Fig. S6D**, **Table S7**). We noted a suite of genes (e.g. *PLP1*, *S100B*, and *CDH19*) expressed at trajectory endpoint which are markers of Schwann cells (glia of the peripheral nervous system). Schwann cells are classically described to develop from Schwan cell precursors (SCPs), a progeny of neural crest cells (NCCs) (**Fig. 6J**).[46] Analyzing hallmark markers of these three lineages, we observed temporal expression patterns that mimic a canonical Schwann cell differentiation trajectory (**Fig. 6K**)

To appraise neural crest cell identity more comprehensively, we relied on a scRNA-seq dataset of mouse neural crest cells.[47] We noted 49% of neural crest marker genes were contained in our trajectory DEG list (**Fig. S6E**). Temporal expression of these genes followed a pattern that largely mirrors the stages of neural crest development (**Fig. 6L-M, S6F**). Together, these data confirm the glial cluster is composed of a *bona fide* NCC-SCP-SC differentiation trajectory.

Loss *TSC1/2* induces a melanocytic differentiation branch from MITF^{+} Schwann cell precursors

We next sought to elucidate the aberrant cell fate decision that results in formation of the melanocytic population. We observed greater differences across genotype with genes expressed at later pseudotime, indicating progressive cell fate divergence (**Fig. S6G, Table S8**). Melanocytic cells formed around pseudotime 5 – 15, the time during SCP gene activation (**Fig.**

6K, N). Analysis of genes that were differentially expressed between genotype and expressed within this window identified the melanocytic transcription factor *MITF* previously implicated in TSC (**Fig. 6O, Table S8**).[48]

We found that *MITF* was expressed in all genotypes but remained high exclusively in *TSC1/2*$^{-/-}$ cells (**Fig. 6P**). Significant genotypic divergence in *MITF* expression co-occurred with other transcriptomic targets of MITF such as PMEL and ASAH1 (**Fig. 6P**), as well as *DDIT4*, a negative regulator of mTORC1 signaling (**Fig. S6H**). *MITF* was expressed in SCPs and lost upon Schwann cell differentiation; however, in the *TSC1/2*$^{-/-}$ organoids, *MITF* expression remained high in the branching melanocytic population (**Fig. 6Q**). The *MITF*$^{+}$ melanocytic population exhibited robust expression of multiple MITF target genes (**Fig. 6R**).[49] This aberrant melanocytic branching co-occurred with a delayed SCP gene activation, as well as blunted but not blocked Schwann cell fate acquisition (**Fig. 6Q, S6I-J**). Interestingly, *MITF*$^{+}$ melanocytic cells still retained glial marker expression (**Fig. S6K**). Together, these data demonstrate loss of *TSC1/2* induces *MITF*$^{+}$ melanocytic cell fate acquisition, branching from the *MITF*$^{+}$ SCP population (**Fig. 6S**).

DISCUSSION

The cell of origin of TSC cysts and RAMLs has been in question for decades, with numerous suspects proposed.[50–54] Here, we demonstrate *TSC1/2* ablation alters multiple developmental trajectories to confer pleiotropic features of TSC kidney disease. Thus, TSC renal cysts and AMLs may arise from multiple cells of origin, with disease heterogeneity a reflection of the diverse progenitor populations acquiring second hit mutations during development. While our data cannot exclude the possibility of somatic mutagenesis as the disease etiology,[52,55] such a

mechanism is not mutually exclusive and may very well may co-exist with developmental aberrations.

Our analyses demonstrate AML markers are upregulated in developmental stromal cells (**Fig. 2F**), supporting previous findings that AMLs resemble the embryonic kidney.[23] *TSC1/2*$^{-/-}$ cells favouring a stromal fate (**Fig. 4D**) offers explanation for how AMLs can form in regions outside the kidney.[56,57] While parenchymal tissue constituents (i.e. epithelial cell types) vary between organs, similar stromal cell types can be found in different organ systems.[58] Thus, spatially distinct AMLs may partly arise from *TSC1/2*$^{-/-}$ favouring acquisition of stromal cell fates that are resident identities of each organ.

The metanephric kidney is classically described to arise from the intermediate mesoderm during development; [59,60] however, the paraxial mesoderm and neural crest lineages contribute to non-epithelial populations.[61,62] Previous studies using renal organoids have reported the existence of neuronal, trunk mesenchymal, and melanocytic clusters.[63–66] Although these populations were described as "off-targets," these cell types are all progeny of NCCs. Our data provide evidence of neural crest differentiation during renal organoid differentiation, which may indeed bear physiological relevance and not a technical limitation of *in vitro* manipulation.

The observation of *TSC1/2*$^{-/-}$ enforcing a melanocytic cell fate branch from SCPs **(Fig. 6)** is remarkable, considering the longstanding hypothesis that NCCs are the cell of origin for mesenchymal TSC lesions.[53] Interestingly, cells expressing the SCP marker gene *Mpz* promoter (transiently or permanently) contribute to *Tsc2*$^{+/-}$ mice renal lesion bulk.[67] However, the taxonomic distinction of SCPs from NCCs is blurred; SCPs possess multipotency and can produce melanocytic progeny.[46,68] Our data suggest *TSC1/2* (and perhaps mTORC1) may be critical factors in determining the cell fate decisions of SCPs. Enforced acquisition of a

melanocytic identity by loss of *TSC1/2* may very well explain the etiology of melanocytic markers expressed in mesenchymal TSC lesions.[57] Interestingly, loss of *TSC1/2* in primary melanocytes has been shown to induce *MITF* downregulation and hypopigmentation.[69] As the melanocytic population formed in our organoids retained glial features (**Fig. S6K**), we suspect *TSC1/2*$^{-/-}$ cells are acquiring a cell fate that is an aberrant hybrid between Schwann and melanocytic identity.

While *TSC1/2* were dispensable for renal epithelia formation (**Fig. 1F**), *TSC1/2*$^{-/-}$ cells could not maintain an epithelial identity and underwent EMT (**Fig. 5A**), corroborating findings from several conditional knockout mouse models.[70–73] This cell identity reversion may explain why cell autonomous cysts that formed *in vitro* (which preceded EMT) did not persist (**Fig. 3A**), with *in vivo* cell non-autonomous cytogenesis complementing data in primary TSC lesions and mouse models.[74–77] Acquisition of VIM^{high} cell fate was insensitive to rapamycin treatment, a finding of clinical significance since patient lesions respond incompletely to rapamycin therapy.[78,79] We hypothesize variable clinical responses may arise from heterogeneity in lesion composition, with some constituents possessing rapamycin insensitivity.

In conclusion, we report a novel genetically engineered human renal organoid model which recapitulates features of TSC kidney disease *in vitro* and upon orthotopic xenotransplantation. We find that loss of *TSC1/2* affects multiple developmental processes in the renal epithelial, stromal, and glial compartments. These data illustrate the pleiotropic developmental consequences of biallelic inactivation of *TSC1/2* and offer insight into the pathogenesis of TSC kidney lesions.

METHODS

Study design

The objective of this research was to investigate the consequence of *TSC1/2*$^{-/-}$ mutagenesis on renal development and identify pathogenic mechanisms that confer features of TSC kidney disease. We first expanded on a hPSC allelic series of TSC[37] by knocking out *TSC1* in all four lines with CRISPR/Cas9. These cell lines were subjected to a renal organoid differentiation protocol[38] and analyzed using a variety of methods both *in vitro* and *in vivo* (described subsequently). Of note, most assays employed involved temporal analyses- including time course scRNA-seq, flow cytometry, and RT-qPCR- thereby unravelling etiological mechanisms. Wherever possible, samples were blinded to analysis by coding with a unique identifier.

Sample sizes for both *in vitro* and *in vivo* studies were determined according to field-specific conventions. Power analysis was not employed. All data points were included in the data presentation; outliers were only excluded if there was definitive empirical evidence of technical error. Experiments were repeated three or more times unless otherwise noted, with replicates collected under independent conditions. Raw scRNA-seq data is accessible at the Gene Expression Omnibus (GEO) repository with accession GSE182632.

Statistical analysis

All figures are presented with individual data points (where graphically appropriate), with measures of central tendency and error to be mean and standard deviation, respectively, unless otherwise stated. Sample number and statistical tests employed are reported in the figure legends.

All statistical tests were two-sided and significance (*) was attributed when $p < 0.05$. Outliers were not excluded from the calculation unless otherwise stated.

Study reagents and resources

Please see below (**Table 1**) for a list of key reagents and resources used in this study.

Table 1: List of key reagents and resources used in this study.

REAGENTS and RESOURCES	SOURCE	IDENTIFIER
Antibodies		
TSC1	CST	4906
TSC2	CST	4308
ACTB	CST	370
pS6RP (Ser 235/236)	CST	2211
S6RP	CST	2317
p4E-BP1 (Ser65)	CST	9451
p4E-BP1(Thr 37/46)	CST	2855
4E-BP1	Thermo Fisher Scientific	AHO1382
pS6K1 (Thr 389)	CST	9206
S6K1	CST	2708
HIF1A	R&D Systems	MAB1536
CDH1	Thermo Fisher Scientific	13-1700
CDH1	CST	3195
LRP2	Novus Biologicals	NB110-96417
NPHS1	PROGEN	GP-N2
PMEL	Thermo Fisher Scientific	MA5-13232
MLANA	Thermo Fisher Scientific	MA5-15-237
VIM	CST	3932
ACTA2	Abcam	ab5694
XRCC5 (Ku80)	CST	2180
PCNA	Thermo Fisher Scientific	13-3900
HRP-conjugated Goat anti-Rabbit IgG (H+L)	Thermo Fisher Scientific	G-21234
HRP-conjugated Goat anti-Mouse IgG (H+L)	Thermo Fisher Scientific	G-21040
AlexaFluor 405 Goat Anti-Mouse IgG (H+L)	Thermo Fisher Scientific	A31553
AlexaFluor 488 Goat Anti-Rabbit IgG (H+L)	Thermo Fisher Scientific	A11034
AlexaFluor 488 Goat Anti-Mouse IgG (H+L)	Thermo Fisher Scientific	A11001
AlexaFluor 555 Goat Anti-Rabbit IgG (H+L)	Thermo Fisher Scientific	A21428
AlexaFluor 555 Goat Anti-Mouse IgG (H+L)	Thermo Fisher Scientific	A32727
AlexaFluor 555 Goat Anti-Guinea pig IgG (H+L)	Thermo Fisher Scientific	A21435
AlexaFluor 647 Goat Anti-Rabbit IgG (H+L)	Thermo Fisher Scientific	A21245
AlexaFluor 647 Goat Anti-Mouse IgG (H+L)	Thermo Fisher Scientific	A21235
AlexaFluor 680 Goat Anti-Rabbit IgG (H+L)	Thermo Fisher Scientific	A21076
AlexaFluor 680 Goat Anti-Mouse IgG (H+L)	Thermo Fisher Scientific	A28183
DyLight 800 Goat Anti-Rabbit IgG (H+L)	Thermo Fisher Scientific	SA535571
DyLight 800 Goat Anti-Mouse IgG (H+L)	Thermo Fisher Scientific	SA535521

Small molecules		
Hoechst 33342	Thermo Fisher Scientific	H3570
CHIR-99021	AdooQ Bioscience	A10199
Rapamycin	MilliporeSigma	553211
Y-27632	AdooQ Bioscience	A11001
Cell culture reagents		
Essential 8	Prepared in house	N/A
Matrigel	Corning	354230
Lipofectamine Stem Transfection Reagent	Thermo Fisher Scientific	STEM00001
B-27 Supplement	Thermo Fisher Scientific	17504044
Advanced RPMI	Thermo Fisher Scientific	12633020
Accutase	Stem Cell Technologies	7920
Commercial kits and materials		
BOLT 4-12% 1 mm, 10-well gel	Thermo Fisher Scientific	NW04120BOX
NucleoSpin® RNA 740955.250 D-Mark Bio	Machery-Nagel	740955.250
SupersScript II	Thermo Fisher Scientific	18064014
SYBR Green I Master	Roche	04707516001
ReadyProbes™ Mouse-on-Mouse IgG Blocking Solution	Thermo Fisher Scientific	R37621
Pierce™ BCA Protein Assay Kit	Thermo Fisher Scientific	23225
Cell models		
H9 human embryonic stem cell, WT	WiCell	WB67614
H7 human embryonic stem cell, WT	WiCell	FTDL-03
H1 human embryonic stem cell, WT	WiCell	WB34445
168 1d2 induced pluripotent stem cell, WT	Generated in house[80]	N/A
H9 *TSC2*$^{-/-}$	Generated in house[37]	N/A
H7 *TSC2*$^{-/-}$	Generated in house[37]	N/A
H1 *TSC2*$^{-/-}$	Generated in house[37]	N/A
168 1d2 *TSC2*$^{-/-}$	Generated in house[37]	N/A
H9 *TSC1*$^{-/-}$	Generated in house	N/A
H7 *TSC1*$^{-/-}$	Generated in house	N/A
H1 *TSC1*$^{-/-}$	Generated in house	N/A
168 1d2 *TSC1*$^{-/-}$	Generated in house	N/A
Animal models		
NOD.Cg-*Prkdc*^{scid} *Il2rg*^{tm1Wjl}/SzJ (NSG)	Jackson Laboratory	005557
Software and algorithms		
ImageJ 1.53c	ImageJ	N/A
R 4.0.5	R	N/A
RStudio 1.3.1093	RStudio	N/A

Pluripotent stem cell culture

hPSCs were maintained on plates coated with a thin layer of Matrigel at 37ºC, 10% CO_2. Cells were fed with Essential 8 media, prepared in house. Cells were passaged by incubation

with 500 μM EDTA for 3 min., then cell scraping and transfer to a new pre-coated plate by wide-bore pipette.

Gene editing and validation

We targeted exon 7 of *TSC1* as it is one of the most proximal exons occurring in all reported isoforms (**Fig. 1A, S1A**). hPSCs were dissociated into single cells by Accutase treatment for 15 min at 37ºC. Cells were harvested, washed, and seeded on plates coated with Matrigel. The following day, we used Lipofectamine Stem Reagent to transfect hPSCs with a plasmid (containing *Cas9* and an sgRNA targeting exon 7) and a double stranded repair template (containing stop codons in all three reading frames and a *PmeI* restriction site).

Cells were allowed to expand for 1-2 weeks and individual colonies picked for screening by restriction enzyme digestion. Colonies exhibiting fragment digestion were subjected to another round of clonal isolation and expansion to guarantee a pure population. Mutagenesis was assessed by Sanger sequencing (service provided by the Ottawa Hospital Research Institute Stem Core). hPSC karyotypes were assessed by chromosome spread (service provided by WiCell). Protein expression knockout was assessed by western blot (described subsequently).

Renal organoid differentiation

Renal organoids were generated following a previously reported differentiation protocol (**Fig. S1I**).[38] Briefly, hPSCs are single cell seeded onto a thick layer of Matrigel, then encapsulated in a second thick layer of Matrigel to form spheroids which resemble the human epiblast. The primitive streak is then induced by CHIR-99021 treatment (GSK3β inhibition), followed by continuous media changes with Advanced RPMI + B-27 supplement. Nephron-like

366 structures form spontaneously without any additional mechanical manipulation, making this a
367 "self-organizing" protocol.
368 For each cell line, we optimized epithelialization efficiency by modulating two key
369 parameters: cell seeding density and CHIR-99021 concentration. Optimal parameters for the four
370 lines included: H9 (5,715 cells/cm^2 and 18 μM), H7 (10,500 cells/cm^2 and 10 μM), H1 (3,500
371 cells/cm^2 and 8 μM), and 168 1d2 (8,000 cells/cm^2 and 16 μM). We note however that all
372 genotypes in two backgrounds (H1s and H7s) epithelialized at very low efficiency, thus, the bulk
373 of this work used only the allelic series in H9s (female embryonic stem cell line) and 168 1d2s
374 (male induced pluripotent stem cell line).
375
376 **Cyst quantification and detachment**
377 We defined cysts in adherent cultures as large, balloon-like, translucent structures that
378 swayed in response to agitation, as previously described.[45] We counted both cysts and the total
379 number of discrete epithelialized structures in each organoid well to calculate cytogenesis
380 frequency. At day 21 of differentiation, cysts were detached from the culture stratum using a 25-
381 guage needle under an inverted phase-contrast stereoscope. Cysts were carefully transferred by
382 wide-bore pipette to a culture plate coated with 1% agarose. Media was changed every 2-3 days
383 while cyst growth was tracked temporally by DIC microscopy with an AxioObserver A1 (Zeiss).
384
385 **Western blot**
386 Wells were washed x2 with cold PBS and harvested in RiPA buffer containing total
387 protease and phosphatase inhibitors. We quantified total protein by BCA assay and prepared
388 samples at 10 μg/lane by resuspending in Laemmli buffer and heating for 10 min. at 70°C. Total

protein samples were separated by SDS-PAGE using a BOLT 4-12% 1 mm 10-well gel and MES running buffer. We transferred samples onto a 0.45 µm PVDF membrane overnight at 4ºC by wet transfer with Towbin buffer (containing 0.025% SDS and 10% MeOH). The membrane was blocked with 5% BSA in PBS-T (0.1% Tween-20) for 1 hr. at room temperature. Following, the membrane was incubated overnight at 4ºC in primary antibodies diluted in blocking buffer at the following concentrations: TSC1 (1:1000), TSC2 (1:5000), ACTB (1:5000), pS6RP$^{Ser235/236}$ (1:5000), S6RP (1:500), p4E-BP1^{Ser65} (1:1000), 4E-BP1 (1:1000), pS6K1^{Thr389} (1:500), S6K1 (1:1000), and HIF1A (1:500). The membrane was washed 3 x 5 min. with PBS-T, and then incubated for 1 hr. at room temperature in fluorescent secondary antibodies diluted 1:10,000 in blocking buffer. The membrane was washed again 3 x 5 min. with PBS-T and then imaged using Odyssey Gel Imager (LI-COR Biosciences). Samples were analyzed in ImageJ by quantifying signal intensity, normalizing by unphosphorylated protein or ACTB, and scaling between 0 to 1.

RT-qPCR

Culture media was aspirated from wells and cells were immediately lysed with RNA extraction buffer from the NucleoSpin Kit. RNA samples were prepared following manufacturer instructions with a DNaseI digestion included. Samples quality was assessed by Nanodrop, and only samples with A260/A280 of 1.8-2.3 and A260/230 > 2 were used. We reverse-transcribed 1 µg of total RNA from each sample via SuperScript II with oligoDT priming following manufacturer instructions. qPCR was performed using SYBR Green I and analysis on LightCycler® 480 Instrument II (Roche). The sequence of primers used are listed in **Table 2**. We validated each primer by ensuring a single product of the predicted fragment length. The efficiency of each primer was determined by a standard curve, and suitability of reference genes

across sample sets was assess using variance stability calculations. We quantified normalized gene expression by scaling C_q by primer efficiency, dividing by the geometric mean of reference gene values (ACTB and GAPDH), and normalizing by the within-group average value.

Table 2: List of primer sequences for RT-qPCR.

TARGET	PRIMER SEQUENCE
ACTB	Forward: AGACCTGTACGCCAACACAG Reverse: CGCTCAGGAGGAGCAATGAT
GAPDH	Forward: AAAATCAAGTGGGGCGATGC Reverse: CAGGAGGCATTGCTGATGAT
SOX2	Forward: TACAGCATGTCCTACTCGCAG Reverse: GAGGAAGAGGTAACCACAGGG
OCT4	Forward: TCAGCCAAACGACCATCTGCCG Reverse: AGCAAGGGCCGCAGCTTACA
NANOG	Forward: ACGCAGAAGGCCTCAGCACCTA Reverse: AGGTTCCCAGTCGGGTTCACCA
CDH1	Forward: AGGGGTTAAGCACAACAGCA Reverse: CCTGACCCTTGTACGTGGTG
CUBN	Forward: AGAATAGCTTCGTGAAGGTGTGG Reverse: CCTCCTGAGACTGGAAGACG
NPHS1	Forward: CAACTTGTCAGCATCAGCCG Reverse: CAGCAGCCAGACCCTGTATC

Flow cytometry

Renal organoids were dissociated into single cells by Accutase treatment for 15 min. at 37ºC followed by x3 trituration with a 25-guage needle. Samples were then washed and fixed with 4% paraformaldehyde for 15 min. at room temperature. Fixing solution was diluted out 1/100 in PBS, cells were pelleted by centrifugation, and supernatant discarded. Fixed single cell suspensions were permeabilized with 0.1% Triton-X in blocking solution (PBS with 0.1% Tween-20, 1% BSA, and 10% goat serum) for 20 min. at room temperature. Permeabilizing solution was diluted out 1/100 in PBS, cells were pelleted by centrifugation, and supernatant discarded. Samples were then blocked for 1 hr. Cells were pelleted by centrifugation, supernatant discarded, and primary antibodies diluted in blocking solution were added for an overnight incubation at 4ºC. The following concentrations of antibodies were employed: $pS6RP^{Ser\ 235/236}$ (1:200), CDH1 (1:200), NPHS1 (1:200), PMEL (1:100), and VIM (1:200). The next day,

primary antibody solution was diluted out 1/100 in PBS, cells were pelleted by centrifugation, and supernatant discarded. Samples were then incubated with fluorescent secondary antibodies diluted in blocking solution for 1 hr. at room temperature. All fluorescent secondary antibodies were used as a 1:1000 dilution. Secondary antibody solution was diluted out 1/100 in PBS, cells were pelleted by centrifugation, and supernatant discarded. Samples were next counterstained with 10 μg/mL Hoechst 33342 for 20 min. at room temperature. Hoechst 33342 solution was diluted out 1/100 in PBS, cells were pelleted by centrifugation, and supernatant discarded. Finally, cells were strained and analyzed using the LSRFortessa (BD) flow cytometer.

Whole mount immunofluorescence staining

Renal organoids were fixed with equal media volumes of 8% PFA for 45 min. at room temperature. Wells were washed 5 x 15 min. with PBS, permeabilized with 0.1% Triton-X in blocking solution (PBS with 0.1% Tween-20, 1% BSA, and 10% goat serum) for 4 hrs. at room temperature, then washed 3 x 30 min. with blocking solution. Note for MLANA, Tween and Triton-X were omitted and replaced with 0.05% saponin for permeabilization. We then added primary antibodies diluted in blocking solution for an overnight incubation at 4°C. The following concentrations of antibodies were employed: pS6RP$^{Ser\ 235/236}$ (1:100), p4E-BP1$^{Thr\ 37/46}$ (1:200), CDH1 (1:200), LRP2 (1:100), NPHS1 (1:100), PMEL (1:50), MLANA (1:50), and VIM (1:200). The next day, wells were washed with blocking solution x3 over an 8 hr. period, then incubated with fluorescent secondary antibodies diluted blocking solution (1:400) overnight at 4°C. The next day, wells were washed with blocking solution x3 over an 8 hr. period, then counterstained overnight at 4°C with 20 μg/mL Hoechst 33342. Wells were washed a final time (x3 over 8 hr.

period) and mounted with a 90% glycerol solution made in house. Samples were imaged using an LSM800 (Zeiss) confocal microscope.

Immunohistochemistry

Fixed specimens in 70% EtOH were dehydrated through a series of increasing EtOH concentrations, followed by xylene, and then finally embedded in paraffin. Samples were sectioned at 5 μm using a microtome and placed on ultra-adhesive slides. Paraffin sections were dissolved by incubation in xylene and subsequently rehydrated via decreasing concentrations of EtOH in water. Heat-induced antigen retrieval was performed by incubating specimens in a pressure cooker at 12 psi for 10 min. Depending on the antigen, samples were bathed in either sodium citrate, pH 6, or Tris-EDITA, pH 9, both with 0.1% Tween-20. After cooling to room temperature, samples were blocked in blocking solution (PBS with 0.1% Tween-20, 1% BSA, and 10% goat serum) for 1 hr. at room temperature. If the primary antibody was raised in mouse, we performed a second 1 hr. incubation in polyclonal mouse IgG (ReadyProbes Mouse-on-Mouse IgG Blocking Solution). We then added primary antibody diluted in blocking solution for an overnight incubation at 4^{o}C. The following concentrations of antibodies were employed: CDH1 (1:100), LRP2 (1:100), VIM (1:200), XRCC5 (1:400), ACTA2 (1:100), PCNA (1:200). The next day, slides were washed 2 x 10 min. with PBS-T. Samples were incubated with 3% H_2O_2 diluted in PBS to quench any endogenous peroxidase activity. After another wash 2 x 10 min. in PBS-T, we incubated specimens with HRP-conjugated secondary antibodies diluted in blocking solution (1:1000) for 1 hr. at room temperature. Specimens were washed 3 x 15 min., then we proceeded with the chromogenic reaction by incubating slides in PBS with 0.1% H_2O_2 and 3,3′-Diaminobenzidine. Samples were incubated for ~ 1 – 10 min., depending on staining

intensity of signal relative to background. We counterstained samples with hematoxylin, dehydrated as described above, and mounted with Permount. Slides were digitized using an AxioScan Z1 (Zeiss) slide scanner.

Animal studies

Husbandry and ethics

All animal experiments were conducted with approval from the University of Ottawa Animal Care Committee (Protocol #OHRI1666), in accordance with the Canadian Council on Animal Care Standards and the Province of Ontario's Animals for Research Act. NSG mice were maintained in sterile housing conditions and fed autoclaved chow and water ad libitum.

Teratoma formation

hPSCs were dissociated into single cells by Accutase treatment for 15 min at 37ºC. Single cells were harvested, washed, and resuspended in 5 mg/mL Matrigel. NSG mice (8 week-old) were treated with buprenophrine 1 hour before injection, then anesthetized by isofluorane under a continuous stream of O_2. We bilaterally injected $1x10^6$ hPSC into the mouse tibialis anterior. We allowed teratomas to grow over a 12-week period, after which mice were sacrificed and teratomas extracted.

Renal subcapsular xenotransplants

At day 21 of differentiation, renal organoids were dissociated into single cells by Accutase treatment for 15 min at 37ºC followed by x3 trituration with a 25-guage needle. Single cells were harvested, washed, strained, and resuspended in PBS at $1x10^4$ cells/µL. NSG mice (8

497 week-old) were treated with buprenophrine 1 hour before injection, then anesthetized by
498 isofluorane under a continuous stream of O_2. Mouse kidneys were exposed through a flank
499 incision and partial exteriorization. We injected $0.5x10^6$ cells under the capsule of each kidney.
500 We returned kidneys to their anatomical location in the abdominal cavity and the incision site
501 closed with vicryl sutures (interior) and surgical clips (exterior). After 12 weeks, mice were
502 sacrificed and their kidneys were harvested. We fixed kidneys in 10% formalin overnight at 4ºC
503 and transferred to 70% EtOH until proceeding with pathological analysis.
504
505 **Single cell RNA sequencing**
506 *Sample preparation and RNA sequencing*
507 Renal organoids were dissociated into single cells by Accutase treatment for 15 min. at
508 37ºC followed by x3 trituration with a 25-guage needle. After dissociation, samples were
509 immediately transferred to cold PBS and labelled following the standard MULTI-seq protocol as
510 previously described,[39] albeit all on ice. Briefly, samples were incubated in an anchor:barcode
511 solution for 5 min., a co-anchor solution for another 5 min., then washed x3 in PBS with 1%
512 BSA. We strained cells and assessed viability via 1:1 dilution in 0.4% crystal violet, ensuring
513 >90% viable cells for every sample. Samples were pooled at equal cell numbers and
514 encapsulated using a Chromium Controller (10X Genomics) according to manufacturer
515 instructions. Finally, cells from all samples were pooled and sequenced using a NextSeq 500
516 (Illumina) at a depth of ~25,000 reads/cell.
517
518 *Data processing*

519 Raw sequencing data was processed using the *CellRanger* (10X Genomics) software.
520 First, FASTQ files were generated using the *mkfastq* function, then count matrices were
521 generated using the *count* function. Samples were demultipliex using the standard MUTLI-seq
522 workflow as described previously.[39] Data was imported into R, with most analyses performed
523 using the *Seurat* 4.0 package.[81] We first visually inspected quality control metrics and removed
524 samples with UMI counts < 500, number of uniquely detected genes < 250, and/or fraction of
525 mitochondrial reads > 15%. We also removed samples labelled as "doublets" or "negatives" by
526 the MULTI-seq analysis pipeline. A subset of cells that were later identified as dying, despite
527 passing QC metrics, were also removed. Finally, we removed the gene *SST*, as this gene was
528 aberrantly high in a limited number of cells and believed to be a technical artifact.
529 After removing low quality cells, we normalized expression data using the *SCTransform*
530 function in Seurat, including a regression variable for the difference in cell cycle score between
531 proliferating and non-proliferating cells. This cell cycle score, which predicts the cycle phase of
532 each cell (G1, G2/M, S), was determined using the *CellCycleScoring* function in Seurat. We then
533 performed Principal Components Analysis (PCA) and subsequently Uniform Manifold
534 Approximation and Projection (UMAP) on the 40 most variable PCA dimensions. This
535 processing produced the reduced dimensionality data which was employed for clustering and
536 annotation. For any subsetted data (e.g. nephron and glial-specific analysis), we recalculated the
537 PCA and UMAP for the selected cells.
538
539 *Cell clustering and annotation*
540 We clustered cells using standard functions available in the *Seurat* package. Briefly, data
541 is embedded in a K-nearest neighbour graph structure, and then this graph is partitioned into

highly interconnected "communities." Subsequently, cells are clustered by modularity optimization with the Louvain algorithm. We initially clustered cells at high resolution, and then merged clusters that were not distinguished by any biologically recognizable suite of unique markers genes.

We sought to annotate clusters based on uniquely and highly expressed genes that were identified using the *FindAllMarkers* function in Seurat, pre-selecting genes with an avg_log2FC > 0.25 and expressed in at least 10% of cells. We selected the top 20 marker genes (ranked by adjusted p-value) and looked for overlap in the top 20 marker genes from four mouse and human fetal kidney scRNA-seq datasets.[40–43] We elected to compare our data against multiple fetal kidney scRNA-seq datasets for two key reasons. One, cluster annotation is highly dependent on user determination of clustering granularity and taxonomy label choice, so using multiple datasets mitigates this bias. Two, the exact developmental timing of cells in our dataset is unknown (especially for the early timepoints), so comparing against datasets from multiple fetal timepoints increases the likelihood of annotating with appropriate markers.

After determining overlapping marker genes, we manually annotated each cluster using the most appropriate summarizing label. Often, inconsistent terminology in our resource datasets prevented designation of granular cell identities. For a subset of clusters (i.e. neural-glial populations), we did observe significant overlap of marker genes with our resource datasets, so we annotated clusters based on marker expression from the Mouse Organogenesis Cell Atlas, a comprehensive resource of mouse development scRNA-seq data.[82] Finally, a subset of clusters enriched in early timepoint samples did not consistently express unique markers genes, so we annotated these clusters as "Unspecified progenitors."

Trajectory analysis

We inferred a cell differentiation trajectory (i.e. the network of nodes and edges) using the *monocle3* algorithm.[82] Pseudotime values were determined by manually selected the root node based on proximity to the day 9 timepoint cells. We then analyzed differentially expressed genes across the inferred trajectory using *tradeSeq*.[83] Genes that varied significantly in the expression along the trajectory were determined using the *associationTest* function. We defined differentially expressed genes as those with an FDR < 0.01 and meanLogFC > 0.5. Genes that varied in expression between genotypes across the trajectory were determined using the *conditionTest* function, pre-selecting genes with a meanLogFC > 0.5. We defined differentially expressed genes are those with an FDR < 0.01.

Analysis with a public neural crest cell dataset

We downloaded a dataset on mouse NCC development.[47] This dataset includes 358 NCC marker genes and scores (i.e. relative expression) for each gene in several annotated stages of NCC development (i.e. distinct NCC identities). We aggregated specific annotations into more general categories by averaging expression values: early.migration, migration1, and migration2 were collapsed into "migratory," while sensory, autonomic, and mesenchymal were collapsed into "specifying."

To generate a continuous score of each neural crest identity along our glial differentiation trajectory, we applied Nadaraya–Watson kernel regression estimation to the maximal expression-ordered scores. More specifically, we first ordered NCC genes by the timing of their maximal expression during glial differentiation. Based on this ordering, we fit a kernel regression estimate

to the score for each of the NCC identity categories. This produced a continuous score for each NCC identity along the glial differentiation trajectory.

We performed a complementary analysis by visualizing expression of NCC marker genes, after attributing each marker gene to a single NCC identity, based on maximal score. Then, for each category of NCC genes, we extracted the top 10 maximally expressed throughout glial differentiation and plotted individual genes along pseudotime. We also visualized a single score across pseudotime for each NCC stage by aggregating with locally estimated scatterplot smoothing.

Additional scRNA-seq analyses

Differential gene expression analysis was performed using the *FindMarkers* function in Seurat, testing between WT vs *TSC1*$^{-/-}$ and WT vs *TSC2*$^{-/-}$ using the Wilcox statistic, pre-selecting genes with an avg_log2FC > 0.25 and expressed in at least 10% of cells. GO term enrichment was performed using *clusterProfiler* on significant DEGs (FDR < 0.05). Phylogenetic analysis was conducted with the *BuildClusterTree* function in Seurat. Compositional analysis was performed using the *imbalance_score* function from the *bioc2020trajectories* package.

Visualization of transcript expression

We visualized scRNA-seq transcript expression by several methods, including heatmaps, dotplots, violin plots, line graphs, and so forth. For simplicity, we plotted these values as "Expression" or "Average Expression." Here we define unambiguously the interpretation of these expression values. When a transcript was plotted in isolation and/or with its own Y-axis

(e.g. single gene dotplots, violin plots, or transcript expression on the UMAP points), we are plotting log transformed normalized expression. That is, the counts for each gene within a cell was divided by the total read counts for the cell, then multiplied by an arbitrary scaling factor (10,000), and then transformed by the natural log, i.e. log(exp + 1). When plotting multiple genes together (e.g. multiple gene dotplot, heatmap, multiple gene line graph), we used standardized expression values. That is, we took the log transformed normalized expression, centred expression values (i.e. subtract expression by the gene group mean), and then divided each value by the gene group standard deviation. Finally, plots of expression values against pseudotime (e.g. line plots, pseudotime heat maps) used predicted expression values extracted from the generalized additive model fit using *tradeSeq*.

621 **REFERENCES**

622 1. Salussolia, C. L., Klonowska, K., Kwiatkowski, D. J. & Sahin, M. Genetic Etiologies,
623 Diagnosis, and Treatment of Tuberous Sclerosis Complex. *Annu. Rev. Genomics Hum.*
624 *Genet.* (2019) doi:10.1146/annurev-genom-083118-015354.
625 2. Henske, E. P., Jóźwiak, S., Kingswood, J. C., Sampson, J. R. & Thiele, E. A. Tuberous
626 sclerosis complex. *Nat. Rev. Dis. Primer* **2**, 1–18 (2016).
627 3. Slegtenhorst, M. van *et al.* Identification of the Tuberous Sclerosis Gene TSC1 on
628 Chromosome 9q34. *Science* **277**, 805–808 (1997).
629 4. European Chromosome 16 Tuberous Sclerosis Consortium. Identification and
630 characterization of the tuberous sclerosis gene on chromosome 16. *Cell* **75**, 1305–1315
631 (1993).
632 5. Fryer, A. E. *et al.* Evidence that the gene for tuberous sclerosis is on chromosome 9. *Lancet*
633 *Lond. Engl.* **1**, 659–661 (1987).
634 6. Huang, J. & Manning, B. D. The TSC1–TSC2 complex: a molecular switchboard controlling
635 cell growth. *Biochem. J.* **412**, 179–190 (2008).
636 7. Cook, J. A., Oliver, K., Mueller, R. F. & Sampson, J. A cross sectional study of renal
637 involvement in tuberous sclerosis. *J. Med. Genet.* **33**, 480–484 (1996).
638 8. Rakowski, S. K. *et al.* Renal manifestations of tuberous sclerosis complex: Incidence,
639 prognosis, and predictive factors. *Kidney Int.* **70**, 1777–1782 (2006).
640 9. O'Callaghan, F. J., Noakes, M. J., Martyn, C. N. & Osborne, J. P. An epidemiological study
641 of renal pathology in tuberous sclerosis complex. *BJU Int.* **94**, 853–857 (2004).
642 10. Casper, K. A., Donnelly, L. F., Chen, B. & Bissler, J. J. Tuberous Sclerosis Complex: Renal
643 Imaging Findings. *Radiology* **225**, 451–456 (2002).

11. Shepherd, C. W., Gomez, M. R., Lie, J. T. & Crowson, C. S. Causes of Death in Patients With Tuberous Sclerosis. *Mayo Clin. Proc.* **66**, 792–796 (1991).
12. Amin, S. *et al.* Causes of mortality in individuals with tuberous sclerosis complex. *Dev. Med. Child Neurol.* **59**, 612–617 (2017).
13. Lam, H. C., Siroky, B. J. & Henske, E. P. Renal disease in tuberous sclerosis complex: pathogenesis and therapy. *Nat. Rev. Nephrol.* **14**, 704–716 (2018).
14. Siroky, B. J., Yin, H. & Bissler, J. J. Clinical and Molecular Insights into Tuberous Sclerosis Complex Renal Disease. *Pediatr. Nephrol.* **26**, 839–852 (2011).
15. LeRoy, M. A. & Rao, P. Angiomyolipoma With Epithelial Cysts. *Arch. Pathol. Lab. Med.* **140**, 594–597 (2016).
16. Green, A. J., Smith, M. & Yates, J. R. W. Loss of heterozygosity on chromosome 16p13.3 in hamartomas from tuberous sclerosis patients. *Nat. Genet.* **6**, 193–196 (1994).
17. Giannikou, K. *et al.* Low-level mosaicism in tuberous sclerosis complex: prevalence, clinical features, and risk of disease transmission. *Genet. Med.* 1 (2019) doi:10.1038/s41436-019-0562-6.
18. Tyburczy, M. E. *et al.* Mosaic and Intronic Mutations in TSC1/TSC2 Explain the Majority of TSC Patients with No Mutation Identified by Conventional Testing. *PLoS Genet.* **11**, e1005637 (2015).
19. Verhoef, S. *et al.* High rate of mosaicism in tuberous sclerosis complex. *Am. J. Hum. Genet.* **64**, 1632–1637 (1999).
20. Karbowniczek, M., Yu, J. & Henske, E. P. Renal Angiomyolipomas from Patients with Sporadic Lymphangiomyomatosis Contain Both Neoplastic and Non-Neoplastic Vascular Structures. *Am. J. Pathol.* **162**, 491–500 (2003).

667 21. Green, A. J., Sepp, T. & Yates, J. R. W. Clonality of tuberous sclerosis harmatomas shown
668 by non-random X-chromosome inactivation. *Hum. Genet.* **97**, 240–243 (1996).
669 22. Giannikou, K. *et al.* Whole Exome Sequencing Identifies TSC1/TSC2 Biallelic Loss as the
670 Primary and Sufficient Driver Event for Renal Angiomyolipoma Development. *PLOS Genet.*
671 **12**, e1006242 (2016).
672 23. Martin, K. R. *et al.* The genomic landscape of tuberous sclerosis complex. *Nat. Commun.* **8**,
673 15816 (2017).
674 24. Qin, W. *et al.* Angiomyolipoma Have Common Mutations in TSC2 but No Other Common
675 Genetic Events. *PLOS ONE* **6**, e24919 (2011).
676 25. Ashfaq, R., Weinberg, A. G. & Albores-Saavedra, J. Renal angiomyolipomas and HMB-45
677 reactivity. *Cancer* **71**, 3091–3097 (1993).
678 26. Chan, J. K. C. *et al.* Lymphangiomyomatosis and angiomyolipoma: closely related entities
679 characterized by hamartomatous proliferation of HMB-45-positive smooth muscle.
680 *Histopathology* **22**, 445–455 (1993).
681 27. Chilosi, M. *et al.* Cathepsin-k expression in pulmonary lymphangioleiomyomatosis. *Mod.*
682 *Pathol.* **22**, 161–166 (2009).
683 28. Jungbluth, A. A. *et al.* Expression of melanocyte-associated markers gp-100 and Melan-
684 A/MART-1 in angiomyolipomas. *Virchows Arch.* **434**, 429–435 (1999).
685 29. D'Armiento, J. *et al.* Mesenchymal Tumorigenesis Driven by TSC2 Haploinsufficiency
686 Requires HMGA2 and Is Independent of mTOR Pathway Activation. *Cancer Res.* (2016)
687 doi:10.1158/0008-5472.CAN-15-1287.
688 30. Nair, N. *et al.* Renal Manifestations of Tuberous Sclerosis Complex. *J. Kidney Cancer VHL*
689 **7**, 5–19 (2020).

690 31. Kwiatkowski, D. J. Animal Models of Lymphangioleiomyomatosis (LAM) and Tuberous
691 Sclerosis Complex (TSC). *Lymphat. Res. Biol.* **8**, 51–57 (2010).
692 32. Kobayashi, T. *et al.* A germ-line Tsc1 mutation causes tumor development and embryonic
693 lethality that are similar, but not identical to, those caused by Tsc2 mutation in mice. *Proc.*
694 *Natl. Acad. Sci.* **98**, 8762–8767 (2001).
695 33. Kwiatkowski, D. J. *et al.* A mouse model of TSC1 reveals sex-dependent lethality from liver
696 hemangiomas, and up-regulation of p70S6 kinase activity in Tsc1 null cells. *Hum. Mol.*
697 *Genet.* **11**, 525–534 (2002).
698 34. Kim, J., Koo, B.-K. & Knoblich, J. A. Human organoids: model systems for human biology
699 and medicine. *Nat. Rev. Mol. Cell Biol.* **21**, 571–584 (2020).
700 35. Garreta, E. *et al.* Fine tuning the extracellular environment accelerates the derivation of
701 kidney organoids from human pluripotent stem cells. *Nat. Mater.* **18**, 397–405 (2019).
702 36. Takasato, M. *et al.* Kidney organoids from human iPS cells contain multiple lineages and
703 model human nephrogenesis. *Nature* **526**, 564–568 (2015).
704 37. Delaney, S. P. *et al.* Human pluripotent stem cell modeling of tuberous sclerosis complex
705 reveals lineage-specific therapeutic vulnerabilities. *bioRxiv* 683359 (2020)
706 doi:10.1101/683359.
707 38. Freedman, B. S. *et al.* Modelling kidney disease with CRISPR-mutant kidney organoids
708 derived from human pluripotent epiblast spheroids. *Nat. Commun.* **6**, 8715 (2015).
709 39. McGinnis, C. S. *et al.* MULTI-seq: sample multiplexing for single-cell RNA sequencing
710 using lipid-tagged indices. *Nat. Methods* **16**, 619–626 (2019).

40. Lindström, N. O. *et al.* Conserved and Divergent Features of Mesenchymal Progenitor Cell Types within the Cortical Nephrogenic Niche of the Human and Mouse Kidney. *J. Am. Soc. Nephrol.* **29**, 806–824 (2018).
41. Magella, B. *et al.* Cross-platform single cell analysis of kidney development shows stromal cells express Gdnf. *Dev. Biol.* **434**, 36–47 (2018).
42. Adam, M., Potter, A. S. & Potter, S. S. Psychrophilic proteases dramatically reduce single-cell RNA-seq artifacts: a molecular atlas of kidney development. *Development* **144**, 3625–3632 (2017).
43. Combes, A. N. *et al.* Single cell analysis of the developing mouse kidney provides deeper insight into marker gene expression and ligand-receptor crosstalk. *Development* **146**, (2019).
44. van den Berg, C. W. *et al.* Renal Subcapsular Transplantation of PSC-Derived Kidney Organoids Induces Neo-vasculogenesis and Significant Glomerular and Tubular Maturation In Vivo. *Stem Cell Rep.* **10**, 751–765 (2018).
45. Cruz, N. M. *et al.* Organoid cystogenesis reveals a critical role of microenvironment in human polycystic kidney disease. *Nat. Mater.* **16**, 1112–1119 (2017).
46. Furlan, A. & Adameyko, I. Schwann cell precursor: a neural crest cell in disguise? *Dev. Biol.* **444**, S25–S35 (2018).
47. Soldatov, R. *et al.* Spatiotemporal structure of cell fate decisions in murine neural crest. *Science* **364**, eaas9536 (2019).
48. Zarei, M. *et al.* MITF is a driver oncogene and potential therapeutic target in kidney angiomyolipoma tumors through transcriptional regulation of CYR61. *Oncogene* 1–15 (2020) doi:10.1038/s41388-020-01504-8.

49. Hoek, K. S. *et al.* Novel MITF targets identified using a two-step DNA microarray strategy. *Pigment Cell Melanoma Res.* **21**, 665–676 (2008).
50. Siroky, B. J. *et al.* Evidence for pericyte origin of TSC-associated renal angiomyolipomas and implications for angiotensin receptor inhibition therapy. *Am. J. Physiol. - Ren. Physiol.* **307**, F560–F570 (2014).
51. Yue, M. *et al.* Evidence Supporting a Lymphatic Endothelium Origin for Angiomyolipoma, a TSC2− Tumor Related to Lymphangioleiomyomatosis. *Am. J. Pathol.* **186**, 1825–1836 (2016).
52. Gonçalves, A. F. *et al.* Evidence of renal angiomyolipoma neoplastic stem cells arising from renal epithelial cells. *Nat. Commun.* **8**, 1466 (2017).
53. Delaney, S. P., Julian, L. M. & Stanford, W. L. The neural crest lineage as a driver of disease heterogeneity in Tuberous Sclerosis Complex and Lymphangioleiomyomatosis. *Front. Cell Dev. Biol.* **2**, (2014).
54. Bissler, J. J. & Kingswood, J. C. Renal manifestation of tuberous sclerosis complex. *Am. J. Med. Genet. C Semin. Med. Genet.* **178**, 338–347 (2018).
55. Cho, J.-H. *et al.* Notch transactivates Rheb to maintain the multipotency of TSC-null cells. *Nat. Commun.* **8**, 1–16 (2017).
56. Nonomura, A. *et al.* Angiomyolipoma of the liver: a reappraisal of morphological features and delineation of new characteristic histological features from the clinicopathological findings of 55 tumours in 47 patients. *Histopathology* **61**, 863–880 (2012).
57. Thway, K. & Fisher, C. PEComa: morphology and genetics of a complex tumor family. *Ann. Diagn. Pathol.* **19**, 359–368 (2015).

58. Buechler, M. B. *et al.* Cross-tissue organization of the fibroblast lineage. *Nature* **593**, 575–579 (2021).
59. Little, M. H. & McMahon, A. P. Mammalian Kidney Development: Principles, Progress, and Projections. *Cold Spring Harb. Perspect. Biol.* **4**, a008300 (2012).
60. Takasato, M. & Little, M. H. The origin of the mammalian kidney: implications for recreating the kidney in vitro. *Development* **142**, 1937–1947 (2015).
61. Guillaume, R., Bressan, M. & Herzlinger, D. Paraxial mesoderm contributes stromal cells to the developing kidney. *Dev. Biol.* **329**, 169–175 (2009).
62. Engleka, K. A. *et al.* Insertion of Cre into the Pax3 locus creates a new allele of Splotch and identifies unexpected Pax3 derivatives. *Dev. Biol.* **280**, 396–406 (2005).
63. Wu, H. *et al.* Comparative Analysis and Refinement of Human PSC-Derived Kidney Organoid Differentiation with Single-Cell Transcriptomics. *Cell Stem Cell* **23**, 869-881.e8 (2018).
64. Phipson, B. *et al.* Evaluation of variability in human kidney organoids. *Nat. Methods* **16**, 79–87 (2019).
65. Czerniecki, S. M. *et al.* High-Throughput Screening Enhances Kidney Organoid Differentiation from Human Pluripotent Stem Cells and Enables Automated Multidimensional Phenotyping. *Cell Stem Cell* **22**, 929-940.e4 (2018).
66. Subramanian, A. *et al.* Single cell census of human kidney organoids shows reproducibility and diminished off-target cells after transplantation. *Nat. Commun.* **10**, 5462 (2019).
67. Unachukwu, U., Shiomi, T., Goldklang, M., Chada, K. & D'Armiento, J. Renal neoplasms in tuberous sclerosis mice are neurocristopathies. *iScience* **24**, 102684 (2021).

68. Adameyko, I. *et al.* Schwann Cell Precursors from Nerve Innervation Are a Cellular Origin of Melanocytes in Skin. *Cell* **139**, 366–379 (2009).
69. Cao, J. *et al.* Tuberous sclerosis complex inactivation disrupts melanogenesis via mTORC1 activation. *J. Clin. Invest.* **127**, 349–364 (2017).
70. Inoki, K. *et al.* mTORC1 activation in podocytes is a critical step in the development of diabetic nephropathy in mice. *J. Clin. Invest.* **121**, 2181–2196 (2011).
71. Iwata, W. *et al.* Podocyte-specific deletion of tubular sclerosis complex 2 promotes focal segmental glomerulosclerosis and progressive renal failure. *PLOS ONE* **15**, e0229397 (2020).
72. Ren, S. *et al.* Inactivation of Tsc2 in Mesoderm-Derived Cells Causes Polycystic Kidney Lesions and Impairs Lung Alveolarization. *Am. J. Pathol.* **186**, 3261–3272 (2016).
73. Volovelsky, O. *et al.* Hamartin regulates cessation of mouse nephrogenesis independently of Mtor. *Proc. Natl. Acad. Sci.* **115**, 5998–6003 (2018).
74. Onda, H., Lueck, A., Marks, P. W., Warren, H. B. & Kwiatkowski, D. J. *Tsc2*$^{+/-}$ mice develop tumors in multiple sites that express gelsolin and are influenced by genetic background. *J. Clin. Invest.* **104**, 687–695 (1999).
75. Wilson, C. *et al.* Tsc1 Haploinsufficiency without Mammalian Target of Rapamycin Activation Is Sufficient for Renal Cyst Formation in Tsc1+/− Mice. *Cancer Res.* **66**, 7934–7938 (2006).
76. Bissler, J. J. *et al.* Tuberous sclerosis complex exhibits a new renal cystogenic mechanism. *Physiol. Rep.* **7**, e13983 (2019).
77. Kumar, P. *et al.* Tsc2 mutation induces renal tubular cell nonautonomous disease. *Genes Dis.* (2021) doi:10.1016/j.gendis.2021.03.010.

78. Bissler, J. J. *et al.* Everolimus for angiomyolipoma associated with tuberous sclerosis complex or sporadic lymphangioleiomyomatosis (EXIST-2): a multicentre, randomised, double-blind, placebo-controlled trial. *The Lancet* **381**, 817–824 (2013).
79. Bissler, J. J. *et al.* Sirolimus for Angiomyolipoma in Tuberous Sclerosis Complex or Lymphangioleiomyomatosis. *N. Engl. J. Med.* **358**, 140–151 (2008).
80. Chen, Z. *et al.* Reprogramming progeria fibroblasts re-establishes a normal epigenetic landscape. *Aging Cell* **16**, 870–887 (2017).
81. Hao, Y. *et al.* Integrated analysis of multimodal single-cell data. *Cell* **184**, 3573-3587.e29 (2021).
82. Cao, J. *et al.* The single-cell transcriptional landscape of mammalian organogenesis. *Nature* **566**, 496–502 (2019).
83. Van den Berge, K. *et al.* Trajectory-based differential expression analysis for single-cell sequencing data. *Nat. Commun.* **11**, 1201 (2020).

SUPPLEMENTARY TABLES

Table S1. Genes upregulated in each cluster of the global UMAP. Genes reported for (A) general cluster groupings and (B) specific cluster groupings.

Table S2. Overlap of top 20 upregulated genes in each cluster of the global UMAP with marker genes from four public scRNA-seq datasets of the fetal mammalian kidney.

Table S3. Differential gene expression analysis comparing WT and *TSC1/2*$^{-/-}$ renal organoids. Comparisons made (A) globally, containing all cells, (B) within general cluster groupings, and (C) within specific cluster groupings.

Table S4. Genes upregulated in each cluster of the nephron epithelial UMAP.

Table S5. Overlap of top 20 upregulated genes in each cluster of the nephron epithelial UMAP with marker genes from four public scRNA-seq datasets of the fetal mammalian kidney.

Table S6. Genes upregulated in each cluster of the glial UMAP.

Table S7. Variation in gene expression along the glial differentiation trajectory.

Table S8. Differential gene expression between WT and *TSC1/2*$^{-/-}$ along the glial differentiation trajectory.

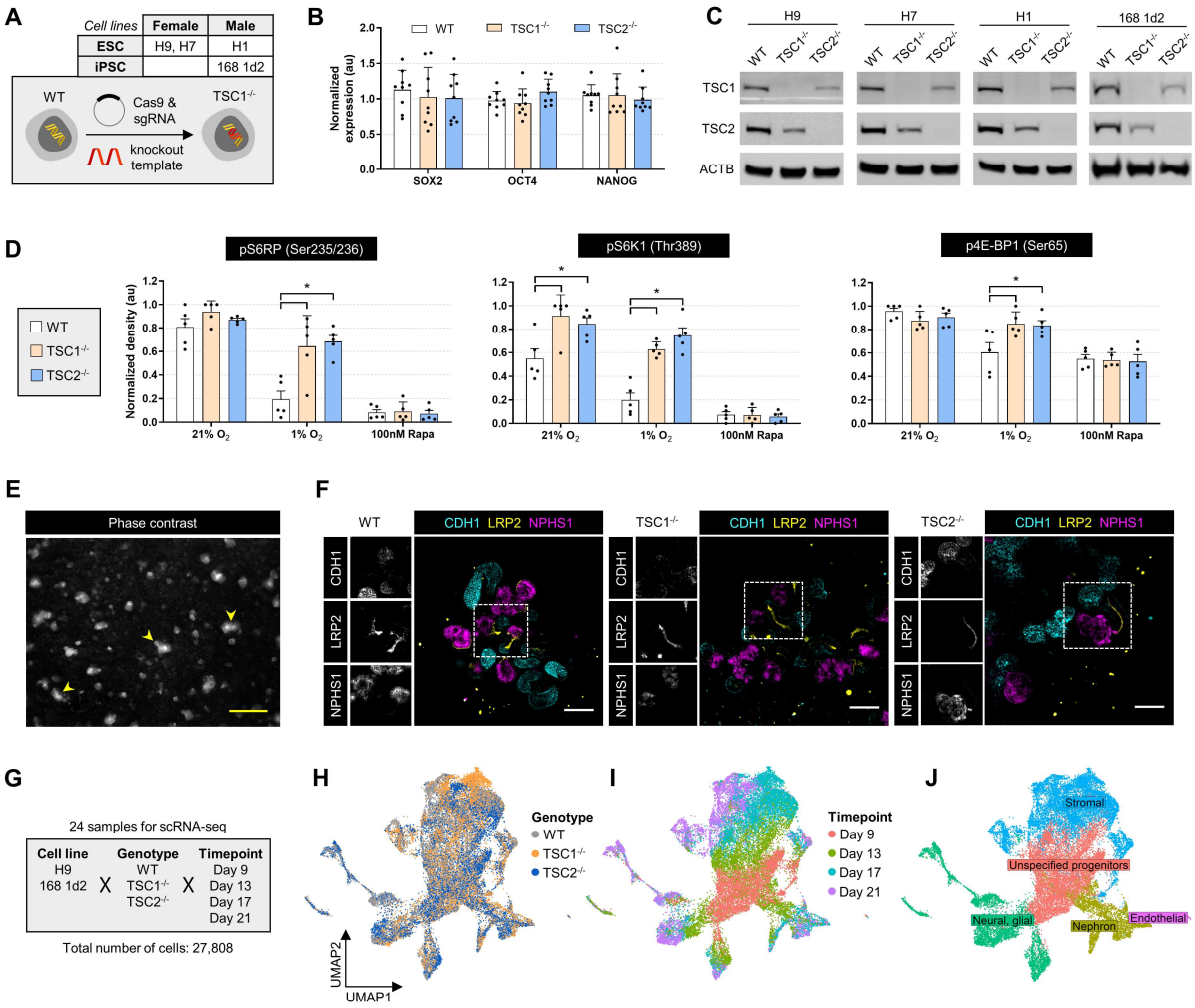

Fig 1

Figure 1: Development of a renal organoid model of TSC kidney disease. (A) Schematic of gene-editing strategy to knockout *TSC1* in four hPSC lineages. Acronyms are embryonic stem cells (ESC) and induced pluripotent stem cells (iPSC). (B) RT-qPCR gene expression in hPSC maintenance cultures (n = 9; ordinary ANOVA with Dunnett post-hoc comparison to WT). (C) Protein expression in hPSCs by western blot. (D) Quantification of western blot protein expression data in hPSCs. Treatment stimuli were for 6 hrs. (n = 5; two-way ANOVA with Dunnett post-hoc comparison to WT). (E) Phase contrast image of WT renal organoid differentiation at day 21. Yellow arrows indicate regions of epithelialization. Scale bar is 2 mm.

(F) Immunofluorescence images of renal organoid differentiations at day 17. Scale bars are 100 μm. (G) Overview of samples collected for scRNA-seq analysis. (H – J) UMAP two-dimensional plot of all 27,808 cells analyzed by scRNA-seq, coloured by (H) genotype, (I) timepoint, and (J) general cluster label.

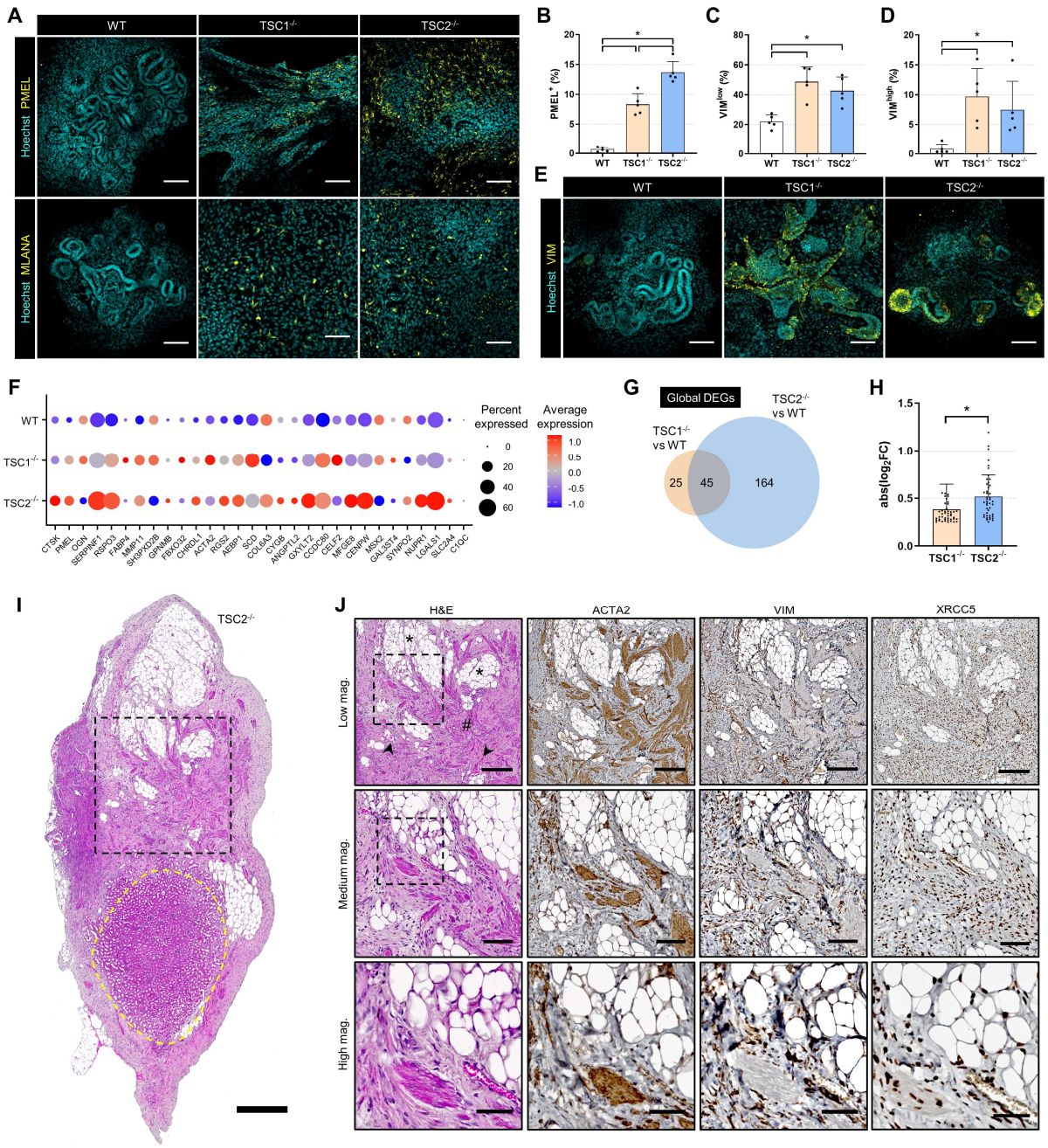

Fig 2

Figure 2: *TSC1/2*$^{-/-}$ renal organoids exhibit angiomyolipoma features. (A) Immunofluorescence images of renal organoid differentiations at day 21. Scale bars are 100 µm. (B – D) Quantification of flow cytometry data from bulk extraction of renal organoids (n = 5; two-way ANOVA with Tukey post-hoc comparison). (E) Immunofluorescence images of renal

855 organoid differentiations at day 21. Scale bars are 100 μm. (F) Expression of AML marker genes
856 in renal organoids at day 21. Marker genes are the top 30 upregulated genes in primary AMLs
857 compared to normal kidney.[23] (G) Overlap in globally differentially expressed genes (adjusted p-
858 val < 0.05, Wilcox signed-rank test) for WT vs. *TSC1*$^{-/-}$ and WT vs. *TSC2*$^{-/-}$ (H) Absolute $\log_2$FC
859 of *TSC1/2*$^{-/-}$ vs. WT of the 45 genes found to be commonly differentially expressed in G (n = 45;
860 Mann–Whitney U test). (I) Section from lesion formed following kidney subcapsular injection of
861 *TSC2*$^{-/-}$ renal organoids, stained with hematoxylin and eosin. Yellow dashed circle indicates
862 normal renal parenchymal. Black dashed square used as inset for low magnification image in
863 panel J. Scale bar is 500 μm. (J) Images at three magnifications from sections of lesion reported
864 in panel I. Samples were stained with hematoxylin and eosin or by immunohistochemistry with
865 3,3′-Diaminobenzidine. Symbols indicate fat (*), blood vessels (arrows), and smooth muscle-like
866 (#). Scale bars are 250 μm (low), 100 μm (med.), and 50 μm (high). (K) Section from human
867 AML stained with hematoxylin and eosin. Symbols indicate fat (*), blood vessel (arrow), and
868 smooth muscle-like (#). Scale bar is 250 μm.

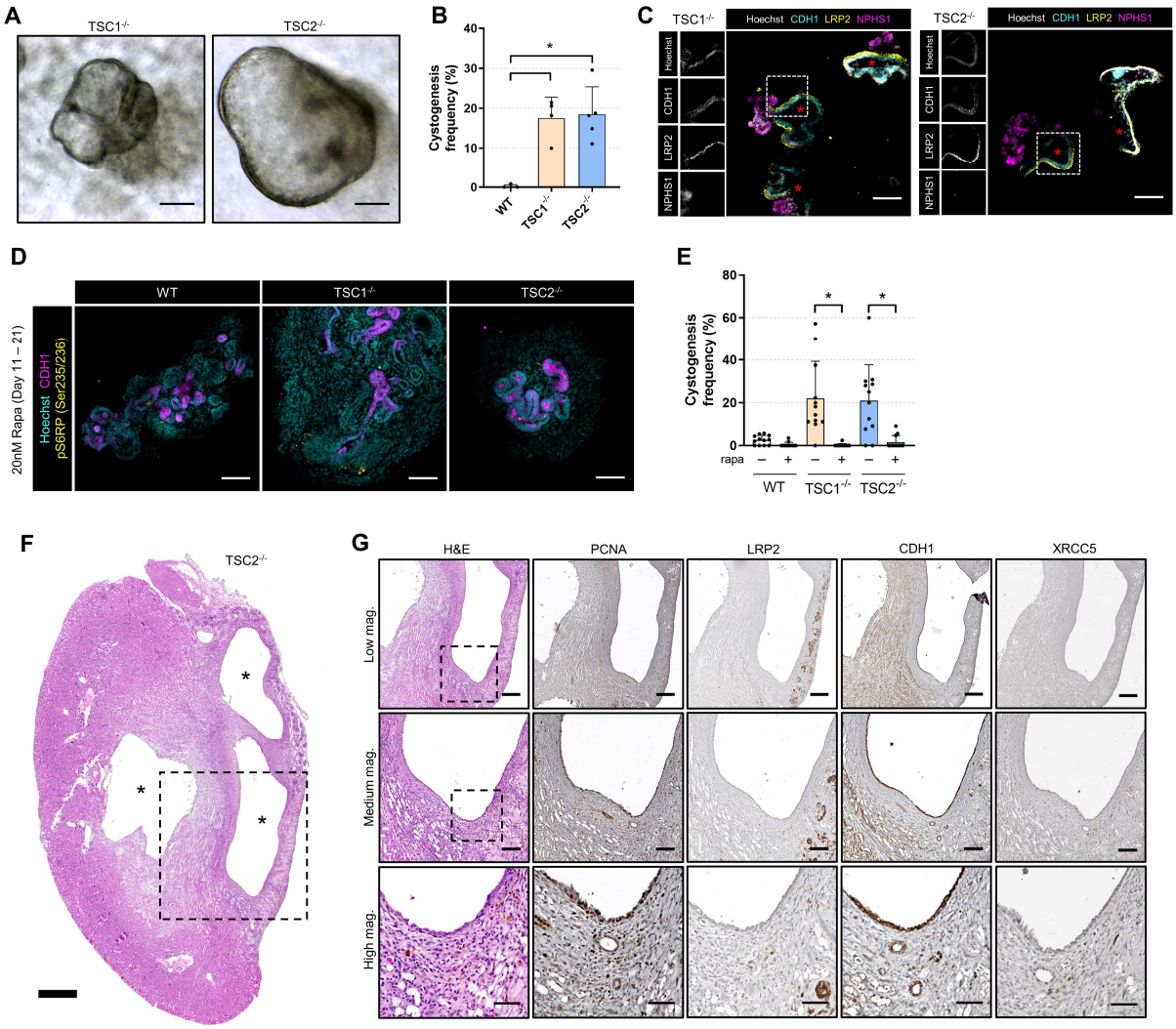

Fig 3

Figure 3: *TSC1/2*$^{-/-}$ renal organoids confer both cell autonomous and non-autonomous cystogenesis. (A) DIC images of cysts formed *in vitro* at day 19 of renal organoid differentiation. Scale bars are 200 µm. (B) Fraction of epithelialized regions that formed cysts by day 21 of renal organoid differentiation (n = 4 – 5; ordinary ANOVA with Dunnett post-hoc comparison to WT). (C) Immunofluorescence images of base of cysts from renal organoid differentiations at day 21. Scale bars are 100 µm. (D) Immunofluorescence images of renal organoid differentiations at day 21, with continuous 20 nM rapamycin treatment starting at day 11. Scale bars are 100 µm. (E) Fraction of epithelialized regions that formed cysts by day 21 of

renal organoid differentiation, without or with continuous 20 nM rapamycin treatment starting at day 11. (n = 5; two-way ANOVA with Šídák's post-hoc comparisons test). (F) Image of section from lesion formed following kidney subcapsular injection of *TSC2*$^{-/-}$ renal organoids, stained with hematoxylin and eosin. Black dashed square used as inset for low magnification images in panel G. Symbols indicate cysts (*). Scale bar is 500 µm. (G) Images at three magnifications from sections of lesion reported in panel F. Samples were stained with hematoxylin and eosin or by immunohistochemistry with DAB. Scale bars are 250 µm (low), 100 µm (med.), and 50 µm (high).

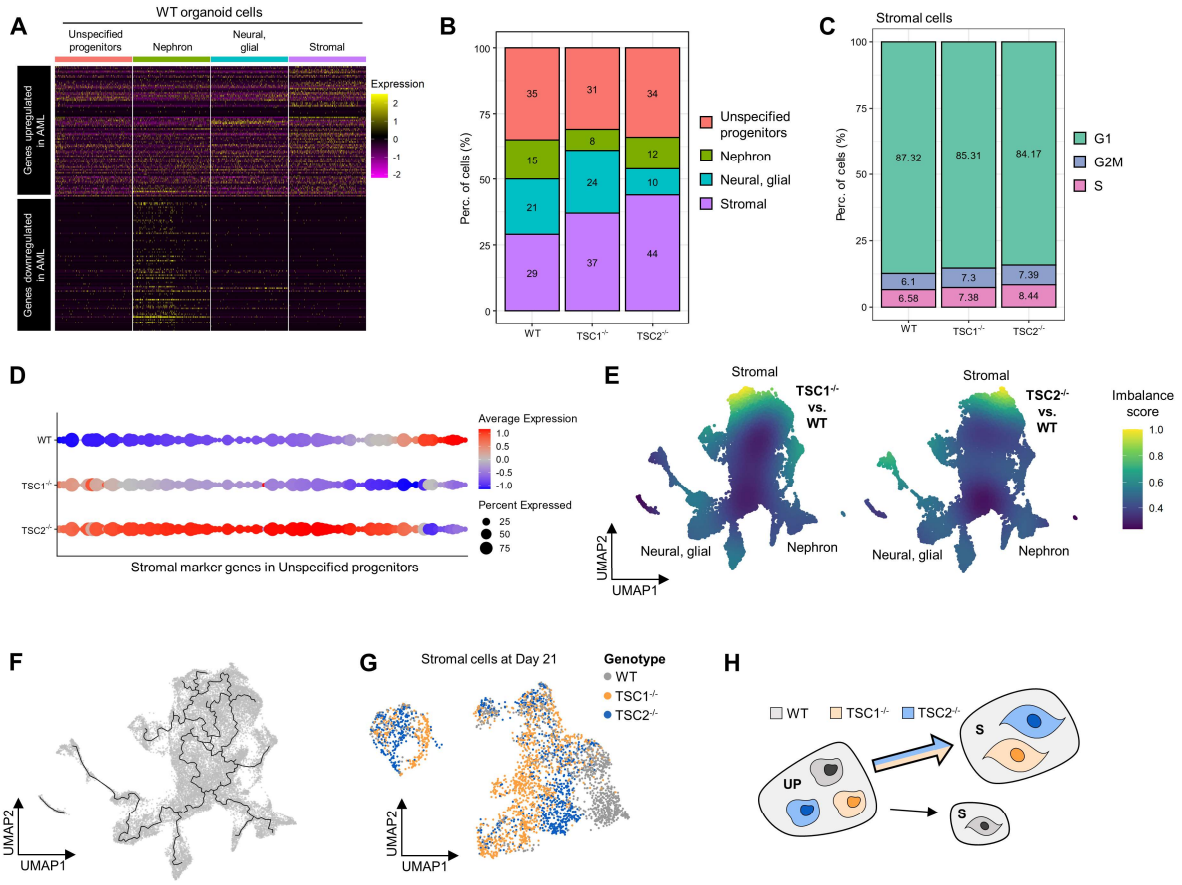

Fig 4

Figure 4: *TSC1/2* ablation favours stromal cell fate acquisition and alters terminal cell identity. (A) Heatmap of WT renal organoids sampling 1,000 cells from each organoid cluster. Marker genes plotted include the top 100 upregulated and downregulated genes in primary AML compared to normal kidney.[23] (B) Fraction of cells in renal organoid clusters. (C) Fraction of stromal cells in each phase of the cell cycle. (D) Expression of stromal marker genes in the renal organoid unspecified progenitor population. Marker genes were the top 100 upregulated genes of the stromal cluster. (E) Compositional analysis of *TSC1/2*$^{-/-}$ compared to WT. (F) Trajectory inference with *monocle3*[82]. (G) UMAP two-dimensional plot recalculated on subset of cells from stromal cluster, day 21 of differentiation. (H) Schematic of the effect of loss of *TSC1/2* on

898 stromal differentiation trajectory. Acronyms indicate unspecific progenitors (UP) and stromal

899 cells (S).

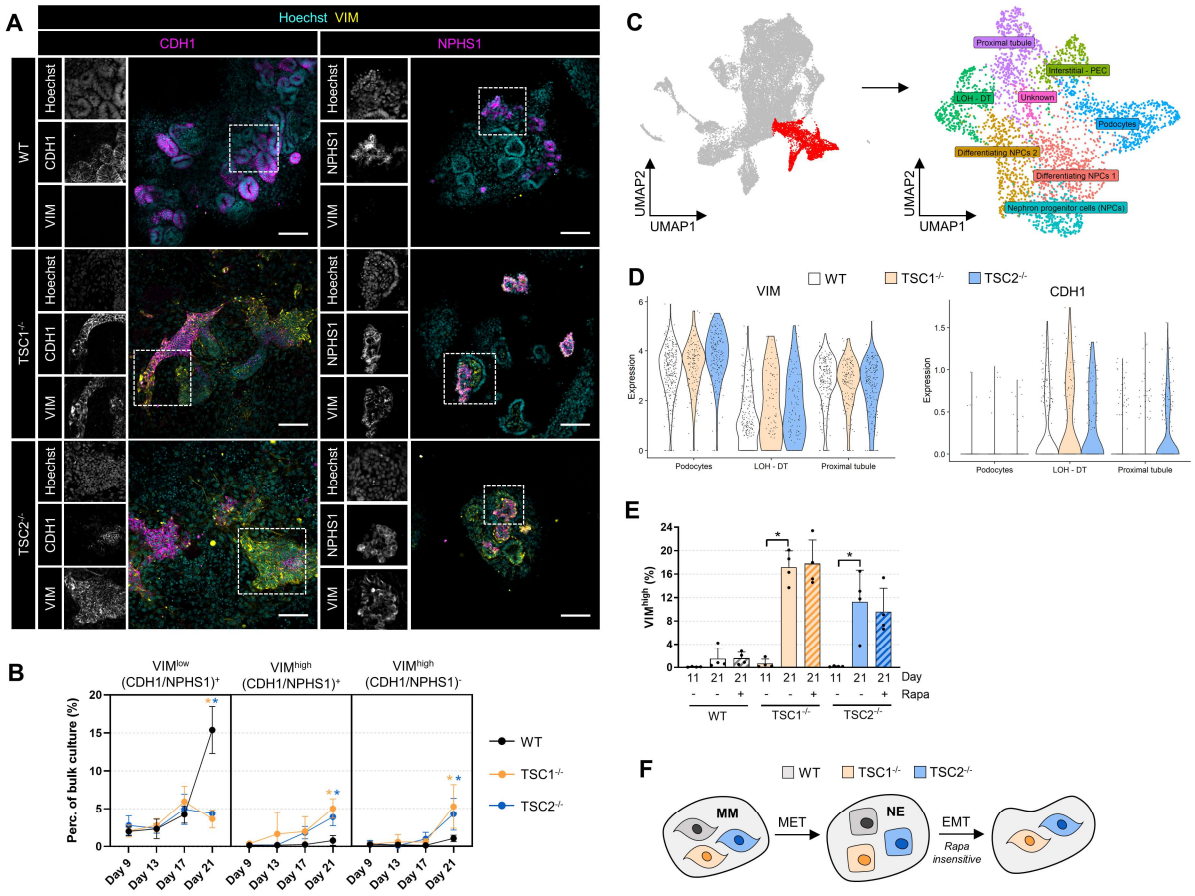

Fig 5

Figure 5: *TSC1/2* ablation causes a rapamycin insensitive epithelial-to-mesenchymal transition. (A) Immunofluorescence images of renal organoid differentiations at day 21. Scale bars are 100 µm. (B) Quantification of flow cytometry data from bulk extraction of renal organoids (n = 4; two-way ANOVA with Dunnett post-hoc comparison to WT). (C) Schematic of subsetting nephron epithelial differentiation branch and subsequent recalculation of PCA, UMAP, and cell clusters. Acronyms indicate loop of Henle (LOH), distal tubule (DT), and parietal epithelial cells (PEC). (D) Gene expression in renal organoids. (E) Quantification of flow cytometry data from bulk extraction of renal organoids at day 11 or 21, either without or with continuous 20 nM rapamycin treatment starting at day 11 (n = 4; two-way ANOVA with

911 Dunnett post-hoc comparison to day 21 untreated). (F) Schematic of effect of loss of *TSC1/2* on
912 nephron differentiation trajectory. Acronyms indicate metanephric mesenchyme (MM) and
913 nephron epithelial cells (NE).
914

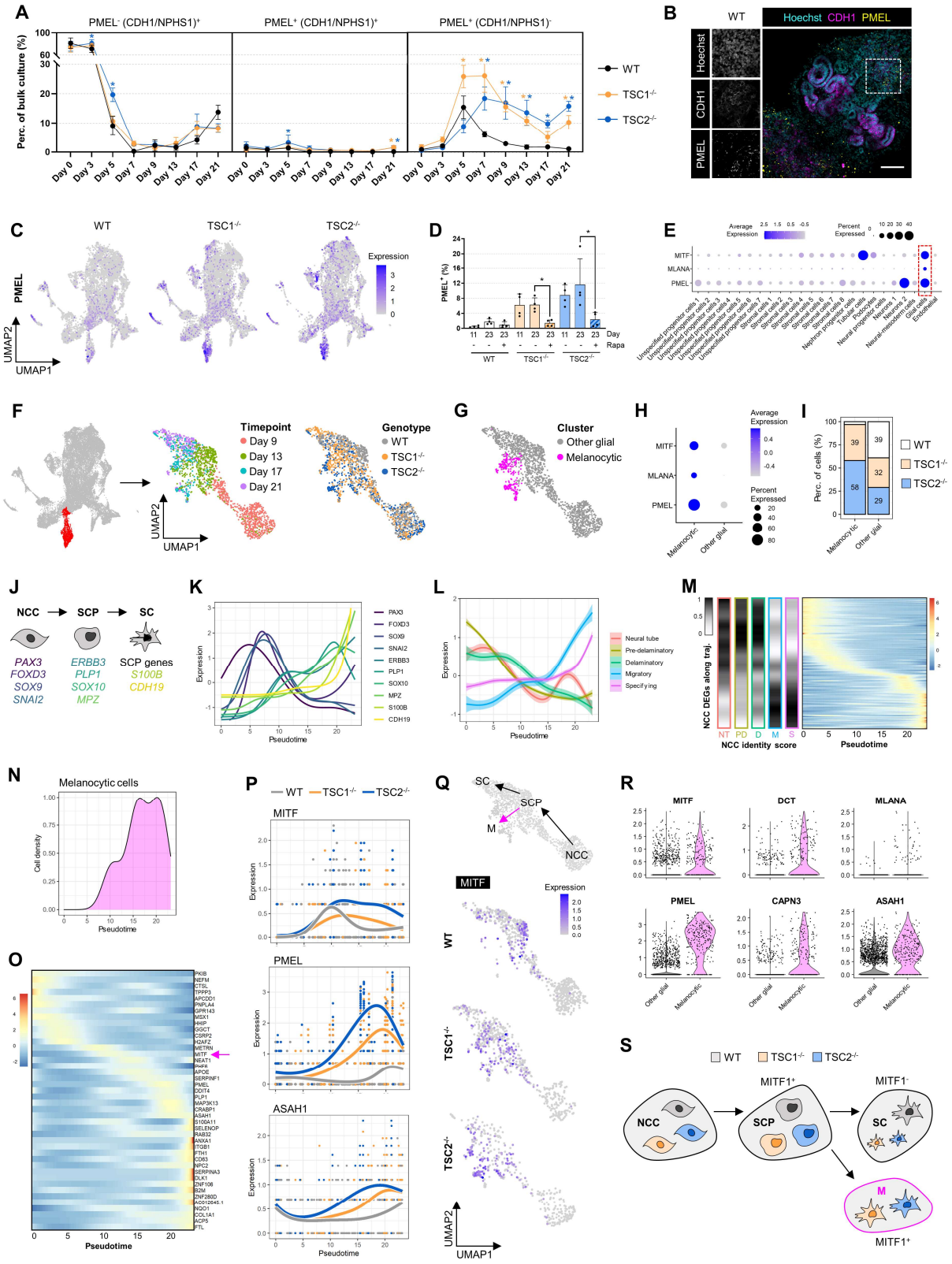
A
PMEL⁻ (CDH1/NPHS1)⁺
PMEL⁺ (CDH1/NPHS1)⁺
PMEL⁺ (CDH1/NPHS1)⁻
Perc. of bulk culture (%)
WT
TSC1-/-
TSC2-/-
B
WT
Hoechst CDH1 PMEL
Hoechst
CDH1
PMEL
C
WT
TSC1-/-
TSC2-/-
PMEL
Expression
UMAP2
UMAP1
D
PMEL+ (%)
Day
Rapa
E
Average Expression
Percent Expressed
MITF
MLANA
PMEL
F
Timepoint
Day 9
Day 13
Day 17
Day 21
Genotype
WT
TSC1-/-
TSC2-/-
UMAP2
UMAP1
G
Cluster
Other glial
Melanocytic
H
Average Expression
Percent Expressed
MITF
MLANA
PMEL
Melanocytic
Other glial
I
Perc. of cells (%)
WT
TSC1-/-
TSC2-/-
Melanocytic
Other glial
J
NCC
SCP
SC
PAX3
FOXD3
SOX9
SNAI2
ERBB3
PLP1
SOX10
MPZ
SCP genes
S100B
CDH19
K
Expression
Pseudotime
PAX3
FOXD3
SOX9
SNAI2
ERBB3
PLP1
SOX10
MPZ
S100B
CDH19
L
Expression
Pseudotime
Neural tube
Pre-delaminatory
Delaminatory
Migratory
Specifying
M
NCC DEGs along traj.
NCC identity score
Pseudotime
NT
PD
D
M
S
N
Melanocytic cells
Cell density
Pseudotime
O
Pseudotime
P
WT
TSC1-/-
TSC2-/-
MITF
PMEL
ASAH1
Expression
Pseudotime
Q
SC
SCP
M
NCC
MITF
Expression
WT
TSC1-/-
TSC2-/-
UMAP2
UMAP1
R
MITF
DCT
MLANA
PMEL
CAPN3
ASAH1
Other glial
Melanocytic
S
WT
TSC1-/-
TSC2-/-
MITF1+
MITF1-
NCC
SCP
SC
M
MITF1+

Fig 6

915

Figure 6: *TSC1/2* ablation induces MITF^{+} melanocytic cell fate acquisition. (A) Quantification of flow cytometry data from bulk extraction of renal organoids (n = 4; two-way ANOVA with Dunnett post-hoc comparison to WT). (B) Immunofluorescence image of WT renal organoid differentiation at day 14. Scale bar is 100 μm. (C) Expression of *PMEL* across all cells in the UMAP two-dimensional plot. (D) Quantification of flow cytometry data from bulk extraction of renal organoids at day 11 or 21, either without or with continuous 20 nM rapamycin treatment starting at day 11 (n = 4; two-way ANOVA with Dunnett post-hoc comparison to day 21 untreated). (E) Expression of key AML melanocytic marker genes. (F) Schematic of subsetting glial differentiation branch and subsequent recalculation of PCA and UMAP, colouring by genotype and day of differentiation. (G) UMAP two-dimensional plot highlighting melanocytic cells identified by unsupervised clustering. (H) Expression of key AML melanocytic marker genes. (I) Fraction of cells in glial clusters. (J) Schematic of neural crest cell (NCC) to Schwann cell precursor (SCP) to Schwann cell (SC) differentiation program, and associated marker genes. (K) Expression of NCC-SCP-SC marker genes along glial differentiation trajectory. (L) Aggregated expression of top 10 NCC identity marker genes along glial differentiation trajectory, determined from [47] as described in **Methods**. (M) Expression of NCC marker genes differentially expressed along glial differentiation trajectory. NCC identity score determined from [47] as described in **Methods**. (N) Density of melanocytic cells along glial differentiation trajectory. (O) Expression of genes that are differentially expressed between WT vs. *TSC1/2*$^{-/-}$ along glial differentiation trajectory. (P) Gene expression split by genotype along glial differentiation trajectory. (Q) Expression of *MITF* across cells in the glial UMAP two-dimensional plot. (R) Expression of *MITF* target genes. (S) Schematic of effect of loss of *TSC1/2*

938 on glial differentiation trajectory. Acronyms indicate neural crest cell (NCC), Schwann cell
939 precursor (SCP), Schwann cell (SC), and melanocytic cells (M).

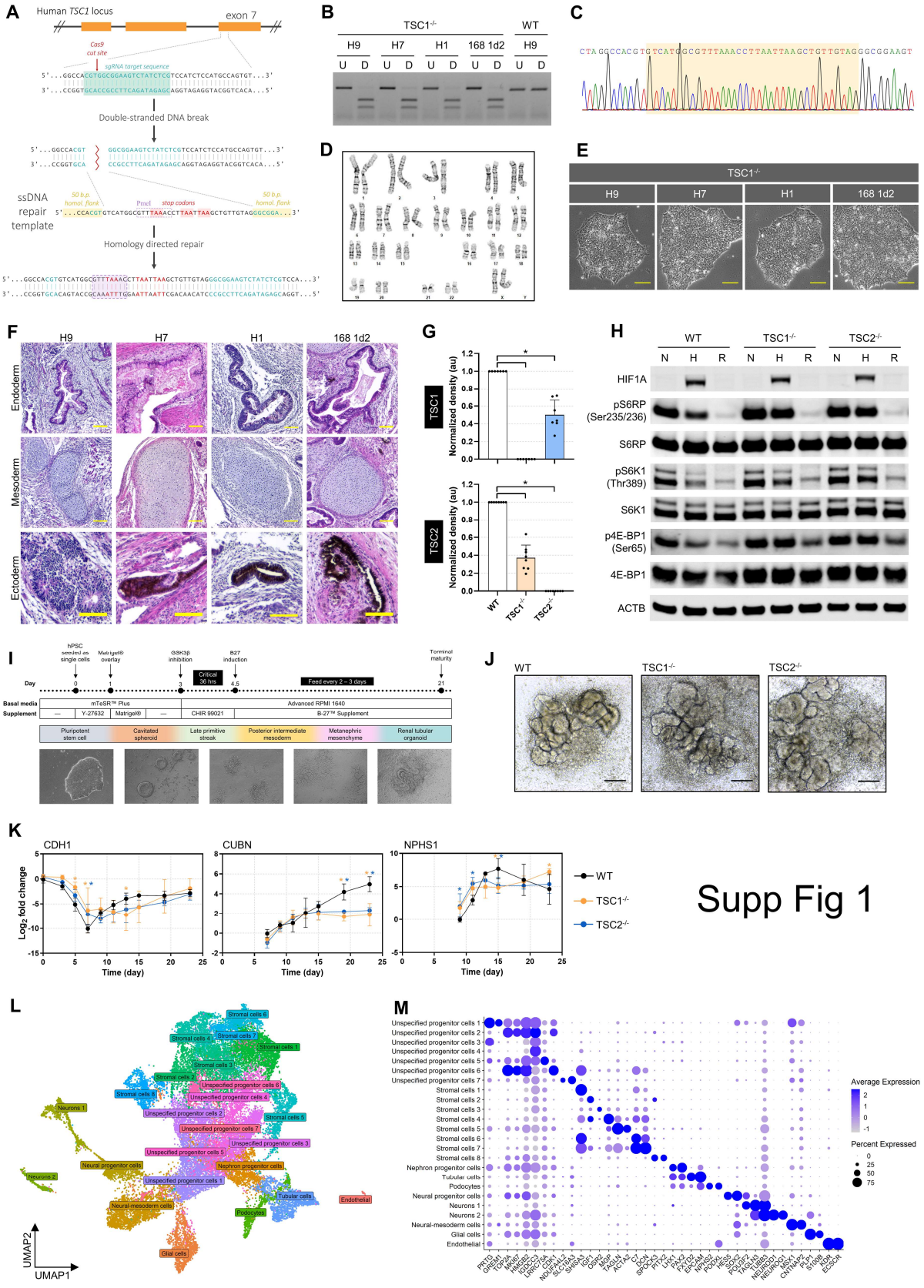

Supp Fig 1

940

Supplementary Figure 1: Development of a renal organoid model of TSC kidney disease. (A) Extended schematic of gene-editing strategy to knockout *TSC1* via homology-directed repair. (B) Restriction enzyme digestion with *PmeI* using PCR-amplified DNA from hPSCs, including undigested (U) and digested (D). (C) Sanger sequencing chromatogram of exon 7 of *TSC1* in hPSCs. Yellow region highlights knockout template. (D) Karyogram of chromosomes from *TSC1*$^{-/-}$ hPSCs. (E) Phase contrast images of hPSC colonies in maintenance culture. Scale bars are 200 μm. (F) Sections from hPSC-derived teratomas, stained with hematoxylin and eosin, showing gut epithelium (endoderm), cartilage (mesoderm), and neural rosettes and pigmented cells (ectoderm). Scale bars are 300 μm. (G) Quantification of western blot protein expression data from hPSCs. (n = 8; ordinary ANOVA with Dunnett post-hoc comparison to WT). (H) Protein expression by western blot. hPSCs were treated for 6 hrs. in either 21% O_2 (N), 1% O_2 (H), or 21% O_2 with 100 nM rapamycin (R). (I) Schematic of renal organoid differentiation protocol. (J) DIC images of epithelialized regions of renal organoid differentiation. Scale bars are 200 μm. (K) RT-qPCR bulk gene expression throughout renal organoid differentiation, with values relative to WT day 0 (n = 4; two-way ANOVA with Dunnett post-hoc comparison to WT). (L) UMAP two-dimensional plot of all 27,808 cells analyzed by scRNA-seq, coloured by specific cluster label. (M) Average expression of select marker genes used to distinguish each cell cluster.

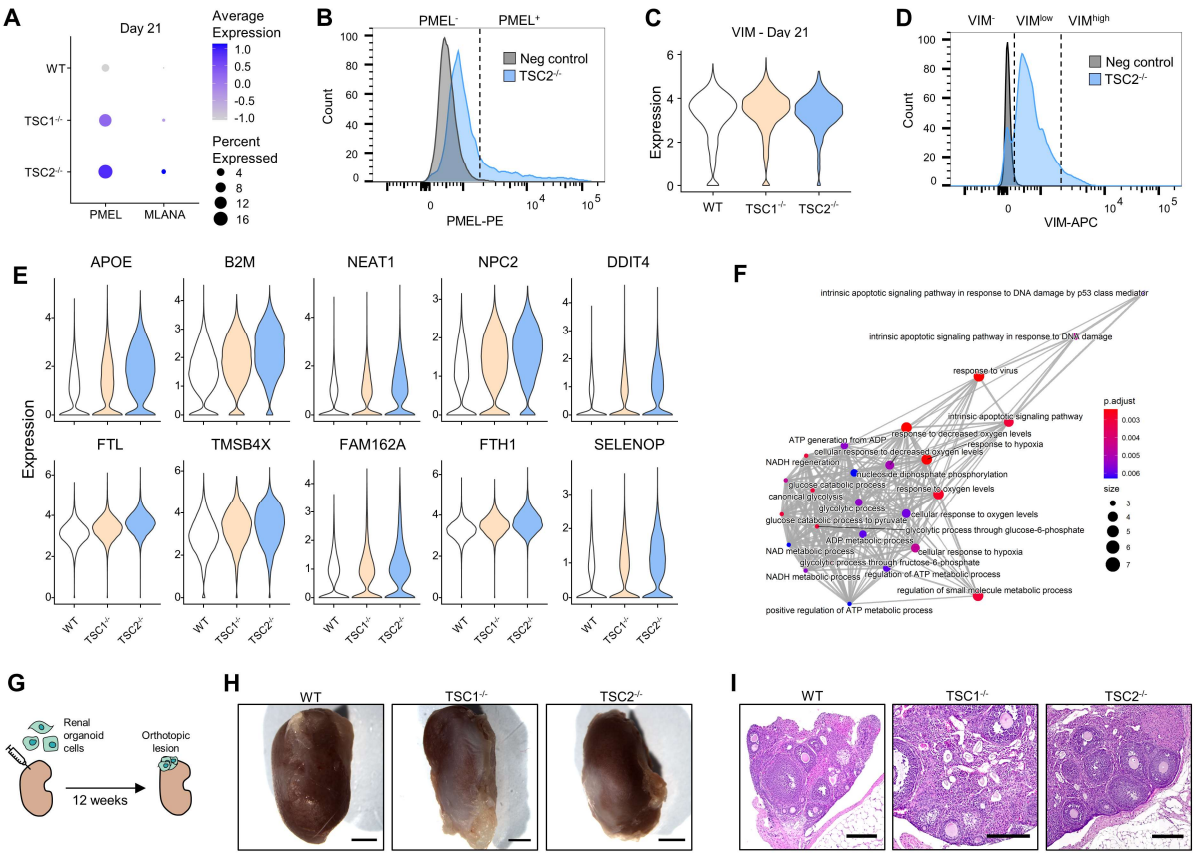

Supp Fig 2

Supplementary Figure 2: *TSC1/2*$^{-/-}$ renal organoids exhibit angiomyolipoma features. (A) Gene expression in all renal organoid cells at day 21. (B) Example of gating threshold used for distinguishing PMEL^{+} vs. PMEL^{-} cells from bulk culture extraction. Counts are normalized to sample mode. (C) Gene expression in all renal organoid cells at day 21. (D) Example of gating threshold used for distinguishing VIM^{high} vs. VIM^{low} vs. VIM^{-} cells from bulk culture extraction. Counts are normalized to sample mode (E) Network map of top 25 enriched GO terms, generated from the 45 genes found to be commonly differentially expressed in **Fig. 2G**. (F) Expression of select genes found to be globally upregulated in both *TSC1*$^{-/-}$ and *TSC2*$^{-/-}$ relative to WT. (G) Schematic of kidney subcapsular xenotransplantation of renal organoids. (H) Macroscopic lesions formed following kidney subcapsular injection with renal organoids. Scale bars are 25

970 mm. (I) Sections from kidney xenograft lesions, stained with hematoxylin and eosin. Scale bars
971 are 200 μm.
972

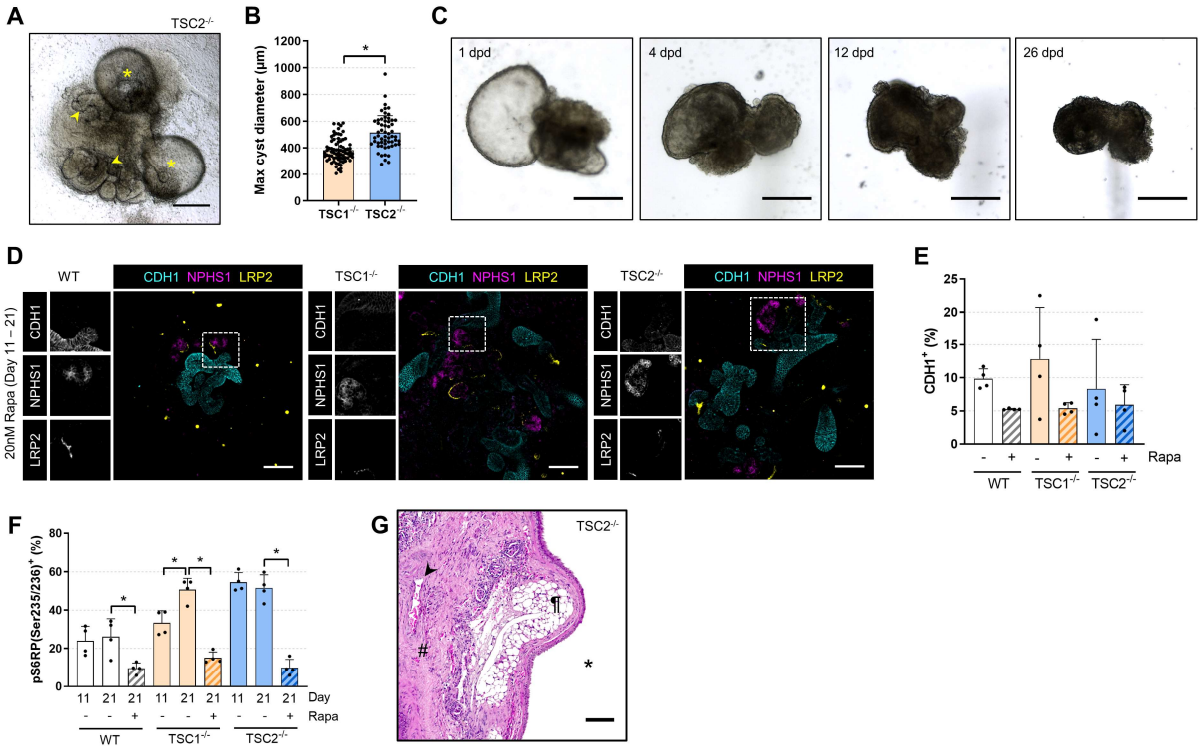

Supp Fig 3

Supplementary Figure 3: *TSC1/2*$^{-/-}$ renal organoids confer both cell autonomous and non-autonomous cystogenesis. (A) DIC color image of cysts arising from epithelialized regions, at day 21 of renal organoid differentiation. Symbols indicate cysts (*) and epithelialized structures (arrows). Scale bars are 400 µm. (B) Quantification of maximal cyst diameter at day 21 (n = 55 – 76; Student t-test). (C) DIC color images of cysts detached from culture stratum at day 21 of differentiation, tracked for up to 26 days post detachment (dpd). (D) Immunofluorescence images of renal organoid differentiations at day 21, with continuous 20 nM rapamycin treatment starting at day 11. Scale bars are 100 µm. (E) Quantification of flow cytometry data from bulk extraction of renal organoids at day 21, either without or with continuous 20 nM rapamycin treatment starting at day 11 (n = 4; two-way ANOVA with Šídák's post-hoc comparisons test). (F) Quantification of flow cytometry data from bulk extraction of renal organoids at day 11 or 21, either without or with continuous 20 nM rapamycin treatment starting at day 11 (n = 4; two-

986 way ANOVA with Dunnett post-hoc comparison to day 21 untreated). (G) Section from *TSC2*$^{-/-}$
987 kidney xenograft lesion, stained with hematoxylin and eosin. Symbols indicate cyst (*), blood
988 vessel (arrows), smooth muscle-like (#), fat (¶). Scale bar is 100 μm.
989

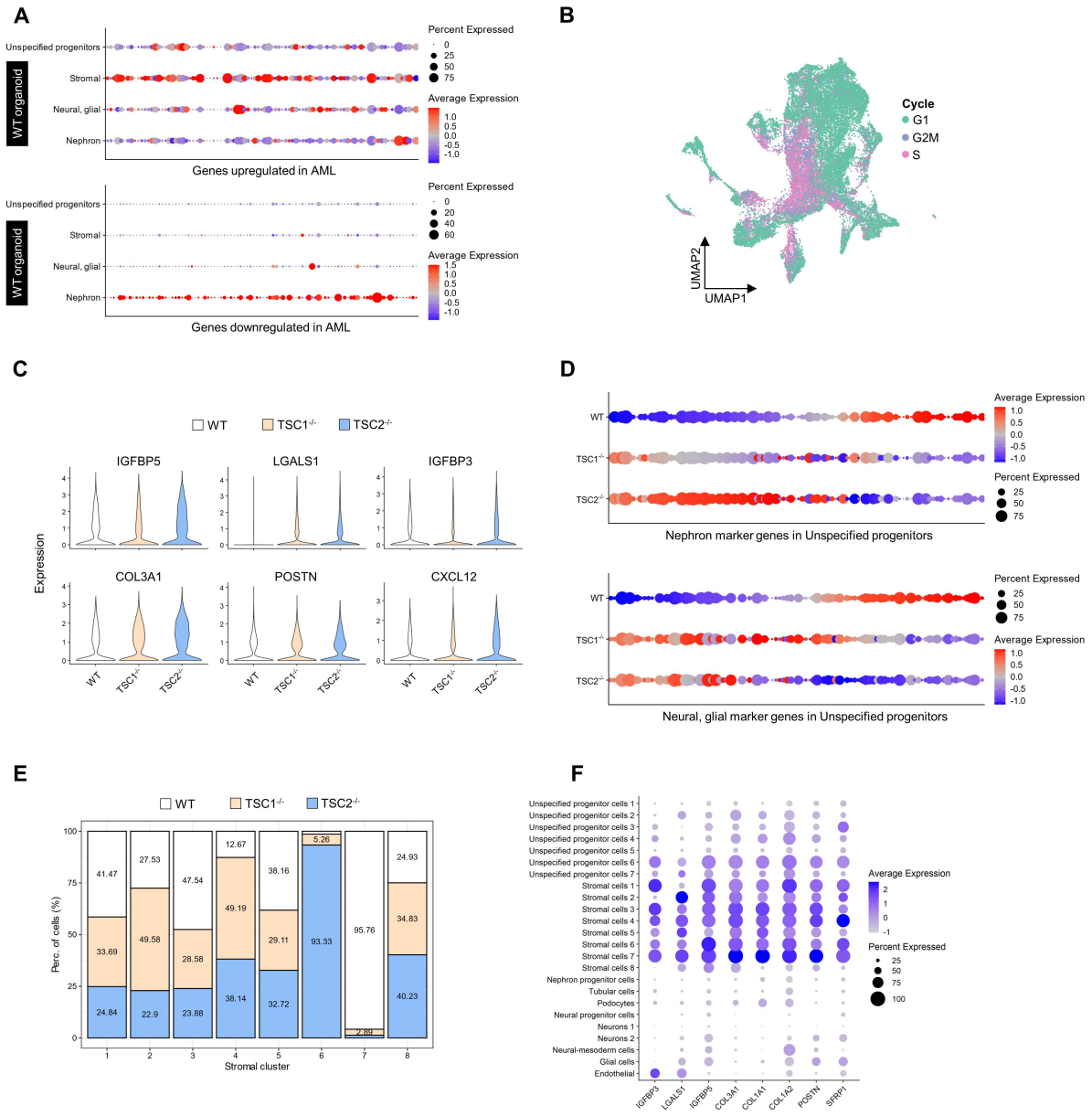

Supp Fig 4

Supplementary Figure 4: *TSC1/2* ablation favours stromal cell fate acquisition and alters terminal cell identity. (A) Expression in WT renal organoid clusters of top 100 upregulated and downregulated genes in primary AML compared to normal kidney.[23] (B) UMAP two-dimensional plot of all cells coloured by cell cycle phase. (C) Expression of select stromal marker genes in the unspecified progenitor population. (D) Expression of nephron or neural-glial

996 marker genes in the unspecified progenitors population. Marker genes were the top 100
997 significantly upregulated genes of the nephron or neural-glial clusters. (E) Fraction of cells in
998 renal organoid stromal clusters. (F) Expression of top upregulated stromal marker genes.
999

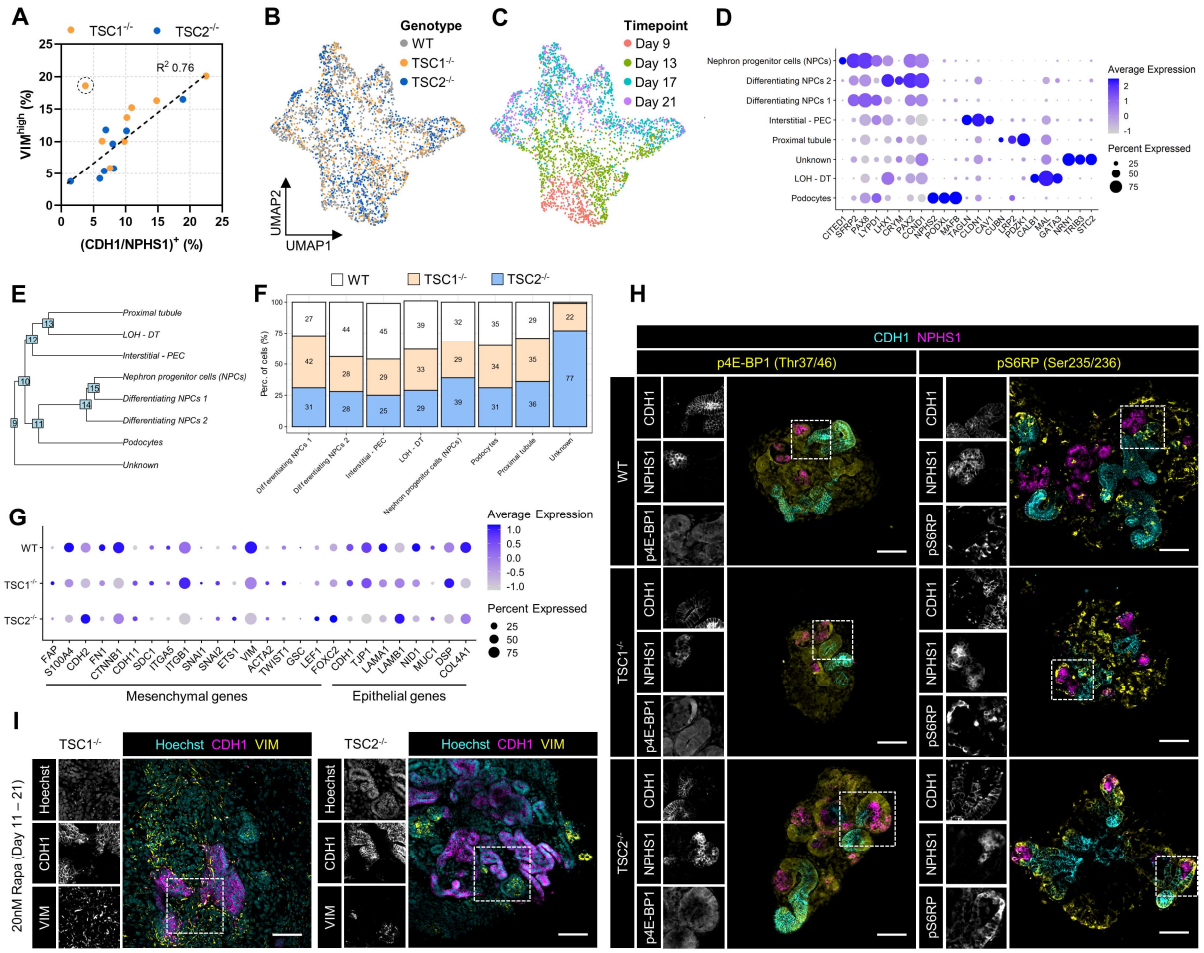

Supp Fig 5

Supplementary Figure 5: *TSC1/2* ablation causes a rapamycin insensitive epithelial-to-mesenchymal transition. (A) Correlation of flow cytometry data quantified from bulk extraction of renal organoids on day 21 (simple linear regression; data point circled with dashed line a statistical outlier not included in the calculation). (B – C) UMAP two-dimensional plot recalculated on subset of cells from nephron differentiation branch, colouored by (B) genotype or (C) day differentiation. (D) Average expression of select marker genes used to distinguish each nephron cell cluster. (E) Phylogenetic analysis of nephron cell clusters. (F) Fraction of cells in renal organoid nephron clusters. (G) Expression of select mesenchymal and epithelial markers in an aggregate of cells from the podocyte, loop of Henle/distal tubule, and proximal tubule

clusters. (H) Immunofluorescence images of renal organoid differentiations at day 17. Scale bars are 100 μm. (I) Immunofluorescence images of renal organoid differentiations at day 21, with continuous 20 nM rapamycin treatment starting at day 11. Scale bars are 100 μm.

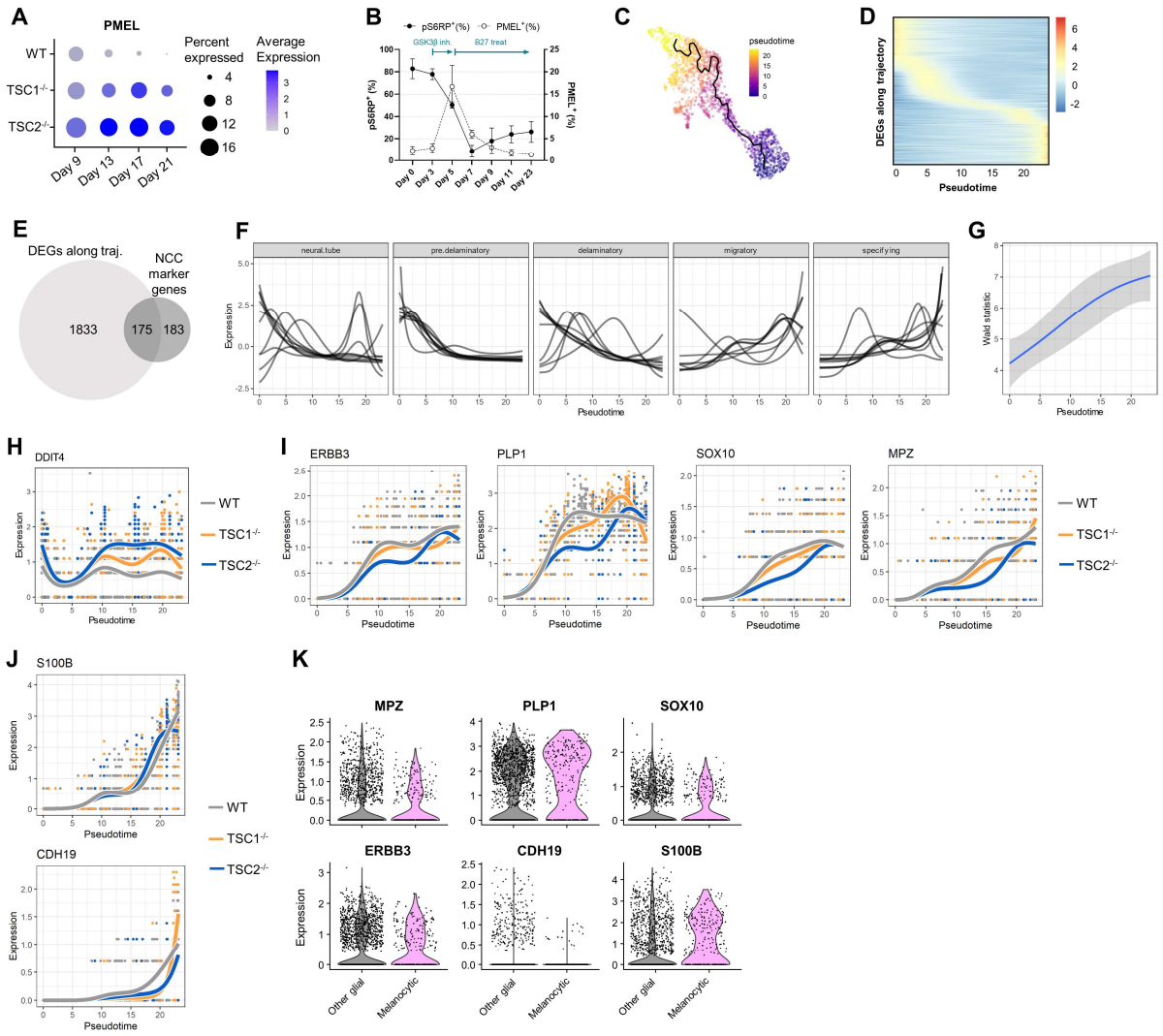

Supp Fig 6

Supplementary Figure 6: *TSC1/2* ablation induces MITF^{+} melanocytic cell fate acquisition.

(A) Expression of *PMEL* in renal organoids. (B) Quantification of flow cytometry data from bulk extraction of renal organoids. (C) Trajectory inference on UMAP two-dimensional plot of glial cluster, coloured by pseudotime. (D) Expression of genes found to be differentially expressed along glial differentiation trajectory, ordered by timing of maximal expression. (E) Overlap in differentially expressed genes along glial differentiation trajectory with NCC marker genes from [47]. (F) Expression of the top 10 NCC identity marker genes along glial differentiation trajectory,

determined from [47] as described in **Methods**. (G) Aggregated Wald statistic (measure of difference between WT and *TSC1/2*$^{-/-}$) by locally estimated scatterplot smoothing, using all genes differentially expressed along glial differentiation trajectory, ordered by timing of maximal expression. (H – J) Gene expression split by genotype along glial differentiation trajectory for marker genes of (H) mTORC1 regulation, (I) SCPs, and (J) SCs. (K) Expression of SCP and SC marker genes.